A MICROMACHINED ULTRASONIC DROPLET GENERATOR: DESIGN, FABRICATION, VISUALIZATION, AND MODELING

A Dissertation
Presented to
The Academic Faculty

By

John Marcus Meacham

In Partial Fulfillment
Of the Requirements for the Degree
Doctor of Philosophy in the
School of Mechanical Engineering

Georgia Institute of Technology

August 2006

A MICROMACHINED ULTRASONIC DROPLET GENERATOR: DESIGN, FABRICATION, VISUALIZATION, AND MODELING

Approved by:

Dr. Andrei G. Fedorov, Advisor
School of Mechanical Engineering
Georgia Institute of Technology

Dr. Ari Glezer
School of Mechanical Engineering
Georgia Institute of Technology

Dr. F. Levent Degertekin, Advisor
School of Mechanical Engineering
Georgia Institute of Technology

Dr. Mark Allen
School of Electrical and Computer Engineering
Georgia Institute of Technology

Dr. Yves Berthelot
School of Mechanical Engineering
Georgia Institute of Technology

Dr. Mark Papania, MD
Immunization Safety Office
Centers for Disease Control and Prevention

Date Approved: June 12, 2006

To my grandparents, William Marcus and Wanda Lee Meacham

ACKNOWLEDGEMENTS

I would like to thank my parents, John and Anita Meacham, without whose guidance I surely would not have achieved so much. I am also grateful to have met Kate Williams while working on the research presented here. History will likely prove her to be the most important discovery made during my time at Georgia Tech.

My advisors, Andrei G. Fedorov and F. Levent Degertekin, have been invaluable sources of both professional and personal support. Their generosity of time is only matched by their boundless enthusiasm for teaching, advising, encouraging, and inspiring their students.

Financial support through a National Aeronautics and Space Administration (NASA) grant (UG03-0050 NRA 02-OBPR-03, Project Monitor Dr. Karen Weiland) and the Centers for Disease Control and Prevention (CDC) is acknowledged and appreciated. In addition, I was also personally supported by a National Science Foundation (NSF) graduate research fellowship and a Graduate Assistance in Areas of National Need (GAANN) fellowship.

TABLE OF CONTENTS

LIST OF TABLES

LIST OF FIGURES

SUMMARY

The focus of this Ph.D. thesis research is a new piezoelectrically driven micromachined ultrasonic atomizer concept that utilizes fluid cavity resonances in the 1–5 MHz range along with acoustic wave focusing to generate the pressure gradient required for droplet or jet ejection. This ejection technique exhibits low-power operation while addressing the key challenges associated with other atomization technologies including production of sub-5 μm diameter droplets, low-temperature operation, the capacity to scale throughput up or down, and simple, low-cost fabrication. This thesis research includes device development and fabrication as well as experimental characterization and theoretical modeling of the acoustics and fluid mechanics underlying device operation. The main goal is to gain an understanding of the fundamental physics of these processes in order to achieve optimal design and controlled operation of the atomizer.

Simulations of the acoustic response of the system for various device geometries and different ejection fluid properties predict the resonant frequencies of the device and confirm that pressure field focusing occurs. High-spatial-resolution stroboscopic visualization of fluid ejection under various operating conditions is used to investigate whether the proposed atomizer is capable of operating in either the discrete-droplet or continuous-jet mode. The results of the visualization experiments combined with a scaling analysis provide a basic understanding of the physics governing the ejection process and allow for the establishment of simple scaling laws that prescribe the mode (e.g., discrete-droplet vs. continuous-jet) of ejection. In parallel, a detailed computational

fluid dynamics (CFD) analysis of the fluid interface evolution and droplet formation and transport during the ejection process provides in-depth insight into the physics of the ejection process and determines the limits of validity of the scaling laws.

These characterization efforts performed in concert with device development lead to the optimal device design. The unique advantages enabled by the developed micromachined ultrasonic atomizer are illustrated for challenging fluid atomization examples from a variety of applications ranging from fuel processing on small scales to ultra-soft electrospray ionization of biomolecules for bioanalytical mass spectrometry.

CHAPTER 1

INTRODUCTION

Since the 1950s, the evolution of inkjet printing techniques has led to improvements in direct drop-on-demand (DOD) droplet formation and indirect droplet formation from capillary stream breakup.[1] More recently, the utility of these technologies in a number of other applications has also been demonstrated. In addition to printing text and images onto porous surfaces, droplet production techniques are used in areas as diverse as biomedicine and biotechnology,[2-7] mass spectrometry,[8-14] fuel processing,[15-17] manufacture of multi-layer parts and circuits,[18-20] and deposition of doped organic polymers, low-*k* dielectrics, and photoresist without spinning.[21-25] In fact, these technologies can be utilized in any application requiring the production of monodisperse droplets using a repeatable and reliable process. Le[1] has provided a detailed review of current DOD and continuous inkjet technologies classifying them by droplet formation mechanism. Although the continuous inkjet (stream of droplets) is capable of placing a single droplet in a desired location provided a suitable droplet deflection (trapping) system is used, most research efforts are currently focused on less complex DOD methods that do not require unused ink to be recycled. DOD techniques typically utilize thermal, piezoelectric, electrostatic, or acoustic actuation to effect droplet formation and ejection.[1] Figure 1.1 illustrates the design and operation of common inkjet systems with those using piezoelectric actuation further classified based on the mode (e.g., bending, push, or squeeze) of operation of the piezoelectric element.

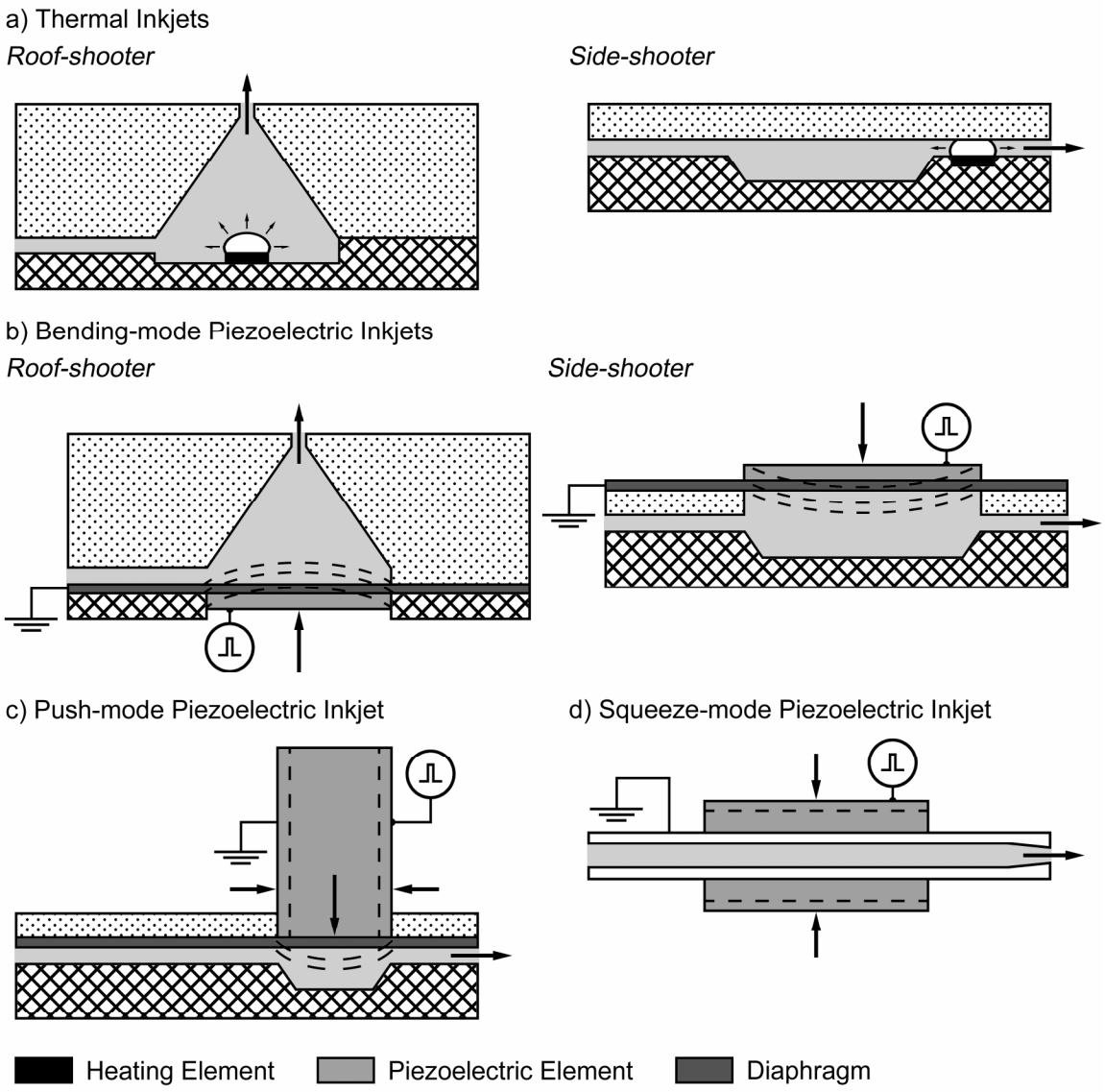

Figure 1.1. Common inkjet printing techniques: a) roof-shooter and side-shooter thermal inkjets, b) roof-shooter and side-shooter bending-mode piezoelectric inkjets, c) push-mode piezoelectric inkjet, and d) squeeze-mode piezoelectric inkjet.

Several existing inkjet techniques are successful in specific applications, but there are challenges associated with extending each to more general use. For example, the thermal inkjet method cannot be used with most biological samples due to thermal degradation[2] and the possibility of a limited lifetime associated with burnout of the heater resistor. Implementation of piezoelectric inkjets in applications requiring a large array of nozzles is difficult due to increased power consumption,[4] and displacement of a large ink volume is required to eject a droplet from a single orifice limiting the spatial density of the array elements.[1] In addition to addressing the inherent challenges of each droplet generation method, the continued need for reliable production of ever decreasing droplet volumes calls for further development of inkjet technologies. Typical droplet and nozzle diameters range from 30 μm (113 pL) down to 10 μm (9 pL);[26] however, certain applications, e.g., aerosol production for medical inhalation purposes, require that the droplet diameter is below 5 μm (65 fL).[2] Further, in some cases droplet production at low temperature (e.g., biological applications) and with low power consumption (e.g., portable fuel processing) is important. Scalability of throughput, simplicity and robustness of operation, and low cost of fabrication are also desirable.

The current research is focused on a new piezoelectrically driven, micromachined atomizer concept that utilizes fluid cavity resonances in the 0.5–5 MHz range combined with acoustic wave focusing for droplet generation or jet ejection. This technique is capable of addressing the key challenges associated with existing inkjet methods including the ability to produce droplets with sub-5 μm diameters, low-temperature and low-power operation, the capacity to scale throughput up or down by using an array, and simple, low-cost fabrication. This thesis research includes device development and

fabrication as well as experimental characterization and theoretical modeling of the acoustics and fluid mechanics underlying device operation. The main goal is to gain an understanding of the fundamental physics of these processes in order to achieve optimal design and controlled operation of the atomizer.

Chapter 2 provides a detailed discussion of the atomizer concept, the device design, and the fabrication process. A comparison of the proposed droplet generation method with conventional techniques is provided to illustrate how this atomizer concept is capable of addressing the challenges associated with other atomization techniques. Fabrication issues that arose during the micromachining of the atomizer, including creation of the pyramidal nozzles that focus the acoustic waves and the nozzle orifices used for droplet/jet ejection, are presented along with solutions developed to resolve each of these problems. Two different designs of realized devices are described and evaluated based on ease of fabrication, robustness, and performance.

Simulations of the acoustic response of the system for various device geometries and different working fluid properties are described in Chapter 3. Not only do these simulations confirm that pressure field focusing occurs, but they are also able to predict the resonant frequencies of the device as well as which of these frequencies result in the most efficient transfer of power from the piezoelectric transducer to the ejected droplets.

High-spatial-resolution stroboscopic visualization of the ejection of different fluids under various operating conditions is presented in Chapter 4. The results of the visualization experiments combined with a scaling analysis of the fluid mechanics provide a basic understanding of the physics governing the ejection process and allow for the establishment of simple scaling laws that prescribe the mode (e.g., discrete-droplet vs.

continuous-jet) of ejection. In addition to predicting which ejection mode is expected at different operating frequencies, the visualization experiments elucidate other salient features of the ejection process. The variation in droplet diameter as a function of frequency of operation and the velocity of the ejected droplets as a function of the amplitude of the voltage signal driving the piezoelectric transducer are investigated. The mechanisms by which jet disintegration into droplets occurs are also discussed.

In Chapter 5, a detailed computational fluid dynamics (CFD) analysis of the fluid interface evolution and droplet formation and transport during the ejection process is described to provide in-depth insight into the physics of the ejection process and to test the validity of the scaling laws. The volume of fluid (VOF) technique is used to track the free surface separating the fluid being ejected and the surrounding air during the creation of a stream of droplets or a single jet. The orifice size and frequency of operation are varied under controlled conditions resulting in a regime map which defines regions of discrete-droplet and continuous-jet mode of ejection, as well as the transition between these two distinct operation modes. The simulation results are compared with experimental data. Additional phenomena including the frequency dependence of the droplet diameter and the relationship between droplet velocity and the pressure wave amplitude are also studied using the CFD analysis.

As was alluded to previously, a number of difficulties are associated with extending any droplet generation technique to more general use. To illustrate the breadth of application of this device, the ultrasonic atomizer investigated in this thesis has been employed in three different fields of application. Chapter 6 provides the details of this work. The device is shown to address the challenges associated with atomization of liquid

fuels for microscale fuel processing applications, generation of an aerosol for oral delivery of the measles vaccine, and electrospray production for the ion source of a mass spectrometer. In each case, results of proof-of-concept experiments are provided to confirm that the device is able to successfully perform these tasks.

CHAPTER 2

DEVICE CONCEPT, DESIGN, AND FABRICATION

The demand for a universal technology enabling reliable generation of droplets with diameters ranging from sub-5 μm to tens of microns necessitates further development of conventional inkjet devices as well as research into conceptually new atomization methods. Desired attributes of an atomization technique include:

- **High degree of control of the atomization process.** The atomization technique needs to be able to generate monodisperse droplets with a high degree of control of droplet velocity and diameter down to sub-5 μm.
- **Low-temperature and low-power operation.** Power transfer from the actuation mechanism to the ejected droplets must be efficient to reduce the required power input as well as minimize losses that can lead to device heating.
- **High dynamic range.** The atomization technique must be capable of operation at low flow rates; however, individual droplet generation elements can be arrayed to meet high flow rate requirements.
- **Low cost.** Device fabrication and assembly must be simple, and devices need to be robust.

Several existing droplet generation methods perform well in specific applications, but none can achieve all of the desirables listed above. Squeeze-mode piezoelectric droplet generators are characterized by a high degree of control of the atomization process at low flow rates but are difficult to array.[13,26-29] Air-assisted atomizers are unable to operate at low flow rates. Recently developed devices utilizing microfabrication

techniques promise the ability to achieve monodisperse droplet generation from flexible arrays that operate at low temperature and with low power consumption;[2,4-6,21,22,24,25,30] however, implementation of these techniques often requires complex fabrication methods leading to expensive and low-yield processes. The piezoelectrically driven, micromachined atomizer concept investigated in this thesis research addresses many of the challenging issues associated with existing devices.

2.1 Review of Piezoelectric and Acoustic Droplet Generation Devices

A number of piezoelectric and acoustic droplet generators are discussed in the literature. Zoltan[29] was first to describe a squeeze-mode piezoelectric droplet generator. A concentric piezoelectric transducer or sleeve fitted to the outside of a glass capillary was used to generate an oscillating pressure gradient in a cylindrical cavity and eject the working fluid. Berggren *et al*.,[13] Chen and Basaran,[26] Switzer,[28] and Kung *et al*.[27] have used similar techniques to produce micron-sized droplets. Berggren *et al*.[13] were able to produce individual 27 μm droplets or continuous streams of smaller droplets from a 20 μm diameter capillary by increasing the amplitude of the pulse sent to the piezoelectric sleeve. Chen and Basaran[26] used a glass capillary with a larger orifice diameter of 70 μm to produce droplets as small as 32 μm by manipulating the signal waveform driving the piezoelectric transducer. By varying the nozzle aperture size, the driving voltage of the piezoelectric, and the liquid pressure within the chamber, Switzer[28] was able to produce droplets with diameters between 5 and 500 μm. Between 250 and 300 V were required to initiate droplet ejection, but this was reduced to 20 to 30 V for continuous operation. Kung *et al*.[27] successfully generated droplets as small as 3–4 μm in diameter from a 1 μm orifice. Although squeeze-mode piezoelectric devices provide repeatable ejection of

small quantities of liquid without requiring a pressurized fluid supply, they are difficult to array and are limited to low throughput (kHz frequency range) operation.

Elrod *et al.*[31] have proposed an interesting method of nozzleless droplet generation from the free surface of a liquid pool by applying the acoustic radiation pressure generated by highly localized tone bursts of energy that were focused using an acoustic lens. An experimental and theoretical analysis that shows the droplet size to be proportional to the wavelength of the incident acoustic waves was presented; thus, transducers operating at very high frequencies of up to 300 MHz were needed to eject 5 μm diameter droplets. By patterning the electrode on the piezoelectric film driving a similar device, Kwon *et al.*[32] were able not only to produce but also to control the trajectory of streams of 10 μm droplets ejected from the surface of a liquid pool. Fabrication of thin film piezoelectrics and development of driver electronics as well as requirements on orientation and precise fluid level control during operation, make this approach very complex, expensive, and rather impractical.

The use of micromachining techniques enables micron-sized orifices to be made with a high degree of control while providing the flexibility to produce large arrays of uniform nozzles. Femtoliter-sized (~5 μm diameter) droplets were produced by de Heij *et al.*[2] and Yuan *et al.*[5,6] using bending mode piezoelectric transducers operating at up to 200 kHz to actuate arrays of 5 μm diameter micromachined nozzles. Multiple trapezoidal cavities were created in silicon using an anisotropic wet etch in a potassium hydroxide (KOH) solution leaving 10–20 μm thick membranes. An array of nozzles was then etched through each of the membranes using deep reactive ion etching (DRIE).[2]

By replacing the ink with fuel and adjusting some parameters of operation, Ederer *et al*.[15,16] were first to use a piezoelectric DOD inkjet printhead to produce a combustible fuel-air mixture. Subsequent development of this concept yielded a fuel injector consisting of 38 nozzles with 50 μm diameter orifices that were arranged in concentric circles. 40–60 μm diameter droplets were generated at frequencies ranging from 500 to 2800 Hz.

Perçin *et al*.[4,21,22,24,25,30] have presented a technique for ejecting liquids using a micromachined flextensional ultrasound transducer to excite the axisymmetric resonant modes in a clamped circular plate. The plate was made of silicon nitride that was deposited over an oxide layer on a silicon wafer using low pressure chemical vapor deposition (LPCVD). DRIE was used to etch large (100 μm diameter) reservoirs through the back of the wafer up to the oxide layer. An isotropic etch was then used to open up the oxide behind the circular plates. Finally, dry plasma etching was used to create small orifices in the middle of the circular plates.[30] As the plate vibrated, the pressure within a fluid reservoir was increased above atmospheric during part of the cycle. If this pressure was high enough to overcome fluid inertia and surface tension, a droplet was ejected.[30] Droplet ejection was demonstrated for a number of orifices including some as small as 4 μm in a 100 μm diameter membrane driven at 3.45 MHz.

Perçin and coworkers [4,21,22,24,25] have also developed a device where each ejection chamber was individually excited using annular piezoelectric elements deposited around the orifices on the surfaces of the vibrating circular plates. They suggested that the excitation achievable in this configuration was too small to eject some fluids, but proposed that a combination of the bulk and local piezoelectric pumping could be used to

individually actuate droplet ejectors. Although readily scaled by arraying individual ejectors, the complexity of the fabrication processes required to create large-extent, thin membrane structures and multilayer films including thin film piezoelectrics limits practical application of this device.

2.2 Proposed Atomizer Concept

The proposed atomizer concept aims to satisfy each of the desirable attributes of an atomization technique by addressing the issues associated with existing droplet generation methods. Specific features with some that are unique to this concept include:

- **Ultrasonic actuation.** Atomization at low flow rates is achieved through piezoelectrically driven ultrasonic actuation.
- **Resonant operation.** Power consumption is reduced via operation at fluid cavity resonances which also leads to low-temperature operation.
- **Acoustic wave focusing.** The liquid horn structure of the ejector element is exploited to achieve focusing of the acoustic waves. This produces a highly localized pressure gradient at the nozzle orifice, leading to a further reduction in power consumption and frictional heating.
- **Frequency matching.** Efficient power transfer from the piezoelectric transducer to the acoustic waves in the ejection cavity is accomplished by matching the resonant frequency of the driving piezoelectric to the envelope of cavity resonances.
- **Scalability of throughput.** A high dynamic range of operation is achieved through arraying of droplet generation elements.

- **Low-cost, high-yield microfabrication.** Machining costs are reduced by using a batch microfabrication process with only a few, simple steps.

2.3 Device Design and Preliminary Modeling

The proposed atomizer concept is realized in a device by 1) creating an array of resonant fluid cavities, 2) making each cavity focus acoustic waves when driven at appropriate resonant frequencies, and 3) selecting a piezoelectric transducer material and geometry for the most efficient operation in the desired (resonant) frequency range. This conceptual framework is used to design the droplet generator depicted in Figure 2.1. The device comprises a fluid reservoir that is formed between a bulk ceramic piezoelectric transducer and an array of liquid horn structures wet etched into single crystal silicon oriented with the (100) plane. The fluid chamber height and ejector plate thickness are dictated by a nominal 500 μm thickness standard silicon wafer. A number of horn shapes are capable of focusing acoustic waves; however, the pyramidal shape was chosen as it can be conveniently produced via anisotropic wet etching of single crystal (100) oriented silicon.[33] The focusing horn is designed to terminate near the opposite side of the ejector plate. Depending on the fabrication process, the orifice is either created in bulk silicon or in a thin membrane as shown in Figure 2.1. This simple device design and the fabrication procedure described in Section 2.4 represent a significant improvement over the complexity inherent in other ultrasonic ejector designs.[4,7,21,22,24,25,30,31]

The liquid horn structure, cavity size, and the speed of sound within the ejection fluid dictate the resonant frequencies and thus the operating frequencies of the device.[34] Inexpensive and commonly available lead zirconate titanate (PZT-8) ceramic is used for

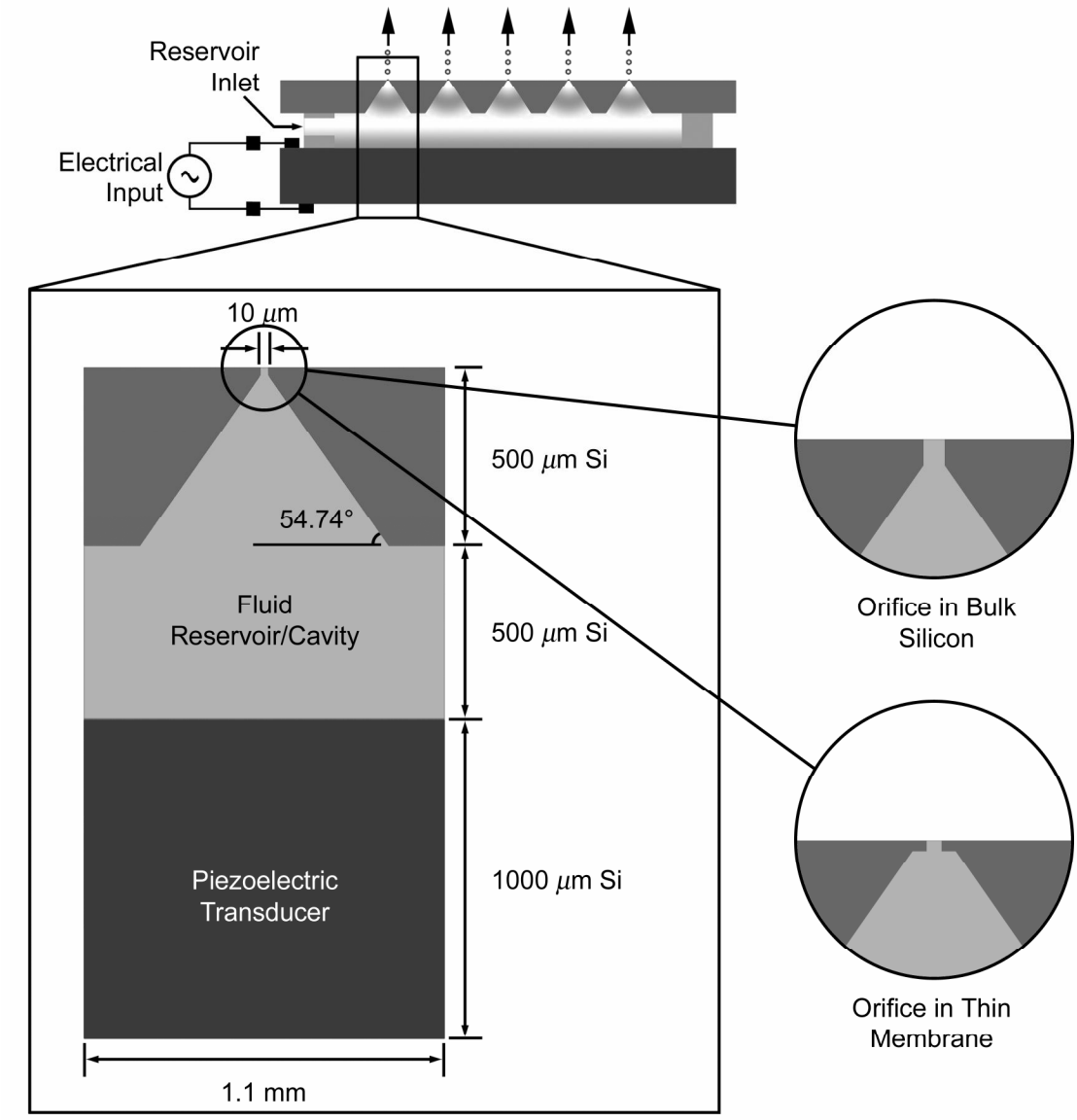

Figure 2.1. Schematic of the ultrasonic atomizer along with representative dimensions. The dimensions of the ejector are defined by the anisotropic character of the silicon. Depending on the fabrication process, the orifice is either created in bulk silicon or a thin membrane.

the piezoelectric transducer. The reported[35] longitudinal acoustic wave velocity characteristic of this piezoelectric material allows for an estimation of the transducer thickness that is required to place the transducer resonance within the envelope of fluid cavity resonances. When the piezoelectric transducer is driven at the fundamental cavity resonant frequency or any of the higher cavity modes, a standing acoustic wave develops, and constructive interference in the pyramidal nozzle focuses the wave so that the peak pressure gradient occurs near the tip of the nozzle. Although the frequency at which this device operates most efficiently must match and is therefore dictated by the fluid chamber resonances for power-efficient operation, the geometry of the chamber can be readily modified to increase or decrease the driving frequency of operation (for example by increasing or decreasing the height of the cavity) according to desired specifications.

The acoustic simulation package of the commercial finite element analysis code ANSYS[36] is used to confirm the acoustic wave focusing by the horn-shaped nozzles at the selected fluid cavity resonances. Figure 2.2 is a plot of the electrical input impedance of the piezoelectric transducer as a function of frequency for a water-loaded device with the geometry shown in Figure 2.1. The peaks in the real component of the complex impedance indicate the resonant frequencies of the device, and among those, the frequencies that correspond to acoustic wave focusing are circled. The pressure fields within the fluid chamber at the first three cavity resonances are provided in Figure 2.3. In each case, the pyramidal nozzles focus the acoustic wave generating a highly localized pressure gradient near the nozzle tips. This is further illustrated in the inset of Figure 2.3 which shows the pressure field in the center nozzle at a frequency of 1.62 MHz. The details of the ANSYS simulations are found in Chapter 3.

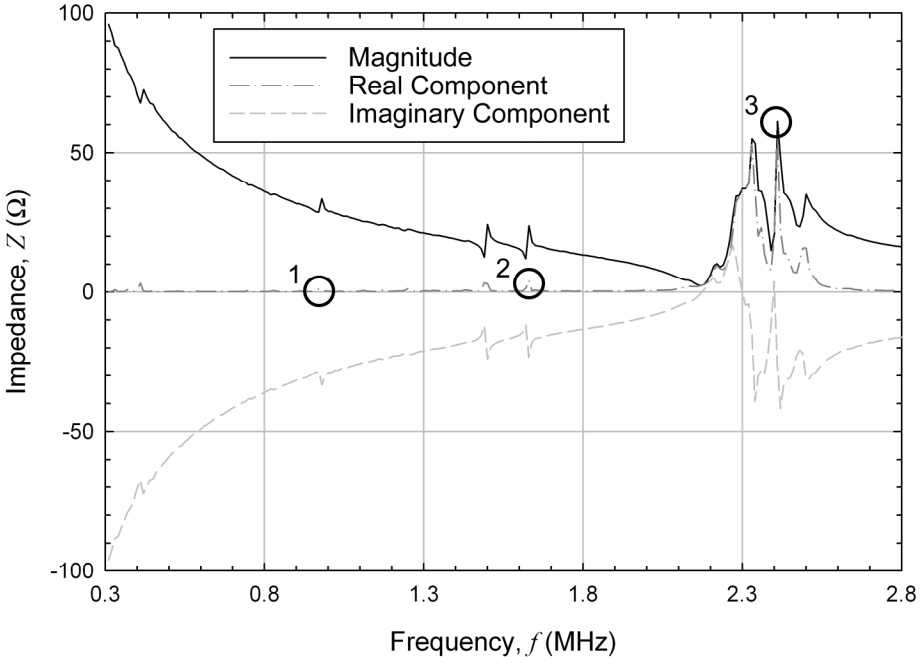

Figure 2.2. Predicted electrical input impedance as a function of transducer frequency for a 1 mm thick lead zirconate titanate (PZT-8) piezoelectric transducer driving a water-loaded device with a 500 μm thick silicon ejector plate and a 500 μm thick spacer. The first three resonant modes corresponding to acoustic wave focusing are highlighted.

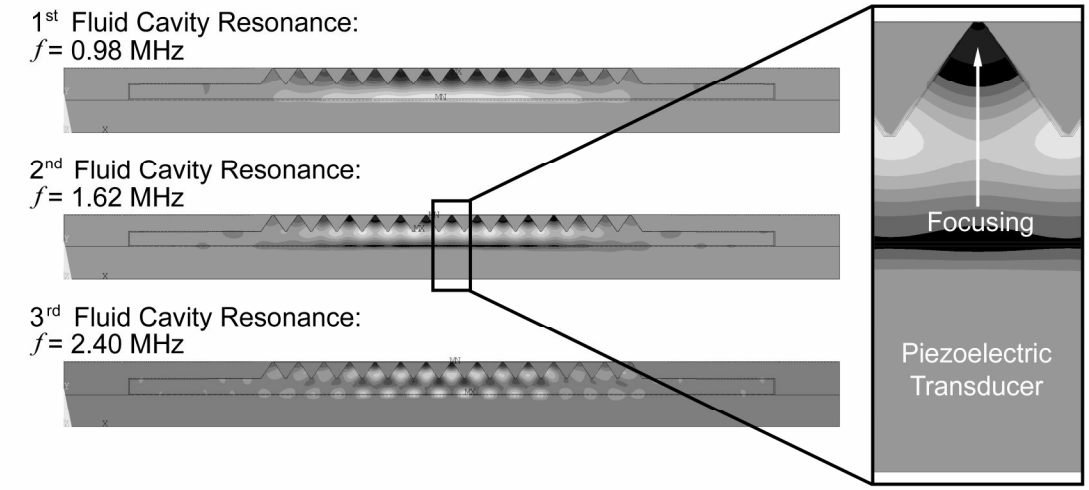

Figure 2.3. Pressure fields within the fluid chamber of a water-loaded device driven at the first three resonant modes that result in acoustic wave focusing at the nozzle tips. The device comprises a 1 mm thick lead zirconate titanate (PZT-8) piezoelectric transducer with a 500 μm thick silicon ejector plate and a 500 μm thick spacer.

2.4 Device Fabrication

Figure 2.4 depicts the baseline, two-mask fabrication process flow for an ejector array.[34] It comprises two main steps: (1) the creation of an array of pyramidally-shaped horns and (2) the opening of precisely defined orifices at the tips of these horns. Each of these processes is further subdivided into the individual processing steps shown in Figure 2.4.

2.4.1 Baseline Fabrication Process

In general, since the silicon wafer may be contaminated, dry organic cleaning is performed in an oxygen plasma using a reactive ion etcher (RIE), or the silicon wafer is

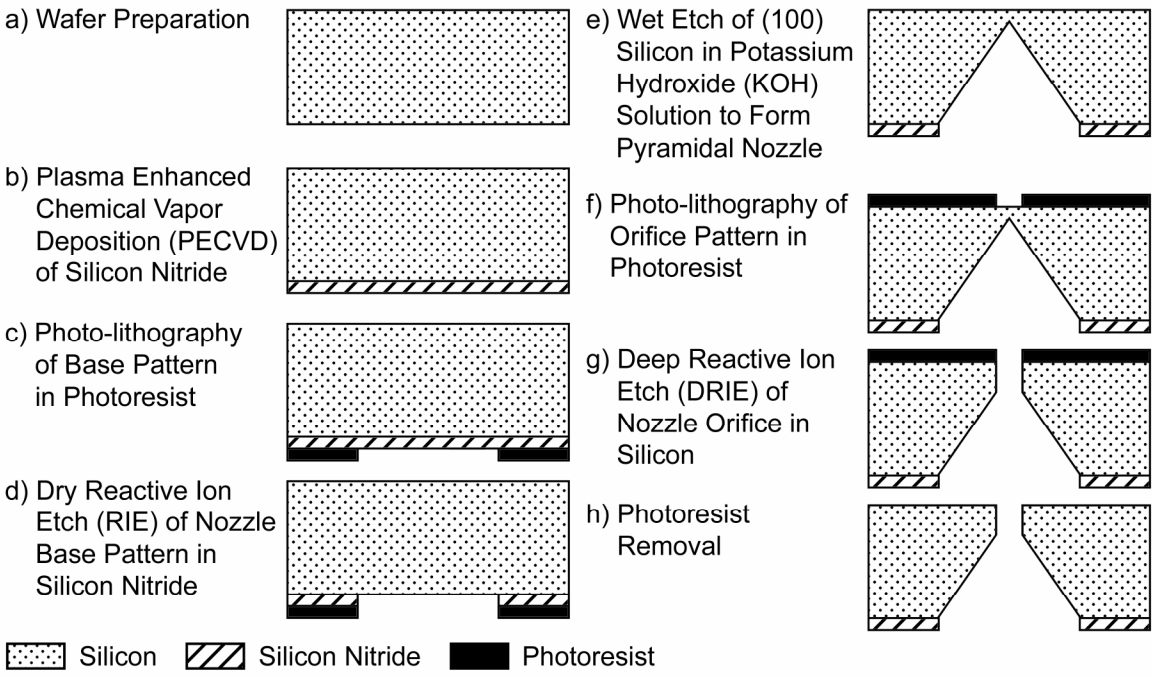

Figure 2.4. Baseline ejector fabrication process: a) wafer preparation, b) deposition of silicon nitride (Si_3N_4) to act as a mask during the wet etch, c) photo-lithography of base pattern, d) Si_3N_4 reactive ion etch (RIE) to form the base of the nozzle, e) formation of a pyramidal nozzle in single crystal (100) oriented silicon by anisotropic wet etch in a potassium hydroxide (KOH) solution, f) photo-lithography of orifice pattern, g) creation of the orifice in the silicon using a deep reactive ion etch (DRIE), and h) removal of photoresist.

dipped in a 4:1 solution of 98% sulfuric acid (H_2SO_4) and 30% hydrogen peroxide(H_2O_2) to remove photoresist residue and oil from its surface before beginning fabrication.

Approximately 1 μm of silicon nitride (Si_3N_4) is deposited over the entire silicon wafer using plasma enhanced chemical vapor deposition (PECVD) in a Surface Technology Systems (STS) Multiplex CVD (Figure 2.4b). The etch rate of Si_3N_4 in potassium hydroxide (KOH) is negligible so this layer acts as a protective mask during the wet etch of the pyramidal nozzles. Nitride deposition occurs at a rate of ~330 Å/min as silane (SiH_4) and ammonia (NH_3) react in a radio frequency (RF) induced plasma to form Si_3N_4 on the silicon surface.

An array of squares with side length equal to that of the base of a pyramidal nozzle is defined on the back side of the wafer using standard photo-lithography techniques (i.e., spin coating, pattern exposure, and feature development) and then dry-etched through the Si_3N_4 masking layer in a Plasma-Therm SLR Series dual ICP using the RIE process (Figures 2.4c and 2.4d). The RIE of the Si_3N_4 consists of etching in a tetrafluoromethane (CF_4) environment at an etch rate of ~2000 Å/min. The anisotropic nature of the KOH etch yields features with slanted sidewalls at an angle of 54.74° to the surface of a single crystal silicon wafer oriented with the (100) plane (Figure 2.4e); therefore, for a nominal 500 μm wafer thickness, each side of the square feature representing the base of a nozzle must be approximately 700 μm in order to form a pyramid that terminates before etching through to the opposite side of the wafer. The wet etch occurs in a 45 weight-percent solution of KOH in water at a temperature of 75°C. Under these conditions, the etch rate is approximately 0.5 μm/min; however, the etch rate

decreases as the etch nears the opposite side of the wafer yielding a total etch time of 18–20 hours.

After completion of the KOH wet etch, standard photo-lithography techniques are used to define the size and shape of the nozzle orifices and to locate them on the opposite side of the wafer (Figure 2.4f). The orifices are then etched through the bare silicon using a deep reactive ion etch (DRIE) in a process similar to that used to create the square features representing the nozzle base array (Figure 2.4g).

2.4.2 Improved Fabrication Process

Even though the diameter of the nozzle orifices is dictated by the frontside lithography and DRIE in the baseline fabrication process, the high degree of variability associated with the anisotropic wet etch of silicon does not allow for control of the length of the channels located in the silicon at the tips of the nozzles, and this has a significant effect on the performance of the device. To improve process control and to reduce the influence of the wet etch, the baseline process is modified as shown in Figure 2.5.

As in the baseline process, 1 μm of Si_3N_4 is deposited on the back side of the wafer using PECVD in a Surface Technology Systems (STS) Multiplex CVD. A Unaxis 790 Series PECVD is then used to deposit a 2 μm layer of Si_3N_4 on the opposite (front) side of the wafer to serve as an etch stop for the wet etch, which is designed to leave thin membranes at the tips of the nozzles (Figure 2.5b). The deposition rate in the Unaxis PECVD is only ~80 Å/min; however, this machine allows the ratio of helium (He) to nitrogen (N_2) in the ambient to be adjusted to control the stress in the resulting nitride layer which is important for creation of stress-free membranes.

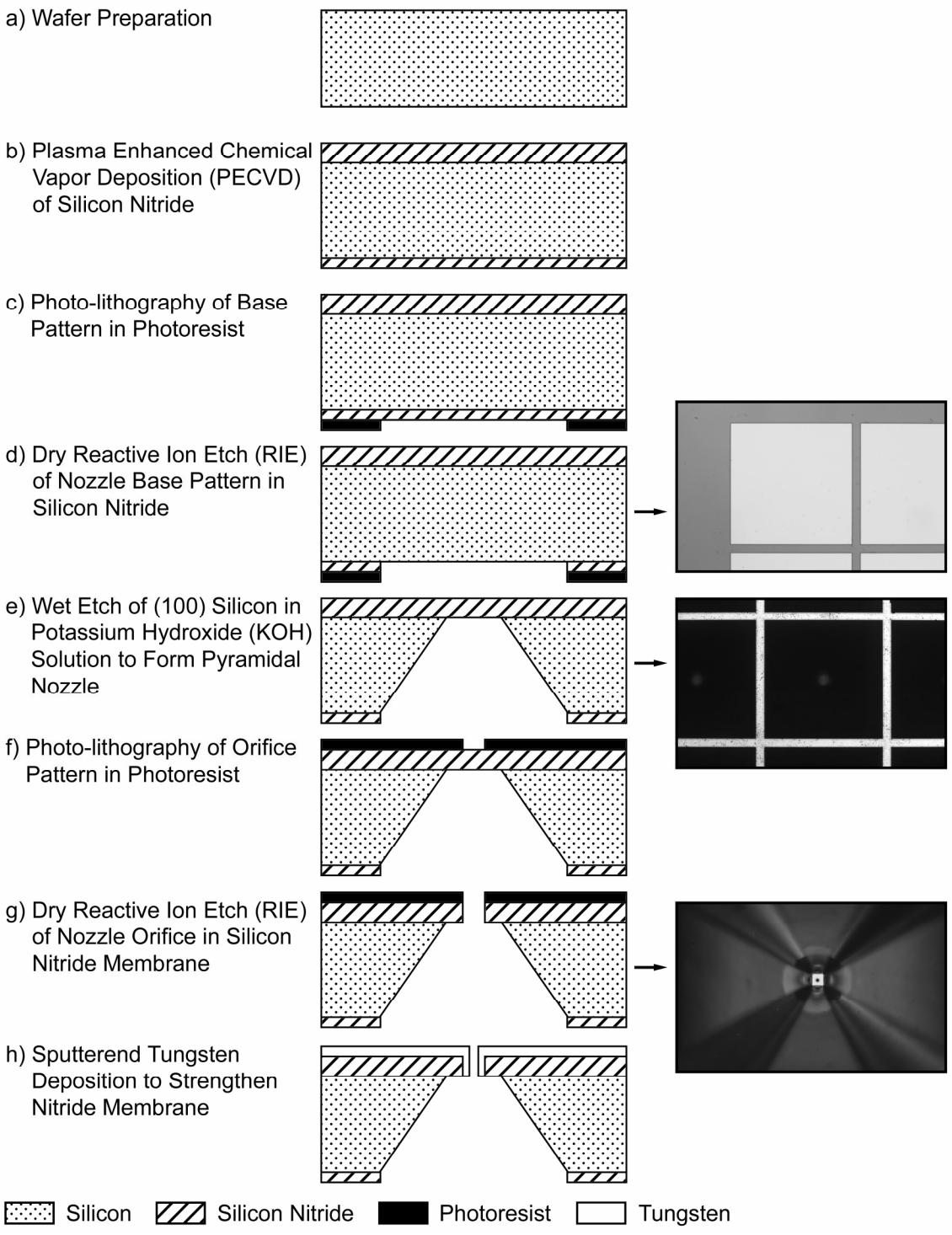

Figure 2.5. Final ejector fabrication process: a) wafer preparation, b) deposition of silicon nitride (Si_3N_4) to act as a mask during the wet etch and as a membrane for orifice creation, c) photo-lithography of base pattern, d) Si_3N_4 reactive ion etch (RIE) to form the base of the nozzle, e) formation of a pyramidal nozzle in (100) oriented silicon by anisotropic wet etch in a potassium hydroxide (KOH) solution, f) photo-lithography of orifice pattern, g) creation of the orifice in the nitride membrane using RIE, and h) tungsten deposition to strengthen the nitride membrane.

The size of the pyramidal nozzles is dictated by etching an array of squares in the Si_3N_4 masking layer. Figure 2.5d provides an optical microscope image of bare silicon squares separated by silicon nitride lines indicating that the nitride has etched completely through. The anisotropic KOH etch is again used to form the pyramidal nozzles; however, now the size of the square feature representing the base of a nozzle is increased so that the KOH solution etches the silicon completely and reaches the nitride layer on the front side of the wafer. The nitride lattice present on the back side of the wafer after the wet etch is shown in the optical microscope image in Figure 2.5e; the membranes are also seen as slightly brighter regions at the center of the black squares which indicates that the silicon etch is complete and reaches the nitride layer at the opposite side of the silicon wafer.

After completion of the KOH wet etch, the nozzle orifices are patterned on the opposite (front) side of the wafer at the center of the nitride membranes (Figure 2.5f). The orifices are then etched through the membranes using the RIE process (Figure 2.5g) in the same way as the square features representing the nozzle base array (Figure 2.5d). A 5 μm orifice located in the center of an 11 μm membrane is shown from the back side in the optical microscope image in Figure 2.5g. By controlling the size of the pyramid bases, the membranes are made only slightly larger than the orifices so that they are very rigid; yet, a CVC Model 601 DC sputterer is used to deposit a 0.5 μm thick layer of tungsten over the front side of the ejector to further strengthen the membranes and to ensure that they do not break during operation (Figure 2.5h). A 300 Å seed layer of titanium is necessary to ensure that the tungsten layer has good adhesion to the nitride.

The sputtering process leaves a fairly conformal coating on the ejector orifices, and it effectively reduces the diameter of the orifices by the thickness of the tungsten layer.

2.4.3 Photomask Layout

The two-step fabrication process requires one photomask for creating the base pattern for the pyramidal nozzle array and a second mask for defining the orifices on the opposite side of the wafer. Figure 2.6 shows the layout for each of these masks. Note that the dark areas in Figure 2.6 represent open areas on the masks. The masks are designed such that six devices are created from a single 100 mm (4") diameter silicon wafer. Although not present on the actual masks, the wafer outline is shown in Figure 2.6 for reference. Because some of the photo-lithography steps require that the wafer is held at its center, this space is not used for device fabrication.

Three mask features are used specifically for alignment purposes. The first is a line located at the bottom of the backside mask that is used to align the square base array to the primary wafer flat and thus to the (110) plane of the silicon wafer. Alignment of the orifices to the membranes located at the tips of the pyramids is accomplished using the coarse and fine alignment marks. Although a frontside alignment technique is currently used, the fine alignment marks are located such that backside microscopes could be used to perform a backside alignment if necessary. Specifics of the frontside alignment procedure are discussed in Section 2.4.5.

After completion of the fabrication process, the wafer is diced to yield six ejector plates. Figure 2.7 provides photographs of the front and back sides of a nozzle array that was fabricated using the two mask process. The 500 μm thick square plate is 24 mm on a

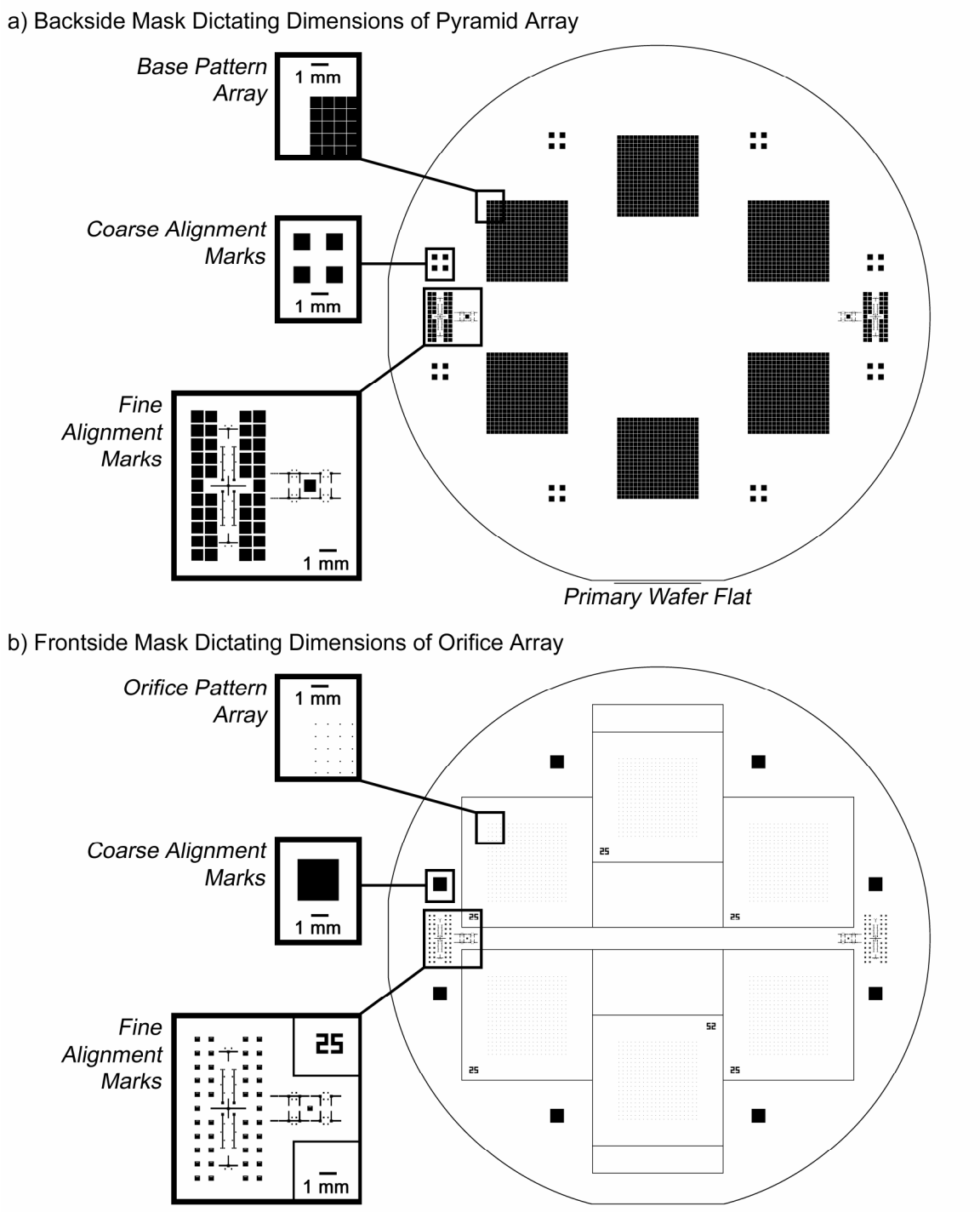

Figure 2.6. Back and frontside photomasks: a) backside mask used to define the size and location of the array of squares representing the bases of the pyramidal nozzles and b) frontside mask used to define the size and shape of the orifices and to locate them at the tips of the pyramids.

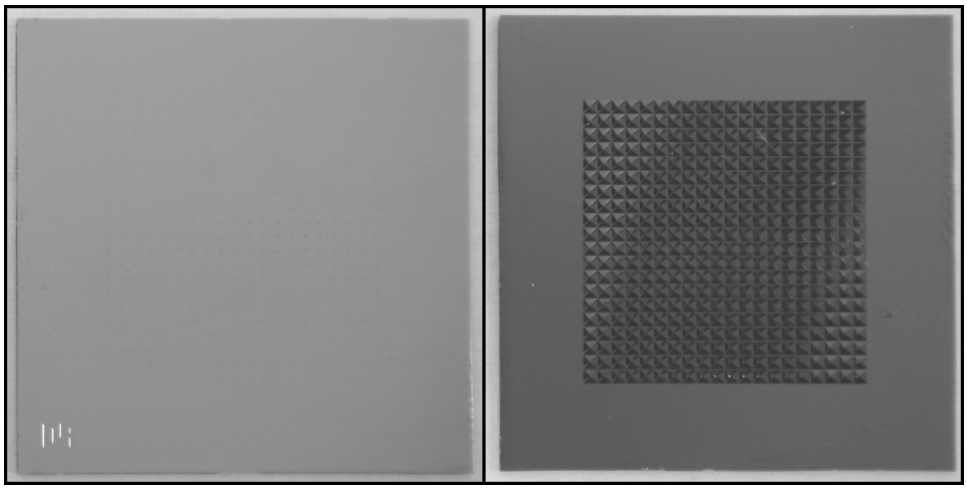

Figure 2.7. Photographs of the front (left) and back (right) sides of a completed ejector plate.

side, and hosts the 20x20 array covering an area of approximately 15x15 mm. During the RIE of the orifices, an identification number representing the nominal orifice size is also etched through the nitride so that individual devices are easily identified. Although it is difficult to distinguish in Figure 2.7, a small "09" is located in the lower left-hand corner of the front face of the device. The nozzle array shown in Figure 2.7 was created using the improved fabrication process described above. In the course of the development of this fabrication process, a number of technical issues have been addressed both with creation of the pyramidally-shaped nozzles and opening of the nozzle orifices, particularly the alignment of the orifices etched from the front side to the tips of the pyramids etched from the back side.

2.4.4 Creation of the Pyramidally-Shaped Nozzle Array

In the first version of the fabrication process, the ejector orifices were opened up naturally by etching completely through the silicon wafer in the KOH solution;[34] however, despite the attractive simplicity of this method, the through-wafer KOH wet etch yields inconsistent results with respect to the nozzle orifice size as the etch rate of

the silicon is difficult to control and there are a number of issues associated with alignment. Figure 2.8 provides a general overview of challenges associated with precise feature creation in (100) oriented silicon using a solution of KOH in water. In order for the mask to accurately prescribe the size of the pyramids in the nozzle array, the square features representing the bases of the pyramids must be perfectly aligned to the (110) plane of the silicon. This is accomplished by aligning the entire mask to the primary wafer flat using the line located at the bottom of the backside mask shown in Figure 2.6. The tolerance for the primary wafer flat is ±1° to the (110) plane so even if the mask is perfectly aligned, the size w_{actual} of the resulting feature will be larger than the desired size w_{mask} as shown in Figure 2.8a.[33] Because the etch rate $R_{<111>}$ in the <111> direction is not truly zero, the (111) plane etches slightly during a through-wafer etch (Figure 2.8b). The resulting under-etch of the nitride layer compounds the problems associated with alignment and causes further enlargement of the features; therefore, the size of the orifices created using the KOH etch alone cannot be controlled with satisfactory precision, and a second mask is needed to create orifices of a precise diameter.

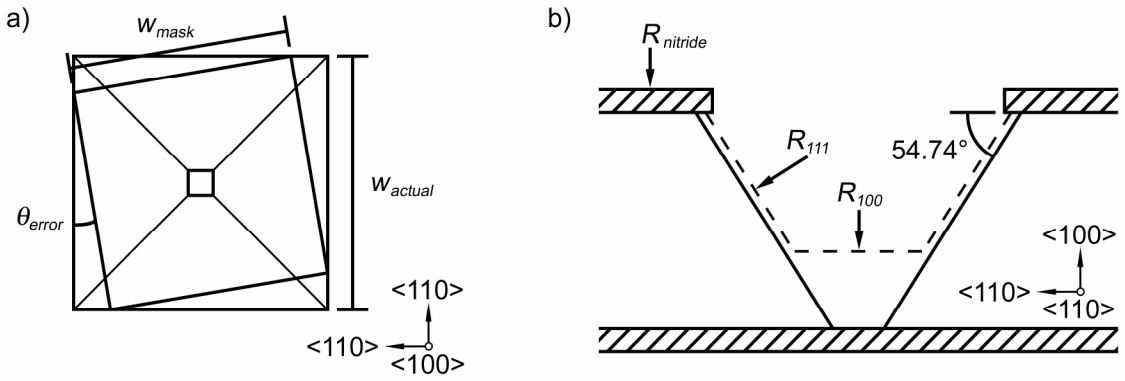

Figure 2.8. Anisotropic etching of (100) oriented silicon in a potassium hydroxide (KOH) solution: a) effect of misalignment of the primary wafer flat to the <110> direction and b) preferential etching of the (100) plane as compared with the (111) plane.

As discussed previously, a square feature with side length of approximately 700 μm should ideally create a pyramid that just reaches the opposite side of a 500 μm thick (100) oriented single crystal silicon wafer without opening a through hole; however, due to the practical issues described above, the resulting pyramids actually terminate at the nitride etch stop layer forming a square membrane that is approximately 5–10 μm on a side. Since a single backside mask is used to create the pyramidal nozzle array for devices with a range of orifice sizes, the side length for the square features representing the nozzle base array is designed to be 700 μm. This allows the size of the nitride membranes created on the front side of the wafer upon completion of the wet etch to be dictated by the thickness of the silicon wafer, which can vary from 475–525 μm. Due to the under-etch of the nitride layer during the KOH etch, the pitch of the nozzles is set at 750 μm. The 50 μm spacing between nozzles ensures that no neighboring nozzles come into contact during the etch.

2.4.5 Opening of the Orifices

A second mask is used to open up the orifices at each nozzle termination point allowing for greater control of the orifice size and shape. Initially, a backside alignment technique was used to locate the nozzles. After performing the anisotropic wet etch, an image of the back side of the wafer was captured using backside microscopes on a Karl Suss MA-6 mask aligner. The frontside mask was then aligned to this image to properly place the orifices. Unfortunately, the mask aligner could shift the image by as much as 30 μm. Sometimes the alignment was successful but this was unpredictable. The devices could not be used if the orifices were misaligned significantly.

When using the backside alignment technique, the alignment marks were protected during the wet etch because the KOH solution would significantly alter the fine alignment features after an extended exposure time. In order to avoid this problem, the alignment marks were modified to take advantage of the anisotropic nature of the wet etch. The alignment marks on the current backside mask consist of two arrays of square features. The first set shown in Figure 2.6 is used for coarse alignment, and the second set is used for fine alignment. The square features in the first array are large enough so that the KOH solution etches completely through the wafer leaving four large 300x300 μm nitride membranes that are visible from the frontside of the wafer. The side lengths of the square features in the second set of fine alignment marks range in size from 685 to 735 μm in 5 μm increments; therefore, after the wet etch, a set of nitride membranes that ranges in extent from a maximum of 20–30 μm down to sub-5 μm is created on the opposite side of the wafer. During alignment, the sets of large membranes on the left and right side of the wafer are first centered in the large open windows on the frontside mask. The smaller membranes are then aligned to match concentric square features making up the fine alignment marks on the frontside mask. One of the four large membranes is shown in its aligned position in Figure 2.9a. Figure 2.9b shows four of the smaller membranes aligned with the fine alignment marks. Note that these images were taken after the final etch step so the alignment features have been dry etched into the front side of the wafer.

In the baseline, two-step fabrication process, the wet etch was designed to terminate before reaching the opposite side of the wafer; the orifices were etched through

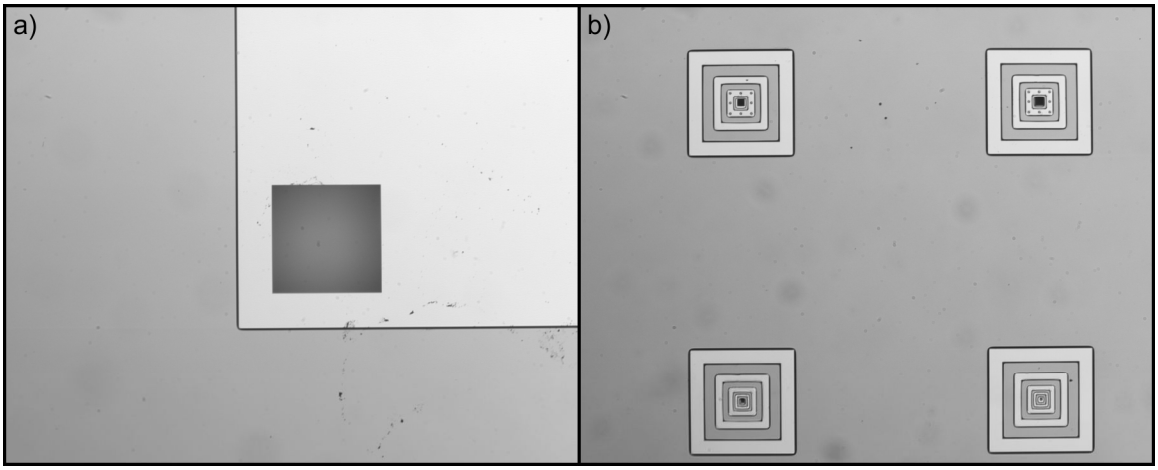

Figure 2.9. Frontside alignment features: a) rough alignment features and b) fine alignment features in aligned position.

the remaining silicon using an RIE, and a short channel was created at the tips of the pyramidal nozzles. In this case, it was not possible to tell if the orifices were properly aligned until after the RIE was completed. Locating the orifices in thin membranes alleviates some of the alignment issues (i.e., if the orifice is not aligned properly, it is possible to see that it is misaligned before etching); however, it introduces problems associated with the structural integrity of the nozzle array. If the size of the orifice is not well matched to that of the membrane or if the membrane is large in extent as compared to the orifice size, the membranes may break during device operation at high power input. Figure 2.10 provides optical microscope images of an array of broken nitride membranes observed from the backside of a wafer. In all cases, failure appears to occur at the edges of the membranes. Note that in this case the orifice size was well matched to that of the membrane, but the device was driven at a much higher power input level than was necessary for ejection.

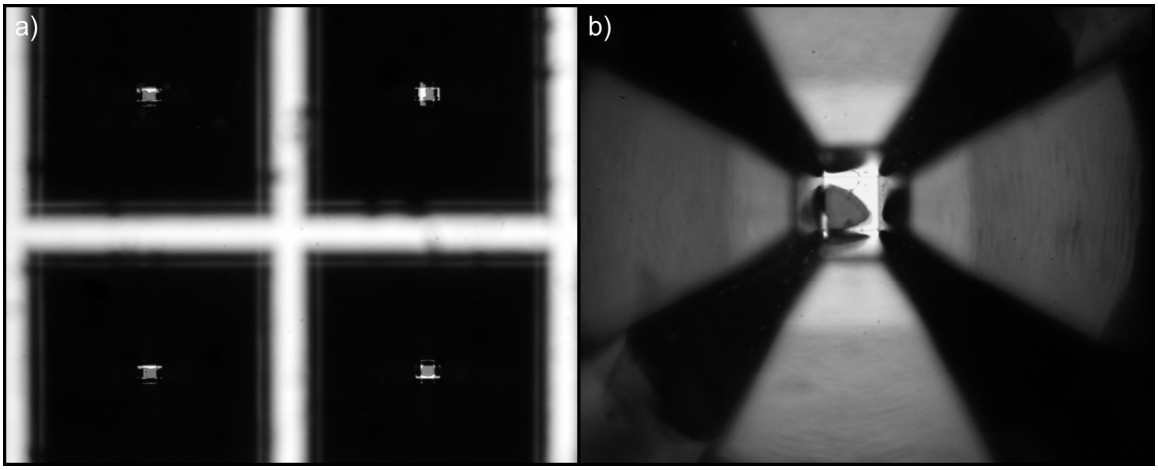

Figure 2.10. Broken nitride membranes: a) array of four broken membranes and b) high resolution optical microscope image of a single broken membrane.

2.4.6 Comparison of Realized Devices

Depending upon the thickness of the wafer, the improved (final) fabrication process described in Figure 2.5 yields devices with orifices located either in nitride membranes or in bulk silicon at the tips of the pyramidal nozzles. Figure 2.11 provides scanning electron microscope (SEM) images of devices created both with and without membranes. A ~480 μm thick wafer was used to create the device shown in Figure 2.11a. After the KOH wet etch, an array of 15.5 μm diameter orifices was etched through the resulting 2.5 μm thick, 26 μm wide square nitride membranes. The device shown in Figure 2.11b was created using a ~500 μm thick wafer. The tips of the resulting pyramids terminated 1–2 μm before reaching the membrane layer at the front side of the wafer. After using an RIE to etch through the nitride layer, a DRIE process was performed to create short 6 μm diameter channels in silicon to reach the tips of the pyramids.

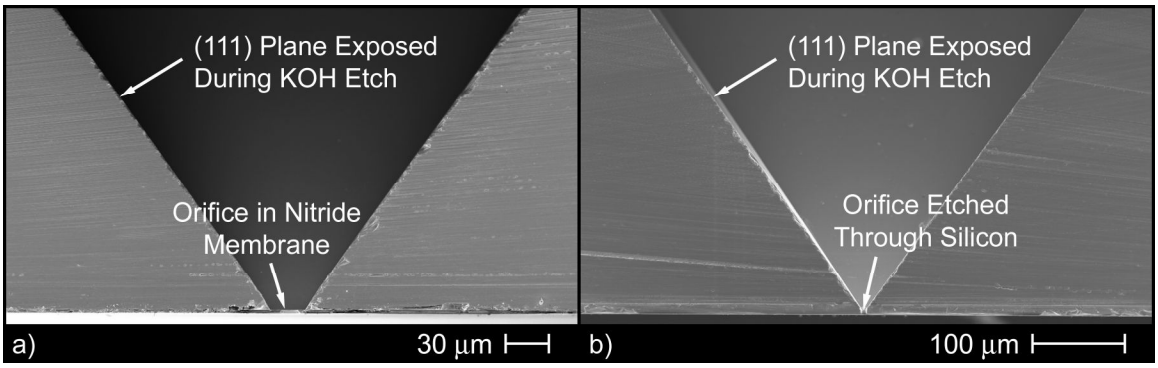

Figure 2.11. Scanning electron microscope (SEM) images of devices fabricated with and without membranes: a) 15.5 μm diameter orifice created in a 2.5 μm thick, 26 μm wide square silicon nitride (Si_3N_4)/tungsten membrane and b) 6 μm orifice etched through bulk silicon.

As was mentioned earlier, there are advantages and disadvantages associated with each of these fabrication sequences and resulting device structures. The biggest advantage of not having a membrane is increased robustness of the nozzle plate. Figure2.11 also indicates that the tips of the pyramids created in devices without membranes comes to a sharper point which may improve focusing of the acoustic waves and increase the resulting pressure gradient at the nozzle orifices; however, the introduction of even a very short channel significantly increases the pressure drop which needs to be overcome to enable fluid ejection and this may offset any acoustic wave focusing benefit.

High resolution SEM images of a 4.5 μm diameter orifice etched in an 11 μm wide square membrane are shown in Figure 2.12. The cross section shown in Figure 2.12a indicates that the nitride and tungsten layers have uniform thicknesses of 2.0 and 0.5 μm, respectively; however, the tungsten deposited on the walls of the orifice appears to increase the surface roughness significantly and could have an impact on the ejection process especially for smaller orifices. The view from the back side of the device in

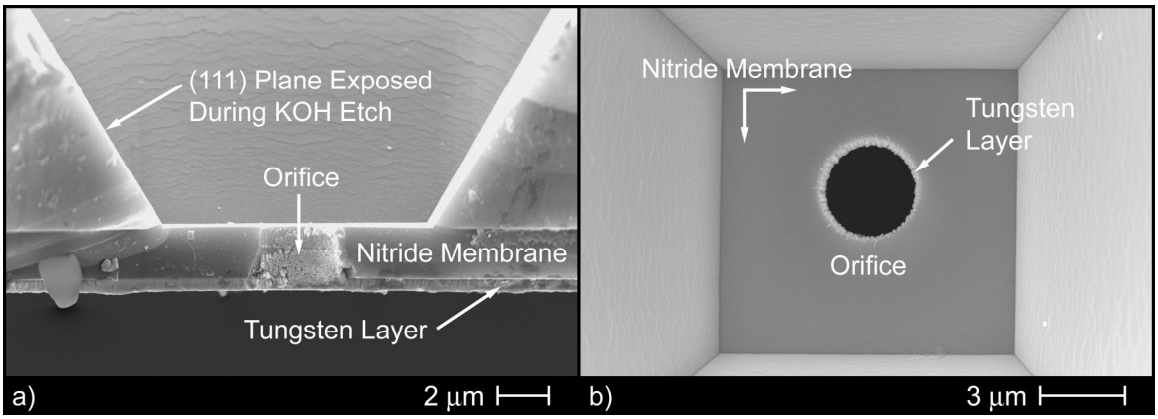

Figure 2.12. Scanning electron microscope (SEM) images of a 4.5 μm diameter orifice in a 2.5 μm thick, 11 μm wide square silicon nitride (Si_3N_4)/tungsten membrane: a) cross section and b) view from the back side of the device.

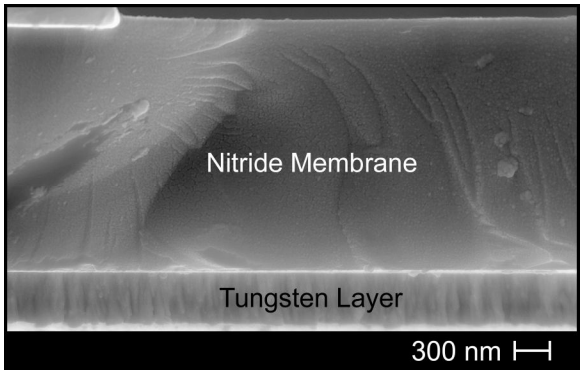

Figure 2.13. Scanning electron microscope (SEM) image of the silicon nitride(Si_3N_4)/tungsten membrane.

Figure 2.12b shows the orifice to be well-aligned close to the center of the membrane. It also indicates that the tungsten layer decreases the diameter of the orifice by approximately 0.5 μm. Figure 2.13 provides a closer look at the structure of the nitride membranes. The nitride layer appears to be highly amorphous whereas the tungsten layer appears to have a grainy structure which could indicate a lower quality film.

High resolution SEM images of a 6 μm orifice created in bulk silicon are shown in Figure 2.14. Again, the surface roughness of the channel formed in the silicon is high;

however, the side walls of the orifice in the nitride layer appear smooth. The channel roughness is due to the DRIE process. Deep reactive ion etching utilizes the Bosch process to alternate between an etch step and deposition of a protective polymer layer. Each cycle of the process removes approximately 0.5 μm of silicon which causes the sidewalls to become scalloped at this interval as seen in Figure 2.14a. The view from the back side of the device shown in Figure 2.14b indicates that the orifice is almost perfectly centered on the tip of the pyramid. It also appears that the transition from the pyramidal horn to the nozzle orifice is not smooth because the surface has been roughened by DRIE-induced scalloping.

2.5 Concluding Remarks and Discussion of Future Design Work

In this chapter, the proposed droplet generation concept has been shown to address the challenges associated with conventional atomization techniques. A high degree of control of the atomization process with low-power and low-temperature operation is achieved with a flexible, low-cost device. Two device designs have been fabricated, and both successfully meet the desirable attributes of an atomization technique

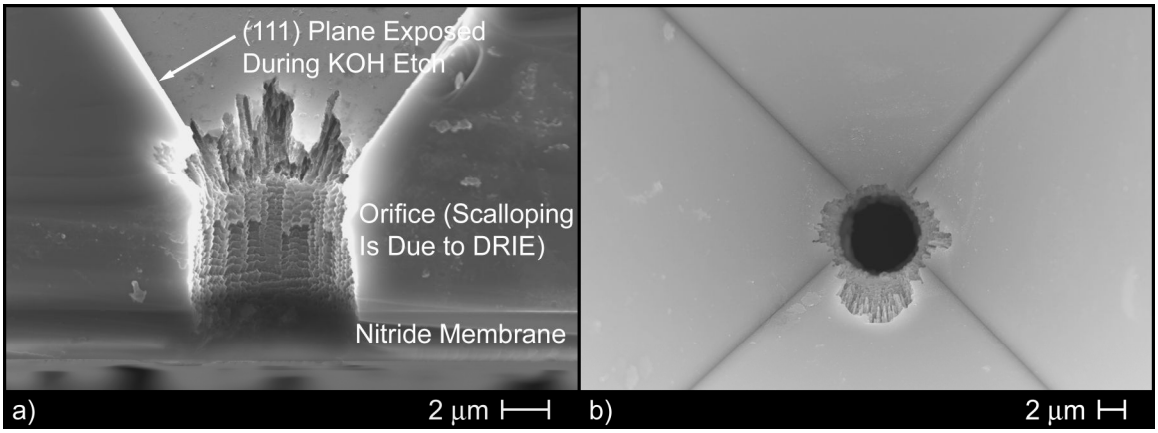

Figure 2.14. Scanning electron microscope (SEM) images of a 6 μm diameter orifice created in bulk silicon: a) cross section and b) view from the back side of the device.

for any operating fluid. The devices perform well in ejection of typical low viscosity, high surface tension fluids such as water. Successful operation has also been demonstrated using higher viscosity (up to ~50 cp) mixtures of glycerol and water and low surface tension (0.025 N/m) methanol; however, ejection of each of these fluids presents challenges that may require refinement of the ejector design.

Low surface tension liquids tend to weep from the nozzle orifices and cover the front surface of the device, thereby hindering ejection. By modifying the surface properties of the ejector, e.g., coating the top surface with a hydrophobic material (Parylene C), this problem has been reduced but not eliminated. Characterization of additional surface materials should be conducted, and if weeping cannot be controlled, it may be necessary to change the design of the nozzle orifice. For example, Luginbuhl *et al*.[12] created nozzles with a ring-shaped lip in order to minimize the weeping effect.

Ejection of high viscosity liquids requires generation of a larger pressure gradient near the nozzle tip to overcome significant viscous losses at the orifice. By fabricating the orifices in thin nitride membranes, the input power requirement is reduced; however, the likelihood of the membranes breaking during device operation is increased. This issue needs to be analyzed in greater detail to find the best compromise between device robustness and power consumption.

CHAPTER 3

SIMULATION OF DEVICE OPERATION

The acoustic simulation package of the commercial finite element analysis code ANSYS[36] is used to predict the frequencies of the device resonances and at which of the resonant frequencies acoustic pressure field focusing occurs within the fluid cavity formed by the fluid reservoir and nozzle array. The simulations also yield an estimate of the fraction of the electrical input power to the piezoelectric transducer that is imparted to the fluid upon ejection; therefore, the simulations not only confirm the behavior of the acoustic wave focusing horn, but are also used to identify the resonant frequencies and desired geometry for optimum device operation.

3.1 Problem Setup

The problem solution is obtained using a harmonic response analysis over the frequency range (0.3–2.8 MHz) of interest. The pressure field generated in the fluid chamber by the periodic excitation of the piezoelectric transducer, and its interactions with the silicon spacer and ejector plate are simulated. It is assumed that all loads and displacements vary sinusoidally at the same known frequency. Using the default solver options, the harmonic response analysis is used to solve the second order (in time) equations of motion governing the structural response of the silicon and the acoustic response of the fluid chamber, and the mixed order (e.g., electrical and structural) equations governing the dynamics of the piezoelectric transducer.[36] This analysis is accurate because only a small amount of energy is transferred to the ejected fluid, leaving the linear acoustic field mostly unperturbed.

3.1.1 Simulation Domain

The ejector simulations are performed for the two-dimensional (2-D) and three-dimensional (3-D) domains shown in Figures 3.1 and 3.2, respectively. For simulations performed in the 2-D domain, the thickness t_{Si} of the silicon ejector plate and the width w_{piezo} of the piezoelectric transducer are set to 500 μm and 24 mm, respectively. The thickness t_{spacer} of the silicon spacer dictates the height of the fluid cavity and therefore its resonant frequencies. Simulations are performed for spacer thicknesses of 0.5, 0.63, and 1.5 mm which correspond to an envelope of resonant frequencies ranging from 0.47 to 2.40 MHz. The thickness t_{piezo} of the piezoelectric transducer is chosen such that its first longitudinal resonance lies within this frequency range. Specifically, transducer thicknesses of 1 and 2 mm corresponding roughly to resonances at 2.25 and 1.12 MHz, respectively, are used in the simulations. Since the thickness of the silicon ejector plate is the same for all of the simulations, the width w_{base} of the base of the triangular nozzles is used to dictate whether or not the nozzles terminate in a membrane or a channel (insets, Figure 3.1). A base width of 705 μm yields a 5 μm long, 5 μm wide channel at the tips of the nozzles. An increased base width of 720 μm results in 13 μm wide nitride membranes. The diameter d_o of the nozzle opening is 5 μm for all cases.

As shown in Figure 3.1, a variable density mesh is used so that the pressure wave focusing close to the nozzle orifice can be properly resolved. A convergence study was conducted to ensure that the results are independent of the mesh size. Regardless whether a channel or membrane structure at the nozzle tip is simulated, the mesh density ranges from approximately six elements per mm at the bottom surface of the piezoelectric

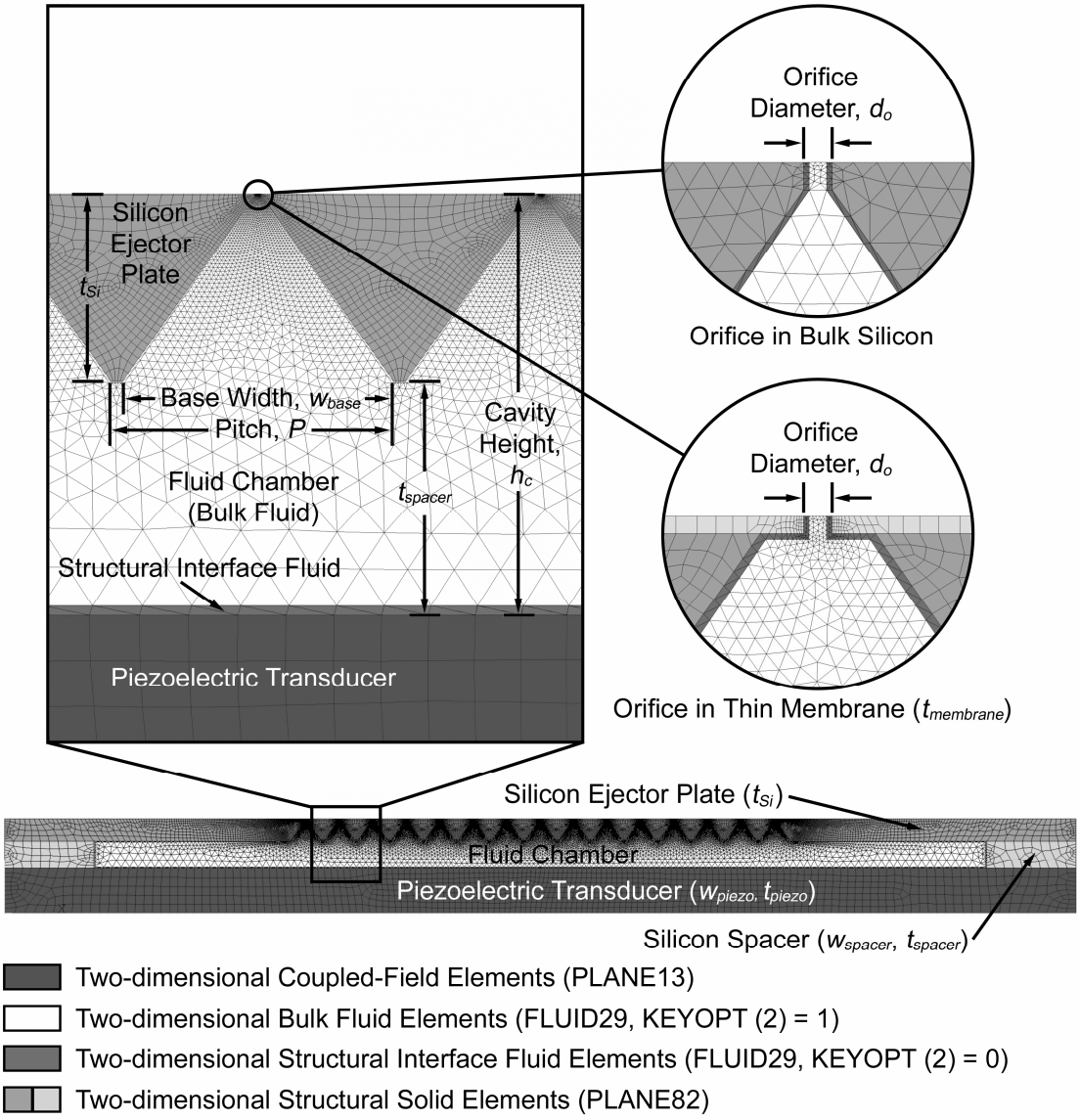

Figure 3.1. Two-dimensional (2-D) computational domain used to perform simulations of the harmonic response of the system using ANSYS.[36]

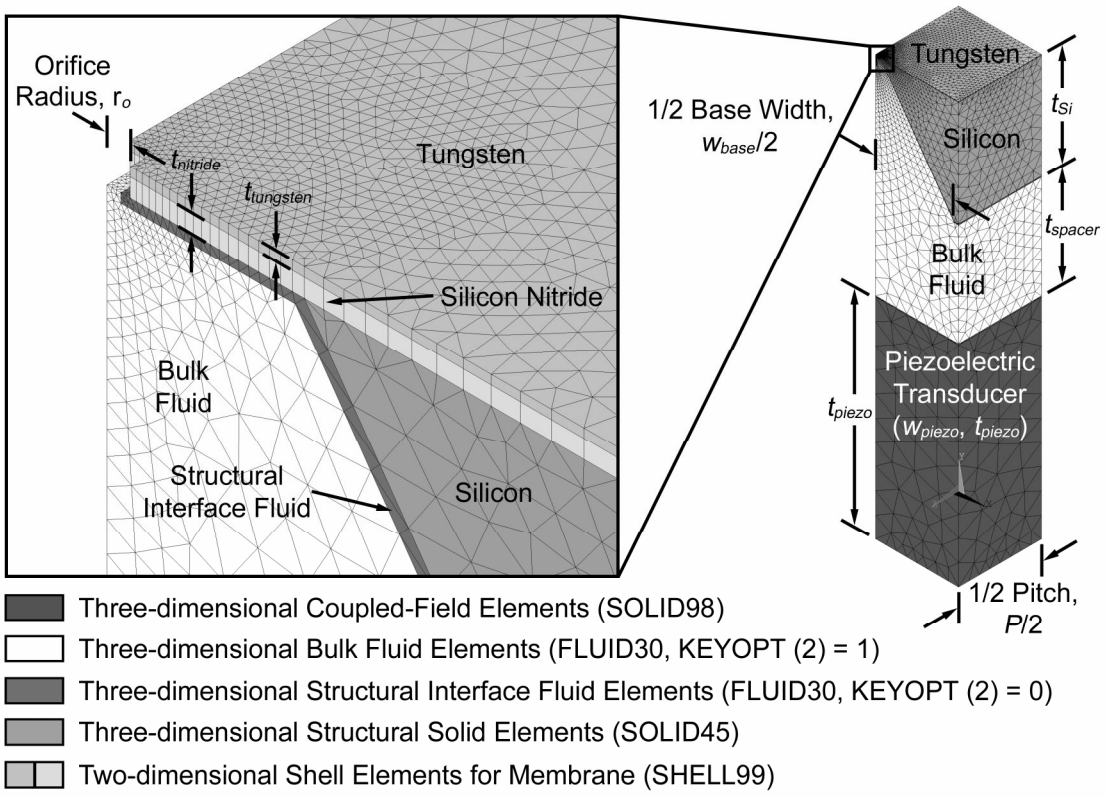

Figure 3.2. Three-dimensional (3-D) computational domain used to perform simulations of the harmonic response of the system using ANSYS.[36]

transducer to 750 elements per mm at the nozzle orifice. The element types coupled-field solid (PLANE13), bulk fluid (FLUID29 (KEYOPT (2) = 1)), structural interface fluid (FLUID29 (KEYOPT (2) = 0)), structural solid (PLANE82) and shell membrane (SHELL99) are discussed in subsequent sections of this thesis.

Because the simulations performed in the 3-D simulation domain are only used to confirm that the acoustic wave focusing predicted by the 2-D simulations accurately represents that of the actual device, 3-D simulations are conducted for a single device geometry. The thickness t_{Si} of the silicon ejector plate and the thickness t_{spacer} of the spacer are set to 500 μm, and the thickness t_{piezo} of the piezoelectric transducer is set to 1 mm. The 3-D domain represents one-quarter of the actual nozzle so the side length of the

square piezoelectric element is set to 395 μm, which is half of the nozzle pitch P. The half-width of the nozzle is set to 375 μm, which results in a membrane that has a half-width of 20 μm. The radius r_o of the nozzle opening is set to 2.5 μm.

Again, a variable density mesh is used to resolve the pressure wave focusing close to the nozzle as shown in Figure 3.2. The mesh density ranges from 25 elements per mm at the bottom surface of the piezoelectric transducer to 1000 elements per mm at the nozzle orifice. The element types coupled-field solid (SOLID98), bulk fluid (FLUID30 (KEYOPT (2) = 1)), structural interface fluid (FLUID30 (KEYOPT (2) = 0)), and structural solid (SOLID45) are discussed in subsequent sections of this thesis.

3.1.2 Modeling the Piezoelectric Transducer

The lead zirconate titanate (PZT-8) material comprising the piezoelectric transducer is characterized by a coupling of structural and electric fields; therefore, the piezoelectric material deforms under an applied voltage, and an applied displacement generates a potential difference. The coupled-field behavior of the piezoelectric material is described by the strain-charge form of the constitutive equations given by

$$\mathbf{S} = \mathbf{s}_{\mathbf{E}} \cdot \mathbf{T} + \mathbf{d}^{t} \cdot \mathbf{E} \quad \text{and} \tag{1}$$

$$\mathbf{D} = \mathbf{d} \cdot \mathbf{T} + \boldsymbol{\varepsilon}_{\mathbf{T}} \cdot \mathbf{E} \,. \tag{2}$$

Equations (1) and (2) define how the stress **T**, strain **S**, charge-density displacement **D**, and electric field **E** of the material interact.[37] The piezoelectric strain matrix **d** contains the piezoelectric coupling coefficients, $\mathbf{s}_{\mathbf{E}}$ is the compliance matrix, and $\boldsymbol{\varepsilon}_{\mathbf{T}}$ is the electric permittivity matrix.

PZT-8 is transverse isotropic, i.e., the material properties in the unpolarized directions are the same and differ from those of the polarized direction; therefore, only five independent variables are needed to completely define the compliance matrix $\mathbf{s_E}$.[37]

$$\mathbf{s_E} = \begin{vmatrix} \frac{1}{E_p} & \frac{-\nu_p}{E_p} & \frac{-\nu_{zp}}{E_z} & 0 & 0 & 0 \\ \frac{-\nu_p}{E_p} & \frac{1}{E_p} & \frac{-\nu_{zp}}{E_z} & 0 & 0 & 0 \\ \frac{-\nu_{pz}}{E_p} & \frac{-\nu_{pz}}{E_p} & \frac{1}{E_z} & 0 & 0 & 0 \\ 0 & 0 & 0 & \frac{1}{2G_{zp}} & 0 & 0 \\ 0 & 0 & 0 & 0 & \frac{1}{2G_{zp}} & 0 \\ 0 & 0 & 0 & 0 & 0 & \frac{(1+\nu_{p)}}{E_p} \end{vmatrix} \quad \text{and} \tag{3}$$

$$\frac{\nu_{pz}}{E_p} = \frac{\nu_{zp}}{E_z}, \tag{4}$$

where E_p and ν_p are the Young's modulus and Poisson's ratio, respectively, in the unpolarized x-y symmetry plane, E_z and ν_{zp} are the Young's modulus and Poisson's ratio in the polarized z-direction, and G_{zp} is the shear modulus in the polarized z-direction. In addition to these five material properties, the permittivity matrix $\boldsymbol{\varepsilon_T}$ and the piezoelectric strain matrix **d** characteristic of PZT-8 are needed to model the piezoelectric transducer. All necessary piezoelectric material properties are obtained from APC International, Ltd.[35] The properties of PZT-8 used in the ANSYS simulations are found in Table A.1 of Appendix A.

Details of the simulation of the piezoelectric material in ANSYS are given in Appendix B; however, a brief description of the method by which the electrical input

impedance of the piezoelectric transducer is obtained is provided here. The piezoelectric transducer is modeled using 2-D PLANE13 or 3-D SOLID98 coupled-field elements with voltage and displacement in the x- and y- (and z- for SOLID98) directions as degrees of freedom (DOF). These elements carry out field coupling by calculating the appropriate element matrices (using matrix coupling) directly in a single iteration.[36] For a 2-D harmonic response analysis, ANSYS provides voltage and displacement, along with displacement current per unit depth i_{ANSYS} as outputs.[36] The sum of the nodal displacement currents at the top face of the transducer is converted to the true current i_{piezo} flowing through the piezoelectric transducer using the following relation:

$$i_{piezo} = j\omega d_{piezo} i_{ANSYS}, \tag{5}$$

where $j = (-1)^{1/2}$, ω is the angular frequency, and d_{piezo} is the depth of the piezoelectric element. The electrical input impedance is then given by

$$Z = \frac{V}{i_{piezo}}, \tag{6}$$

where V is the voltage applied to the top surface of the piezoelectric transducer.

3.1.3 Modeling the Fluid

It is assumed that within the cavity the mean flow of the ejection fluid is vanishingly small and that the fluid is compressible and inviscid. The momentum and continuity equations can then be simplified to obtain the lossless acoustic pressure wave equation

$$\frac{1}{c^2}\frac{\partial^2 P}{\partial t^2} - \nabla^2 P = 0, \tag{7}$$

where c is the speed of sound in the fluid, P is the acoustic pressure ($P(x, y, (z), t)$), and t is time. Since viscous dissipation is neglected in the derivation of Equation (7), there is no damping of the acoustic waves in the bulk fluid.

If damping is required, ANSYS allows a boundary absorption coefficient, $\beta = r/\rho_o c$, to be specified at the fluid-structure interface.[36] The boundary absorption coefficient is used along with the mean fluid density ρ_o and the speed of sound in the fluid to calculate a characteristic impedance r of the material at the boundary. The characteristic impedance is used in a term that is added to Equation (7) to account for dissipation of energy due to damping. To complete the analysis of the fluid-structure coupling, a fluid pressure load vector is added to the structural equation of the solid at the interface. The fluid is modeled using 2-D FLUID29 or 3-D FLUID30 acoustic fluid elements. For a harmonic response analysis, ANSYS provides the acoustic pressure, the pressure gradient computed using nodal pressure values, and the fluid acoustic particle velocity as outputs.[36] The properties of water, methanol, and kerosene used in the ANSYS simulations are found in Table A.2 of Appendix A.[38-42] Further details of the simulation of the bulk and structural interface fluids in ANSYS are given in Appendix B.

3.1.4 Modeling the Silicon Spacer and Ejector Plate

The spacer and ejector plate are made of silicon, which is treated as a linear, isotropic material. Stress is related to strain by Hooke's law given by

$$\mathbf{T} = \mathbf{c_E} \cdot \mathbf{S}, \tag{8}$$

where as before, $\mathbf{T}$ is the stress, $\mathbf{S}$ is the strain, and $\mathbf{c_E}$ is the elasticity matrix.[43] For an isotropic material, only the Young's modulus E and the major Poisson's ratio ν are

required to completely define the elasticity matrix which is the inverse of the compliance matrix $\mathbf{s_E}$ and vice versa,

$$\mathbf{c_E^{-1}} = \mathbf{s_E} = \frac{1}{E}\begin{vmatrix} 1 & -\nu & -\nu & 0 & 0 & 0 \\ -\nu & 1 & -\nu & 0 & 0 & 0 \\ -\nu & -\nu & 1 & 0 & 0 & 0 \\ 0 & 0 & 0 & 1+\nu & 0 & 0 \\ 0 & 0 & 0 & 0 & 1+\nu & 0 \\ 0 & 0 & 0 & 0 & 0 & 1+\nu \end{vmatrix}. \quad (9)$$

As mentioned above, a fluid pressure load vector is added to the analysis of structural elements located next to fluid elements. The properties for silicon and silicon nitride (Si_3N_4) used in the ANSYS simulations are found in Table A.3 of Appendix A.[33]

2-D 8-node PLANE82 or 3-D SOLID45 structural solid elements are used to model the silicon spacer and ejector plate. PLANE82 elements provide increased accuracy for mixed (quadrilateral-triangular) meshes and are able to handle irregular shapes.[36]

3.1.5 Modeling the Nitride/Tungsten Membrane in the Three-Dimensional Domain

Because the thickness of the nitride/tungsten membrane is small compared to its lateral extent, it is modeled using shell elements in the 3-D simulations. These elements provide a 2-D representation of the 3-D structure. SHELL99 linear layered structural shell elements are used to model the membrane because they are appropriate for membranes comprising multiple layers.

3.1.6 Boundary Conditions

The AC voltage signal driving the piezoelectric transducer is applied to the top surface of the piezoelectric, and the bottom surface is held at 0 V. A zero vertical

displacement boundary condition is applied to the top surface of the silicon ejector plate, and the pressure at the lines (2-D domain) or surfaces (3-D domain) representing the nozzle orifices is set to zero. For the 3-D simulation, a symmetry boundary condition is used on all vertical surfaces external to the simulation domain; therefore, the model represents an ejector with an infinite number of nozzles.

3.2 Model Validation

Validation of the ANSYS simulations is achieved through a comparison of the predicted and measured electrical input impedances of an unloaded (Figures C.1 and C.2 of Appendix C) and water-loaded (Figures 3.3 and 3.4) device. The device used in the measurement of the electrical input impedance comprises a 1 mm thick, 24x28 mm^2 piezoelectric PZT-8 transducer, a 495 μm thick, 24x24 mm^2 silicon ejector plate containing a 20x20 array of nozzles with 5 μm diameter orifices etched in 2 μm thick, 11 μm wide square membranes, and a fluid reservoir bounded by a 630 μm thick, 24 mm wide spacer with a 2 mm wide sidewall. The 2-D domain used to model this device consists of a 1 mm thick, 24 mm wide transducer, a 495 μm thick silicon ejector plate containing an array of 15 nozzles with 5 μm orifices, and a 630 μm thick, 24 mm wide spacer with a 2 mm wide sidewall. The base of the nozzles is 710 μm wide, which yields 11 μm wide, 2 μm thick nitride membranes at the nozzle tips.

Measurements of the electrical input impedance of the device described above were made using a network analyzer (Agilent Technologies, Inc., Model 8753 ES). Although some small discrepancies between the predicted and experimentally-determined resonances are observed (Figures 3.3 and 3.4), the simulations of the acoustic response of

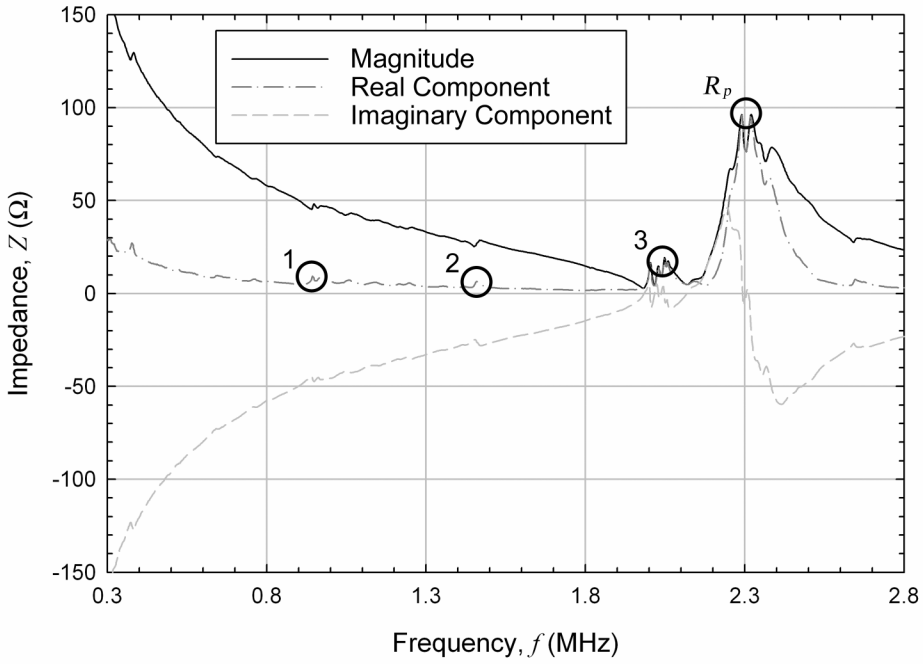

Figure 3.3. Experimentally-determined electrical input impedance as a function of driving transducer frequency for a 1 mm thick lead zirconate titanate (PZT-8) piezoelectric transducer driving a water-loaded device with a 495 μm thick silicon ejector plate and a 630 μm thick spacer.

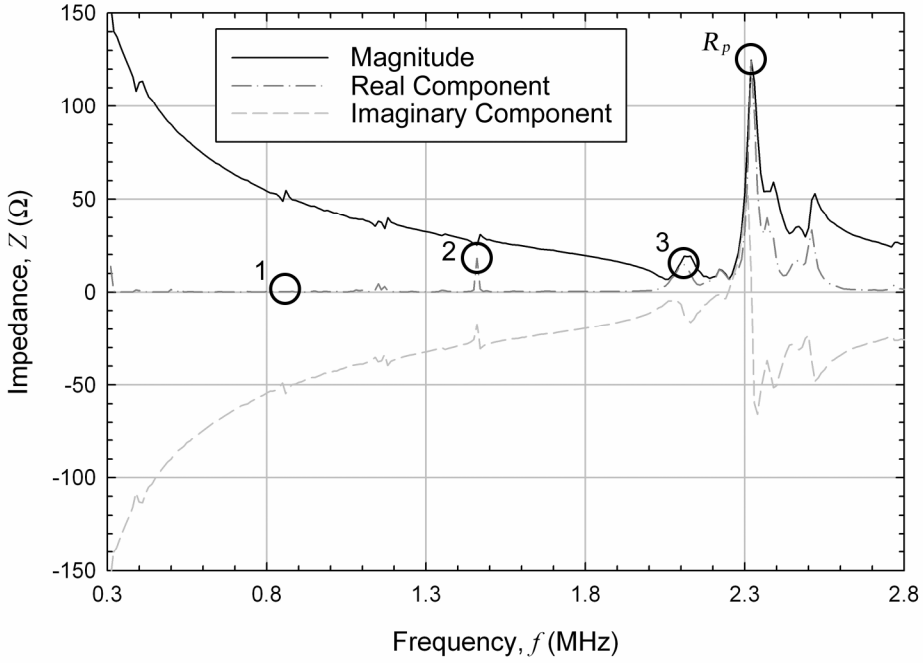

Figure 3.4. Predicted electrical input impedance as a function of driving transducer frequency for a 1 mm thick lead zirconate titanate (PZT-8) piezoelectric transducer driving a water-loaded device with a 495 μm thick silicon ejector plate and a 630 μm thick spacer.

the water-loaded device match measurements remarkably well. The liquid horn resonances are predicted at frequencies of 0.86, 1.46 and 2.10 MHz (labeled 1, 2, and 3). Indeed, successful ejection of water from an array of 5 μm nozzle orifices has been demonstrated over a narrow range of frequencies near 0.90 and 1.45 MHz and over a broader frequency range near the third cavity resonance between 1.95 and 2.10 MHz. In addition, the ANSYS simulations allow one to identify the longitudinal resonance R_p of the piezoelectric transducer at approximately 2.30 MHz. A number of other weaker resonances that partition energy to different vibrational modes are also predicted in Figure 3.4; however, it is not possible to state with certainty that they correspond to particular resonances shown in Figure 3.3 because, unlike operation at resonances corresponding to acoustic wave focusing, no observable change in device operation occurs at these frequencies.

3.3 Baseline Acoustic Response of a Water-Loaded Device

Although successful device operation has been demonstrated for a number of fluids, e.g., water, methanol, kerosene, and water-glycerol mixtures, simulation results obtained using water as the ejection fluid are used to establish a baseline for the acoustic response of the structure over the frequency range 0.3–2.8 MHz. The 2-D computational domain for the model consists of a 1 mm thick, 24 mm wide piezoelectric PZT-8 transducer, a 500 μm thick silicon ejector plate containing 15 nozzles, and a fluid reservoir bounded by a 500 μm thick, 24 mm wide spacer with a 2 mm wide sidewall. The base of the triangular nozzles is 750 μm wide, which corresponds to a 40 μm wide, 2 μm thick nitride membrane with a 5 μm orifice located at the tips of the nozzles. Although this baseline simulation is performed for an ejector with nozzles that terminate

at thin nitride membranes, the form of the nozzle termination (short channel vs. thin membrane) does not noticeably affect the acoustic response of the system as discussed in Appendix D. The amplitude of the AC voltage signal input to the piezoelectric transducer is set at 10 V, and this voltage amplitude along with the output current across the piezoelectric transducer is used to calculate the electrical input impedance of the device. Because of the linear nature of the analysis, the voltage amplitude does not affect the magnitude of the impedance.

Figure 3.5 shows the predicted electrical input impedance as a function of frequency for the water-loaded device. The three highlighted frequencies (1, 2, and 3) represent the first, second, and third resonant modes corresponding to an acoustic wave focusing with a wave located between the top surface of the piezoelectric transducer and the nozzle orifice. Figure 3.6 provides the imaginary components of the complex representations of the pressure fields within the fluid chamber at each of these frequencies. At 0.98 MHz roughly one half-wavelength of an acoustic wave is found between the piezoelectric transducer and the focal point of the nozzles. Similarly, at 1.62 MHz a full wavelength is found, and at 2.40 MHz three half-wavelengths are found.

Note that ANSYS will not output the magnitude of the complex representation of the acoustic pressure field. Only the real or imaginary component can be displayed at each frequency. For most cases, the two components indicate the same form for the pressure field; yet, one will have a much greater magnitude and will therefore provide a better indication of the actual acoustic wave focusing within the fluid chamber. In Figure 3.6 and in subsequent plots of the pressure field within the fluid chamber at resonance,

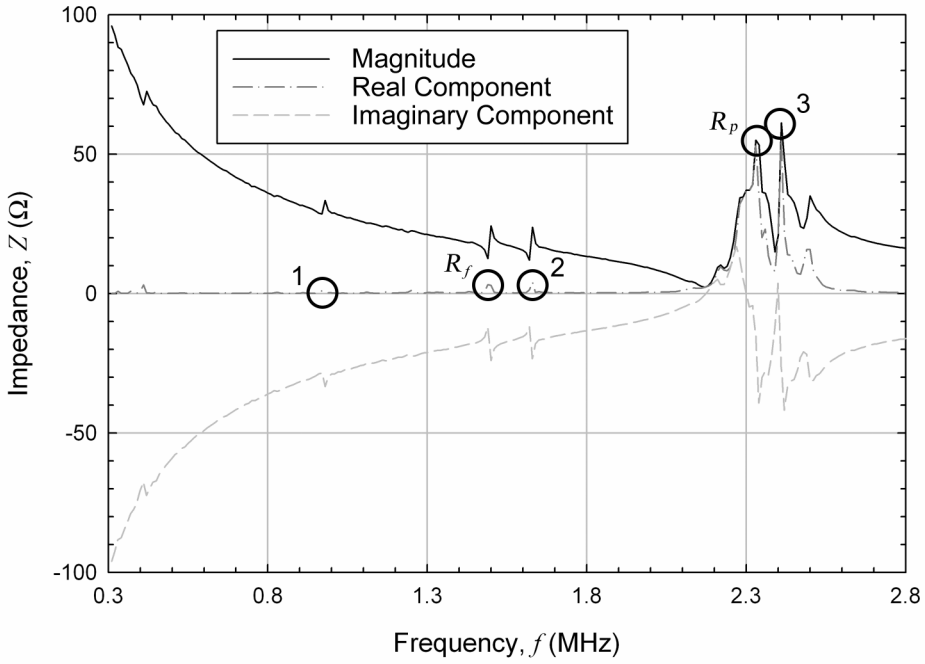

Figure 3.5. Predicted electrical input impedance as a function of driving transducer frequency for a 1 mm thick lead zirconate titanate (PZT-8) piezoelectric transducer driving a water-loaded device with a 500 μm thick silicon ejector plate and a 500 μm thick spacer. The first three resonant modes corresponding to acoustic wave focusing and the longitudinal resonance of the piezoelectric are highlighted.

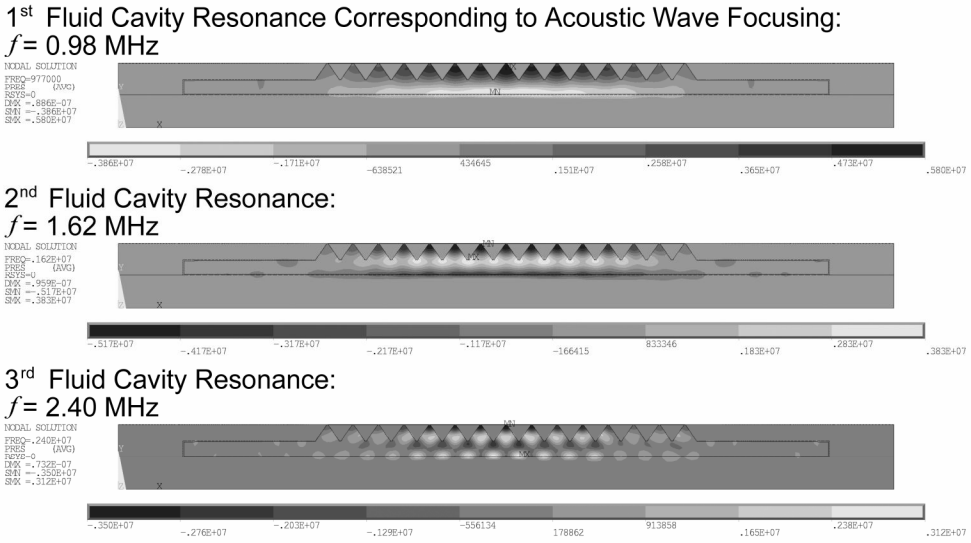

Figure 3.6. Imaginary components of the complex representations of the acoustic pressure fields within the fluid chamber of a water-loaded device driven at the first three resonant modes that result in acoustic wave focusing at the nozzle tips. The device comprises a 1 mm thick lead zirconate titanate (PZT-8) piezoelectric transducer with a 500 μm thick silicon ejector plate and a 500 μm thick spacer. Imaginary components are shown to better illustrate wave focusing.

whichever component of the complex representation of the acoustic pressure field is of the largest magnitude is shown to better illustrate wave focusing.

A number of other resonant frequencies are seen in Figure 3.5. These frequencies correspond to other resonant modes of the ejector assembly and do not lead to focusing at the nozzle tips. For example, the resonance labeled R_f (f = 1.49 MHz) is that corresponding to a standing wave (approximately one half-wavelength) located between the piezoelectric transducer and the flat area of the ejector plate on the periphery of the device (shown in Figure 3.1). The pressure field within the fluid chamber at this resonant frequency is provided in Figure 3.7.

It is interesting to note that efficient ejection is not predicted at the largest resonance labeled R_p in Figure 3.5. This frequency (2.34 MHz) corresponds to the natural longitudinal open-circuit resonance of the piezoelectric transducer and is unrelated to the resonances of the fluid horns within the chamber. At this frequency the pressure field within the fluid chamber is not focused at the nozzle tips for a water-loaded atomizer of the given geometry; however, if desired, it is possible to change the fluid chamber

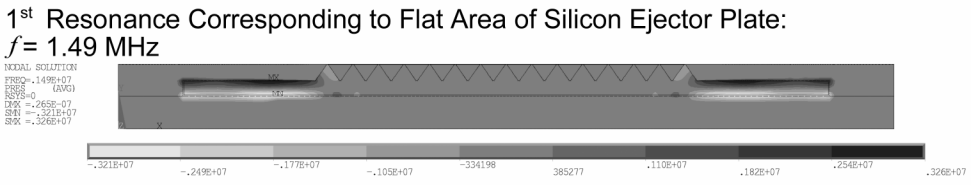

Figure 3.7. Imaginary component of the complex representation of the acoustic pressure field within the fluid chamber of a water-loaded device driven at the first resonance corresponding to a standing wave located between the piezoelectric and the flat area of the ejector plate on the periphery of the device. The device comprises a 1 mm thick lead zirconate titanate (PZT-8) piezoelectric transducer with a 500 μm thick silicon ejector plate and a 500 μm thick spacer. The imaginary component is shown to better illustrate the resonant behavior.

geometry in such a way that one of the cavity resonant modes does match the longitudinal resonant frequency of the piezoelectric transducer.

The fundamental resonant frequency of the fluid cavity is approximately related to its height h_c (shown in Figure 3.1) and the speed of sound c within the ejection fluid as $f_c \approx c/(2h_c)$. In the prototype device, the distance from the piezoelectric transducer to the nozzle tips is constant and approximately equal to 1 mm. Therefore, the resonant frequencies leading to ejection are solely dictated by the speed of sound within the fluid. Using the speed of sound in water (1500 m/s), this simple analysis would predict ejection at 0.75, 1.50, and 2.25 MHz; however, due to the pressure release boundary at the openings of the nozzle tips, the focal point of each nozzle where the acoustic wave pressure maximum occurs is shifted slightly inward from the nozzle tip into the fluid cavity, and the extent of the shift decreases with increasing resonant frequency. This makes the effective fluid cavity height (i.e., the distance from the top surface of the piezoelectric transducer to the focal point of the maximum wave amplitude) less than 1 mm. For example, the focal points for the first and second resonant modes are located at distances of 0.77 mm and 0.93 mm from the piezoelectric transducer, respectively. This behavior is seen in Figure 3.6 as the dark area (focal point) near the tip of the center nozzle moves closer to the nozzle tip as operation moves to higher resonant modes. These observations are essential as they provide simple design rules that can be used to predict the resonant frequencies of the device that are suitable for ejection for any working fluid without performing a detailed ANSYS analysis.

Additional information about the operation of the device can be obtained from Figure 3.6. The pressure field within the fluid chamber is neither uniform nor one-

dimensional at any of the three resonant frequencies. Due to the constructive interference of the acoustic waves within the pyramidal nozzles, those nozzles located closer to the center of the ejector array exhibit better focusing and a higher resulting pressure gradient for fluid ejection. This phenomenon is seen during operation of the device as ejection is observed from only a fraction of the orifices of any given ejector array.

3.4 Comparison of Two-Dimensional and Three-Dimensional Simulation Results

Although simulations performed with the 2-D domain have been shown to accurately predict the resonant frequencies of the actual device (see Section 3.2), it would be difficult to compare the pressure field predicted by the 2-D simulations with that of an actual device during operation. Therefore, a 3-D simulation is performed to confirm that the 2-D simulations accurately predict the acoustic wave focusing within the fluid chamber. Again, the thickness of the silicon ejector plate and the thickness of the spacer are set to 500 μm, and the thickness of the piezoelectric is set to 1 mm. Because the 3-D domain represents one-quarter of a nozzle, the side length of the square piezoelectric element is set to 395 μm, which is half of the distance between adjacent nozzles (790 μm). The nozzle half-width is set to 375 μm, which yields a membrane half-width of 20 μm (corresponding to the membrane width of 40 μm in the 2-D simulation). The radius r_o of the nozzle opening is set to 2.5 μm.

The predicted electrical input impedance as a function of frequency for the water-loaded device shown in Figure 3.8 shows good qualitative agreement with that of the 2-D simulation (Figure 3.5). The four highlighted frequencies (1, 2, 3, and 4) correspond to acoustic wave focusing at the nozzle tips as confirmed by the real components of the complex representations of the acoustic pressure fields shown in Figure 3.9. The first two

resonant frequencies (1.02 and 1.62 MHz) are almost identical to those predicted by the 2-D simulation (0.98 and 1.62 MHz); however, the resonances labeled "3?" and "4?" both appear to correspond to a pressure wave with roughly three half-wavelengths located between the top surface of the piezoelectric transducer and the nozzle orifice. At a driving frequency of 2.27 MHz, three half-wavelengths of an acoustic wave are found between the corners of the top surface of the piezoelectric and the nozzle orifice, and at a frequency of 2.50 MHz, three half-wavelengths of an acoustic wave are found along the centerline of the nozzle between the point at the center of the top surface of the transducer and the orifice. This 3-D behavior is not seen in the 2-D simulations but may

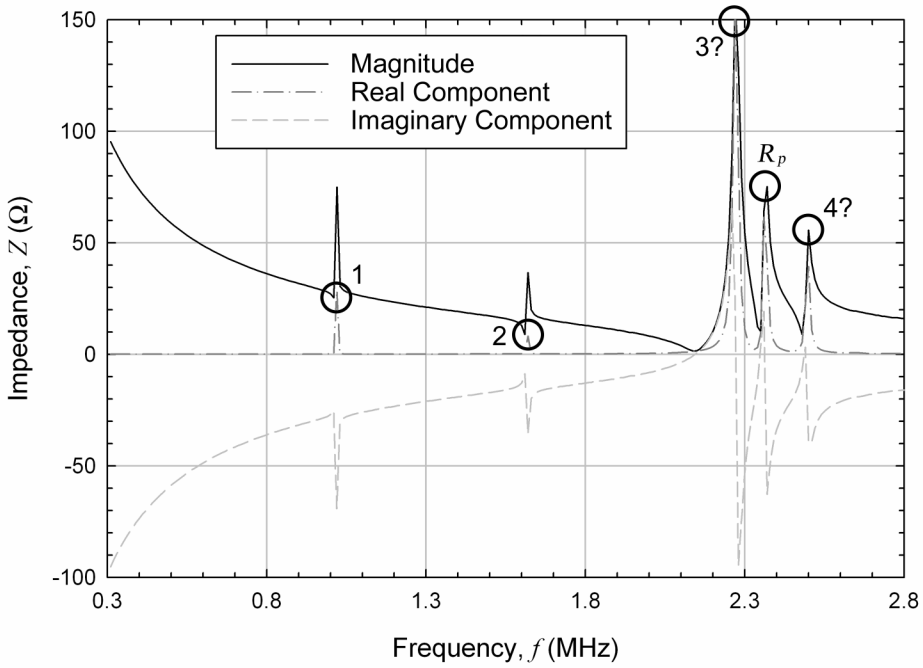

Figure 3.8. Predicted electrical input impedance as a function of driving transducer frequency for the three-dimensional (3-D) simulation domain with a 1 mm thick lead zirconate titanate (PZT-8) piezoelectric transducer driving a water-loaded device with a 500 μm thick silicon ejector plate and a 500 μm thick spacer. The first four resonant modes corresponding to acoustic wave focusing and the longitudinal resonance of the piezoelectric are highlighted.

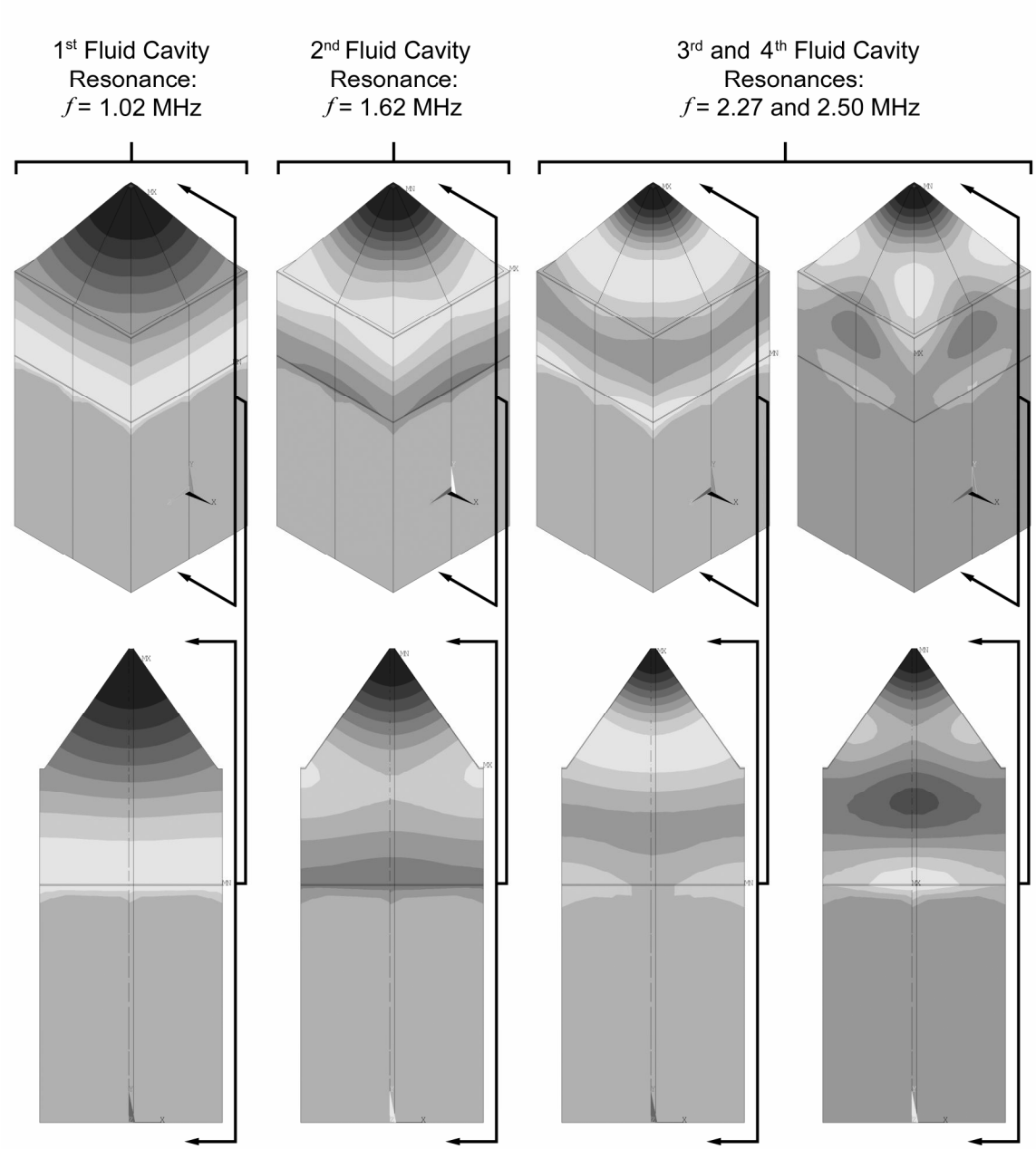

Figure 3.9. Real components of the complex representations of the acoustic pressure fields within a single three-dimensional (3-D) nozzle of a water-loaded device driven at the first four resonant modes that result in acoustic wave focusing at the nozzle tips. The 3-D nozzle comprises a 1 mm thick lead zirconate titanate (PZT-8) piezoelectric transducer with a 500 μm thick silicon ejector plate and a 500 μm thick spacer. Cross sections of the nozzle provide details of acoustic wave focusing along the nozzle centerline. Real components are shown to better illustrate wave focusing.

account for the wider operating range seen near the third resonant mode of operation in the validation experiments. Figure 3.9 also indicates that acoustic wave focusing in the 3-D nozzles is more pronounced than in the 2-D nozzles. As compared with the pressure fields shown in Figure 3.6, the dark area (focal point) near the tips of the nozzles is shifted closer to the orifice for all resonances, and the amplification factor of the acoustic waves due to focusing is between 2.5 and 3.5 times (compared with a maximum of 2 seen in the 2-D simulations). Although 2-D simulations of the acoustic response of the system underpredict the acoustic wave focusing, they better represent other features of actual device operation (e.g., lateral chamber and piezoelectric transducer resonances and the non-uniformity of the pressure field within the fluid chamber); therefore, 2-D simulations are used for the comparative analyses of different device geometries and working fluids.

3.5 Effect of Increasing the Piezoelectric Transducer Thickness

In order to determine the effect that increasing the thickness of the piezoelectric transducer has on the acoustic response of the device, results are obtained for the two-dimensional baseline simulation domain (Figure 3.1) but with the 1 mm thick piezoelectric transducer replaced by a 2 mm thick transducer. Again, water is used as the ejection fluid. Figure 3.10 shows the predicted electrical input impedance as a function of frequency for this device. The two highlighted frequencies (1 and 2) represent the first and second resonant modes corresponding to pressure wave focusing at the nozzle tips as confirmed by the pressure fields within the chamber at these frequencies shown in Figure 3.11. Again, the longitudinal resonance R_p (f = 1.17 MHz) of the piezoelectric transducer and the first resonance R_f (f = 1.52 MHz) corresponding to a standing wave located

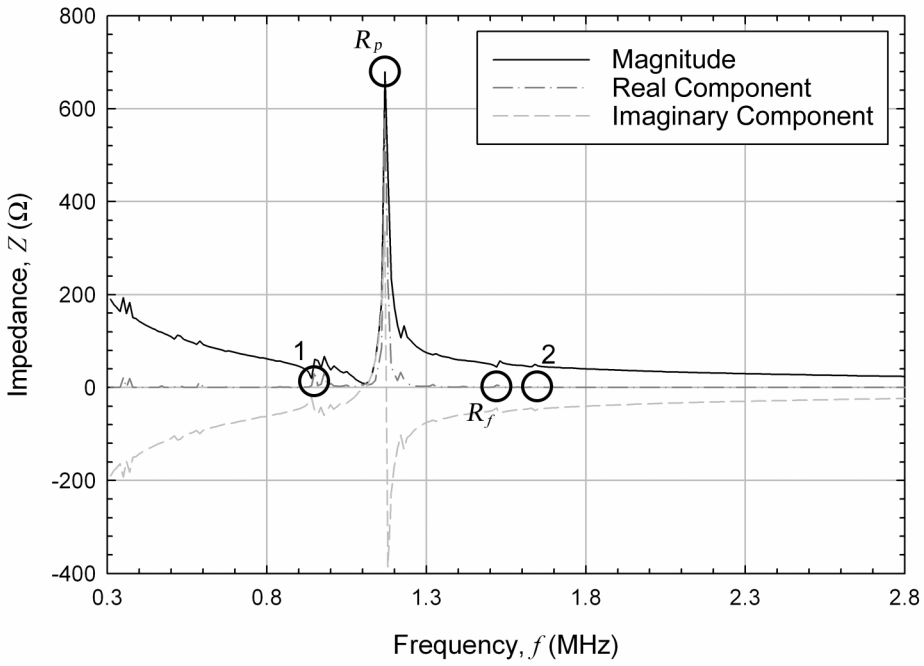

Figure 3.10. Predicted electrical input impedance as a function of driving transducer frequency for a 2 mm thick lead zirconate titanate (PZT-8) piezoelectric transducer driving a water-loaded device with a 500 μm thick silicon ejector plate and a 500 μm thick spacer. The first two resonant modes corresponding to acoustic wave focusing and the longitudinal resonance of the piezoelectric are highlighted.

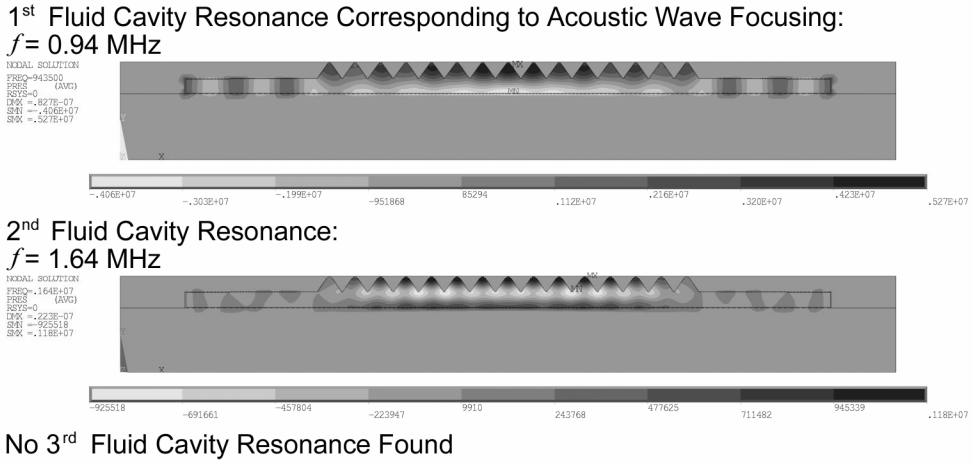

Figure 3.11. Imaginary components of the complex representations of the acoustic pressure fields within the fluid chamber of a water-loaded device driven at the first two resonant modes that result in acoustic wave focusing at the nozzle tips. The device comprises a 2 mm thick lead zirconate titanate (PZT-8) piezoelectric transducer with a 500 μm thick silicon ejector plate and a 500 μm thick spacer. Imaginary components are shown to better illustrate wave focusing.

between the piezoelectric transducer and the flat area on either side of the ejector array are circled in Figure 3.10.

As expected, doubling the thickness of the piezoelectric transducer shifts the longitudinal resonance of the transducer to half of the original frequency, i.e., from 2.34 MHz in Figure 3.5 to 1.17 MHz in Figure 3.10. In turn, the magnitude of the baseline electrical input impedance is doubled. Increasing the thickness of the piezoelectric has little effect on the frequencies at which the fluid cavity resonances occur; however, it is interesting to note that no higher order resonant modes are now seen. This implies that the power transfer from the piezoelectric transducer to the fluid is more efficient at lower frequencies near the fundamental cavity resonant mode. This effect is examined in more detail in Section 3.8.

3.6 Effect of Increasing the Spacer Thickness

Figure 3.12 provides the predicted electrical input impedance as a function of frequency for a water-loaded device using the baseline simulation domain (Figure 3.1) but with a 1.5 mm thick silicon spacer replacing the 500 μm thick spacer. The first six cavity resonant modes found within the frequency range 0.3–2.8 MHz are highlighted (1–6). Cavity resonance is confirmed by the pressure fields within the fluid chamber at these frequencies, which are shown in Figure 3.13.

Because the longitudinal resonance of the piezoelectric transducer is unrelated to the geometry of the cavity, its frequency R_P moves only slightly from 2.34 to 2.38 MHz in Figures 3.5 and 3.12, respectively. The most significant effect of increasing the thickness of the spacer, and thus the height of the chamber, is effectively doubling the

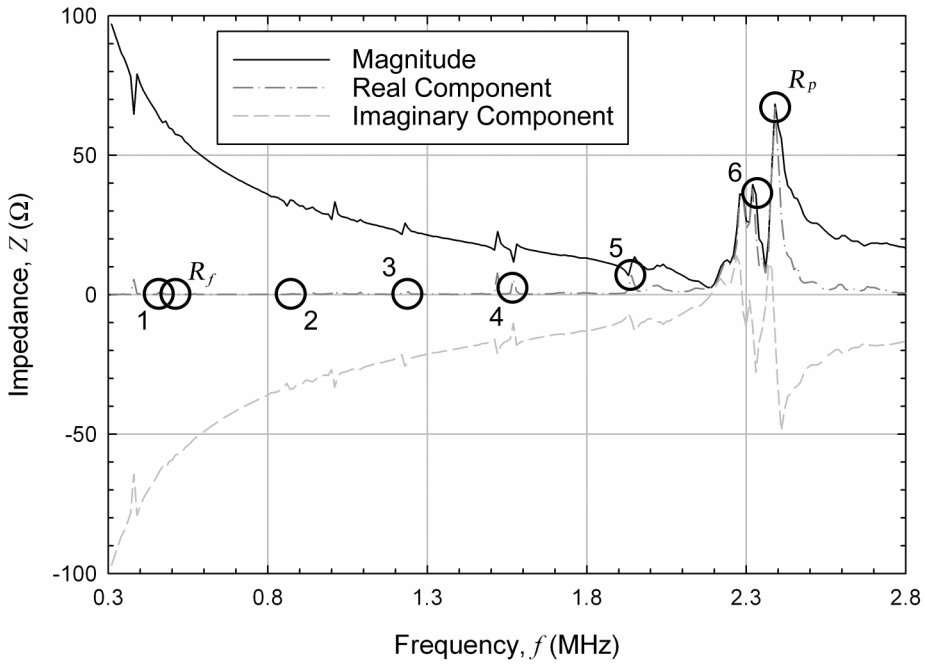

Figure 3.12. Predicted electrical input impedance as a function of driving transducer frequency for a 2 mm thick lead zirconate titanate (PZT-8) piezoelectric transducer driving a water-loaded device with a 500 μm thick silicon ejector plate and a 1.5 mm thick spacer. The first six resonant modes corresponding to acoustic wave focusing and the longitudinal resonance of the piezoelectric are highlighted.

number of possible frequencies of operation in the 0.3–2.8 MHz range for the transducer with the longitudinal resonant frequency of 2.34 MHz. In addition, the frequency envelope is expanded by decreasing the lowest operating frequency from 980 kHz to 470 kHz.

3.7 Acoustic Response of Devices Loaded with Other Fluids

Figures 3.14 and 3.15 show the frequency response of the device loaded with methanol and kerosene, respectively. The properties of the fluids relevant to the ANSYS simulations and compared with those for water are given in Table 3.1. Again a number of different resonant frequencies are observed, the locations of which can be predicted using

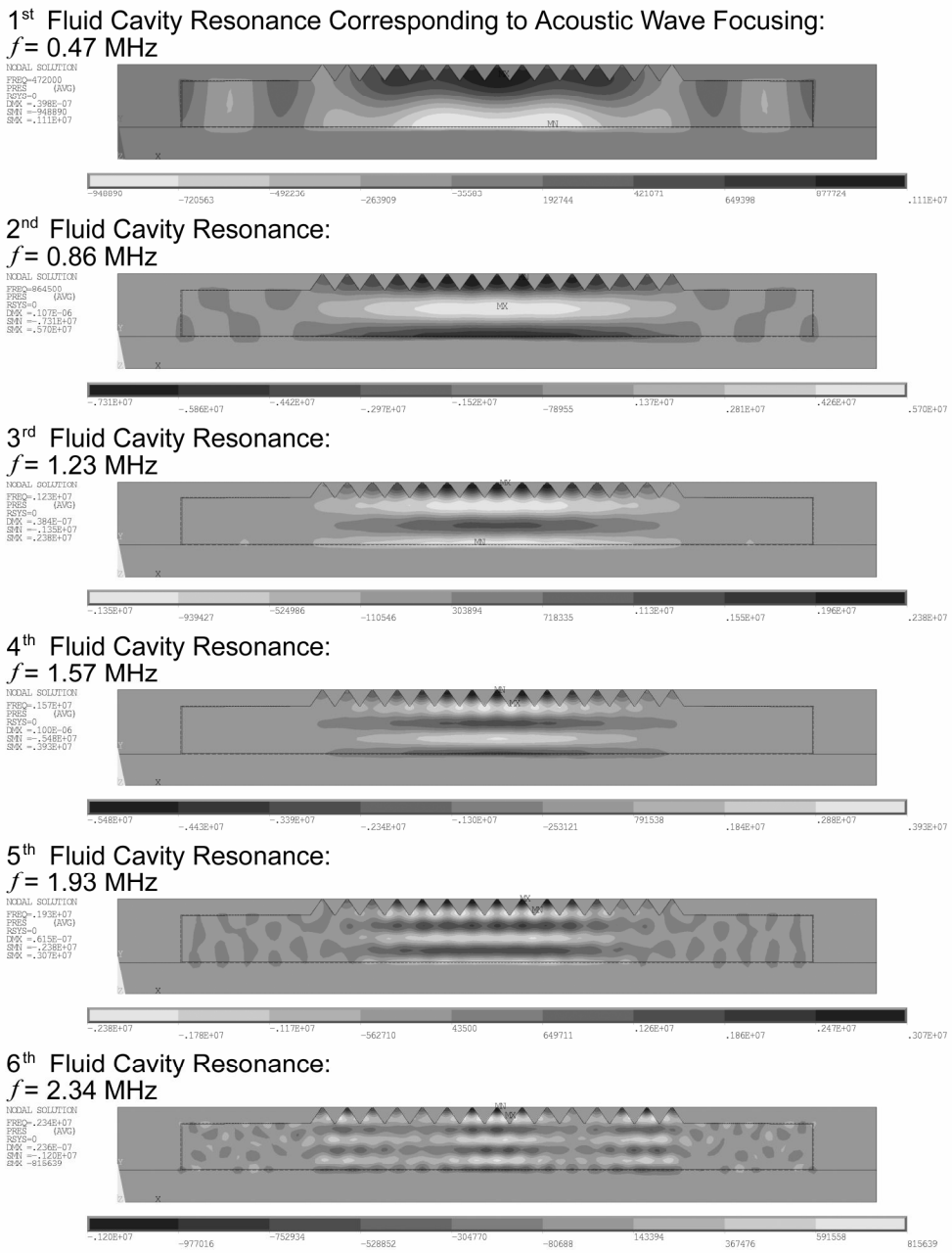

Figure 3.13. Imaginary components of the complex representations of the acoustic pressure fields within the fluid chamber of a water-loaded device driven at the first six resonant modes that result in acoustic wave focusing at the nozzle tips. The device comprises a 1 mm thick lead zirconate titanate (PZT-8) piezoelectric transducer with a 500 μm thick silicon ejector plate and a 1.5 mm thick spacer. Imaginary components are shown to better illustrate wave focusing.

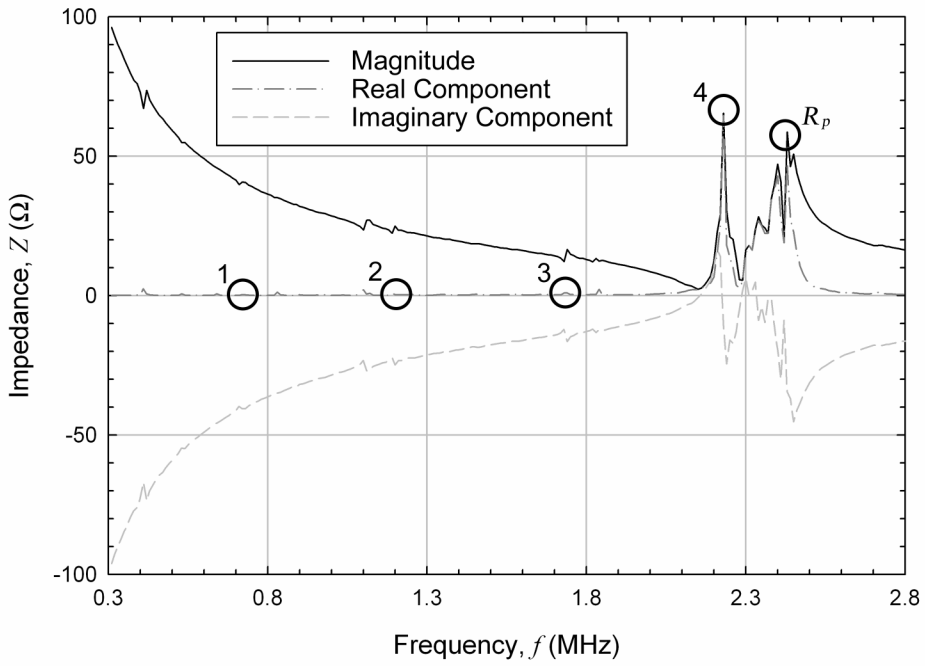

Figure 3.14. Predicted electrical input impedance as a function of driving transducer frequency for a 1 mm thick lead zirconate titanate (PZT-8) piezoelectric transducer driving a methanol-loaded device with a 500 μm thick silicon ejector plate and a 500 μm thick spacer. The first four resonant modes corresponding to acoustic wave focusing are highlighted.

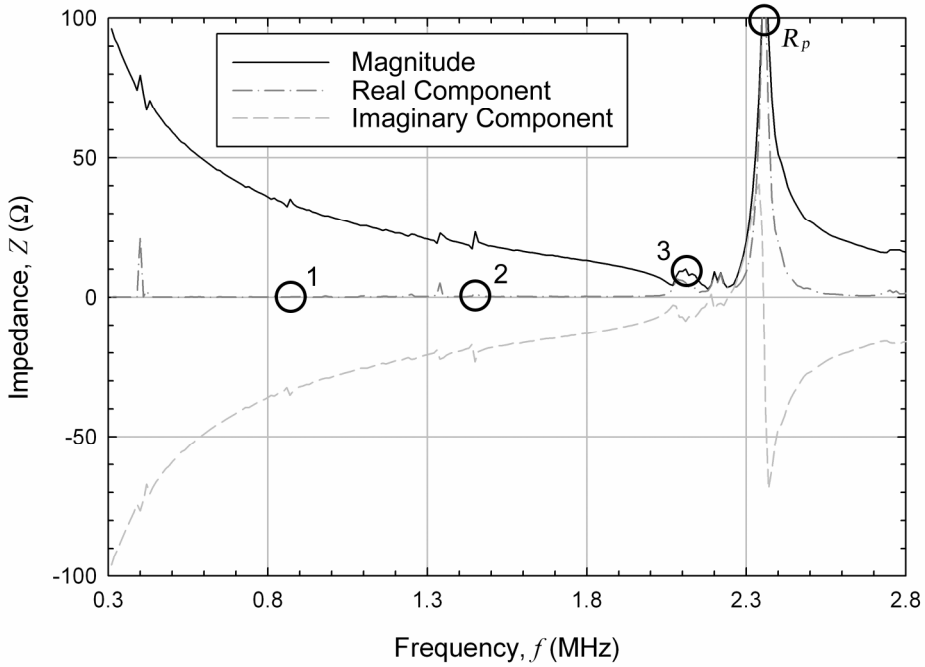

Figure 3.15. Predicted electrical input impedance as a function of driving transducer frequency for a 1 mm thick lead zirconate titanate (PZT-8) piezoelectric transducer driving a kerosene-loaded device with a 500 μm thick silicon ejector plate and a 500 μm thick spacer. The first three resonant modes corresponding to acoustic wave focusing are highlighted.

Table 3.1. Fluid properties used in the ANSYS simulations.

Fluid	Speed of Sound, c (m/s)	Dynamic Viscosity, μ (kg/m-s)	Density, ρ (kg/m^3)
Water	1500	1.00×10^{-3}	1000
Methanol	1089	5.50×10^{-4}	787
Kerosene	1325	2.20×10^{-3}	820

the simple design rule developed by analyzing the frequency response for the water-loaded device (Section 3.3). Based on the earlier discussion, the cavity resonant frequencies suitable for ejection by a given device are defined by the height h_c of the fluid cavity and the magnitude of the speed of sound in each specific fluid considered. In particular, the sound speeds in methanol and kerosene are 1089 and 1325 m/s, respectively, which are less than that in water. Therefore, as compared to the water-loaded device, the cavity resonant frequencies predicted by ANSYS are shifted to 0.72, 1.19, and 1.73 MHz for methanol and to 0.87, 1.45, and 2.10 MHz for kerosene.

Strictly speaking, without looking at ANSYS contour plots of the pressure fields within the fluid reservoir, it is not possible to know for certain that the cavity resonant frequencies listed above for methanol and kerosene correspond to those leading to ejection of water, i.e., represent the same modes as those circled in Figure 3.5. Figure 3.16 provides the imaginary components of the complex representations of the pressure fields within the fluid chamber for the cavity resonant frequency labeled "2" in Figures 3.5, 3.14, and 3.15. This figure indicate that roughly one full wavelength of the acoustic pressure wave is indeed found within the fluid chamber at each of these frequencies

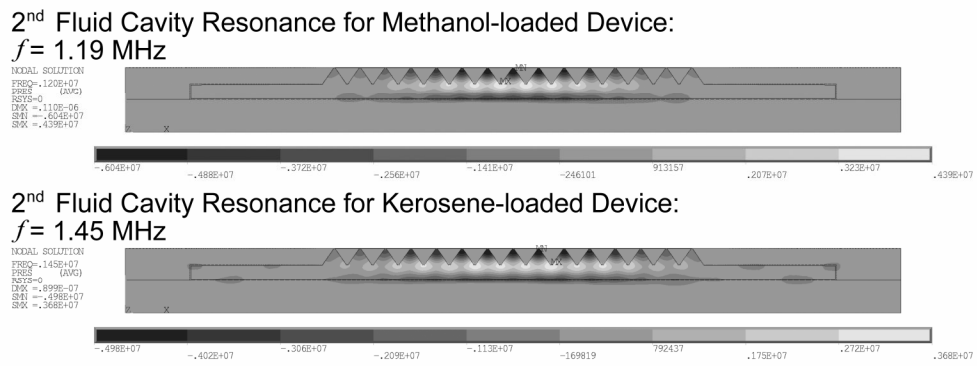

Figure 3.16. Imaginary components of the complex representations of the acoustic pressure fields in methanol- and kerosene-loaded devices at the second resonant mode that leads to acoustic wave focusing at the nozzle tips. The device comprises a 1 mm thick lead zirconate titanate (PZT-8) piezoelectric transducer with a 500 μm thick silicon ejector plate and a 500 μm thick spacer. Imaginary components are shown to better illustrate wave focusing.

that yield wave focusing at the nozzle tip, thus confirming the simple scaling argument presented earlier for estimating the cavity resonances of the device without extensive ANSYS simulations.

3.8 Power Transfer Efficiency Analysis

In addition to predicting the resonant frequencies of the ejector assembly and confirming the acoustic wave focusing within the pyramidal nozzles, ANSYS also permits an estimate of the fraction of the electrical input power to the piezoelectric transducer that is imparted to the ejected fluid. This not only yields the cavity resonance at which a particular device produces the strongest and most efficient ejection but also confirms whether or not it is desirable to make the resonance of the piezoelectric transducer coincide with a cavity resonant frequency.

Since ANSYS is not capable of simulating the actual ejection process, the kinetic energy imparted to a single droplet is estimated from the average acoustic velocity magnitude of all of the fluid elements adjacent to the outlet of each of the nozzles:

$$KE_d = (1/2)\rho_o \forall_d U_d^2, \tag{10}$$

where ρ_o is the fluid density, $\forall_d$ is the droplet volume, and U_d is the estimated droplet velocity. The droplet volume $\forall_d$ is calculated by assuming that the droplet radius r_d is equal to the radius r_o of the orifice.[26,44-46] Assuming that a droplet is ejected from every nozzle during every cycle, the total power imparted to the fluid is expressed as

$$P_F = fNKE_d, \tag{11}$$

where f is the driving frequency of the piezoelectric transducer, and N is the number of nozzles. Note that the actual fluid power is less than that given by the above estimate owing to restraining forces, e.g., viscous dissipation, as well as the fact that ejection does not occur at each nozzle; however, Equation (11) provides a consistent, physically-based measure of the power imparted to the droplets for the comparative study given here.

The electrical input power to the piezoelectric transducer is given by

$$P_E = V \,\mathrm{Re}(i_{piezo}), \tag{12}$$

where V is the applied voltage, and i_{piezo} is the current flowing through the piezoelectric transducer. Device efficiency ε is evaluated as the ratio of the power imparted to the ejected fluid to the electrical input power to the transducer at each frequency of operation.

Again, water is used as the working fluid, and all other simulation parameters are identical to those described previously. The power transfer efficiency analysis is conducted for three different two-dimensional domains: (1) a 1 mm thick piezoelectric transducer with a 0.5 mm thick spacer, (2) a l mm thick transducer with a 1.5 mm thick spacer, and (3) a 2 mm thick transducer with a 0.5 mm spacer. For each simulation, a wide frequency range (0.3–2.8 MHz) harmonic analysis is performed at a step size of 10

kHz to identify the cavity and transducer resonances. Due to the high quality factor of some of the resonances, a higher-resolution (500 Hz step size) simulation centered on each resonance of interest is also performed.

Figure 3.17 provides the electrical input power and the power imparted to the ejected fluid as functions of frequency for the baseline case. Due to the decreasing power input to the transducer, it seems that it is most desirable to operate at the lower frequency modes of the system, and the simple approximation of the ejector efficiency shown in Figure 3.18 strengthens this conclusion. Operation at the longitudinal resonant frequency of the piezoelectric transducer imparts significant power to the ejected fluid; however,

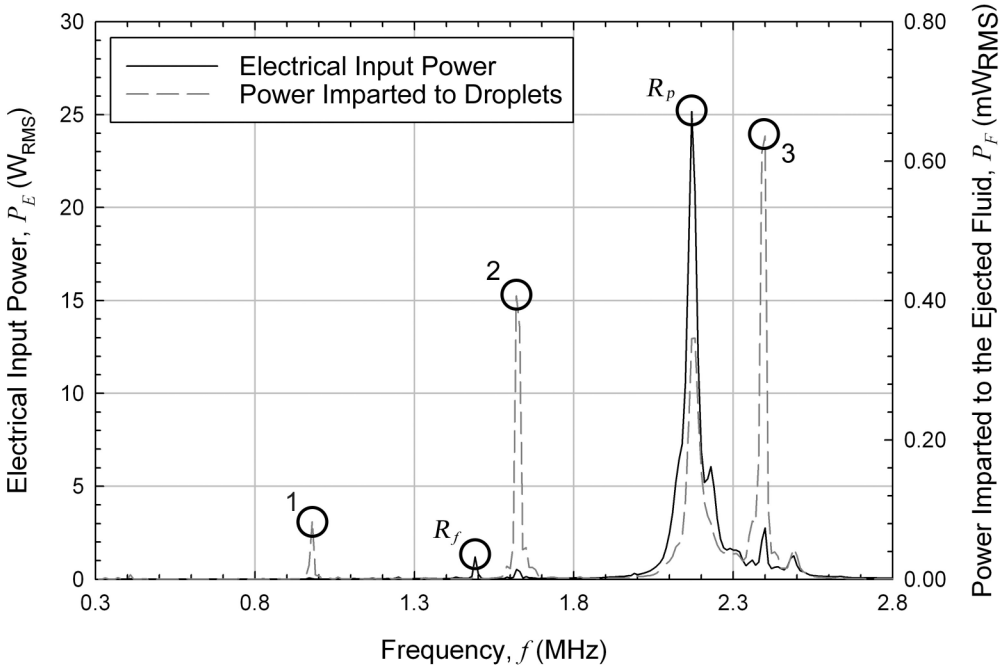

Figure 3.17. Comparison of electrical input power with the power imparted to the ejected fluid as functions of driving transducer frequency for a 1 mm thick lead zirconate titanate (PZT-8) piezoelectric transducer driving a water-loaded device with a 500 μm thick silicon ejector plate and a 500 μm thick spacer. The first three resonant modes corresponding to acoustic wave focusing and the longitudinal resonance of the piezoelectric are highlighted.

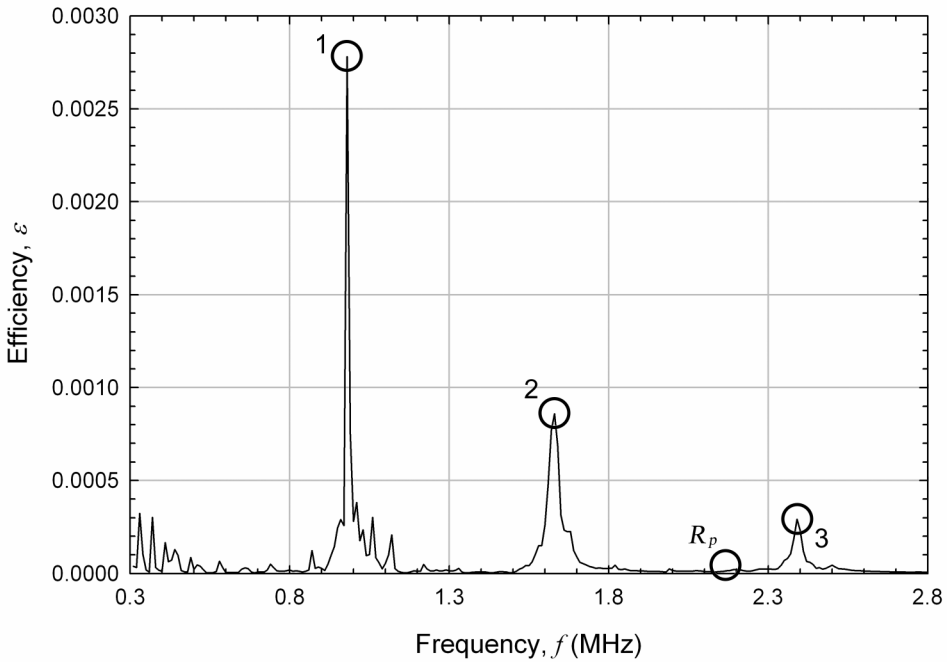

Figure 3.18. Ejector efficiency as a function of driving transducer frequency for a 1 mm thick lead zirconate titanate (PZT-8) piezoelectric transducer driving a water-loaded device with a 500 μm thick silicon ejector plate and a 500 μm thick spacer. The first three resonant modes corresponding to acoustic wave focusing are highlighted.

operation at this frequency is not desirable because amplification of the electrical current and physical displacement of the piezoelectric transducer at resonance leads to drastically increased resistive and frictional losses without the amplification of the fluid velocity associated with operation at a cavity resonance; thus, efficiency drops significantly. This can also lead to excessive device heating, which could be undesirable for applications such as biological fluid processing.

A comparisons of the electrical input power and the power imparted to the ejected droplets as functions of frequency for the case with a 2 mm piezoelectric transducer and the case with a 1.5 mm spacer are shown in Figures E.1 and E.2, respectively, of Appendix E. Plots of the resulting ejector efficiency as a function of frequency are provided in Figures 3.19 and 3.20. Again, the device efficiency at the resonance of the

piezoelectric transducer is low for both cases. Based on Figures 3.18–3.20, it appears that in general the device efficiency while operating at one of the cavity resonances decreases with increasing frequency unless the resonance is located very near that of the piezoelectric transducer (mode 1 in Figure 3.19); however, mode 1 (f = 0.47 MHz) in Figure 3.20 seems to indicate that if the chamber resonance is located far from the longitudinal resonance of the transducer the efficiency enhancement decreases because very little power is imparted to the ejected droplets. The pressure field for this mode shown in Figure 3.13 does not show uniform planar focusing towards the nozzle tips but is somewhat distorted so it is also possible that a lateral chamber resonance located at a frequency near this resonance is causing interference and reducing the focusing effect. It is interesting to note that the efficiency at a given frequency seems to be independent of

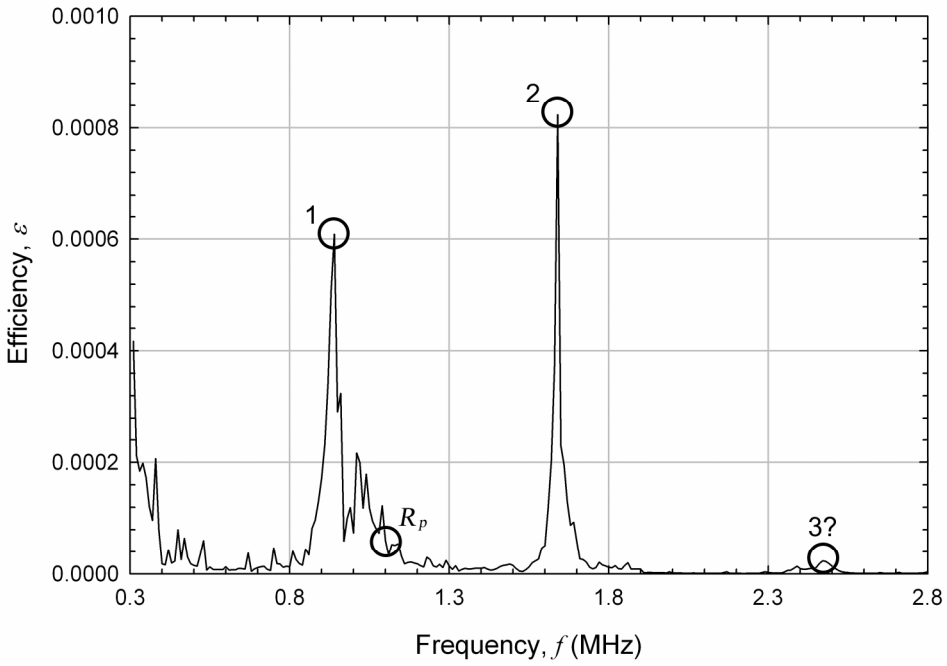

Figure 3.19. Ejector efficiency as a function of driving transducer frequency for a 2 mm thick lead zirconate titanate (PZT-8) piezoelectric transducer driving a water-loaded device with a 500 μm thick silicon ejector plate and a 500 μm thick spacer. The first three resonant modes corresponding to acoustic wave focusing are highlighted.

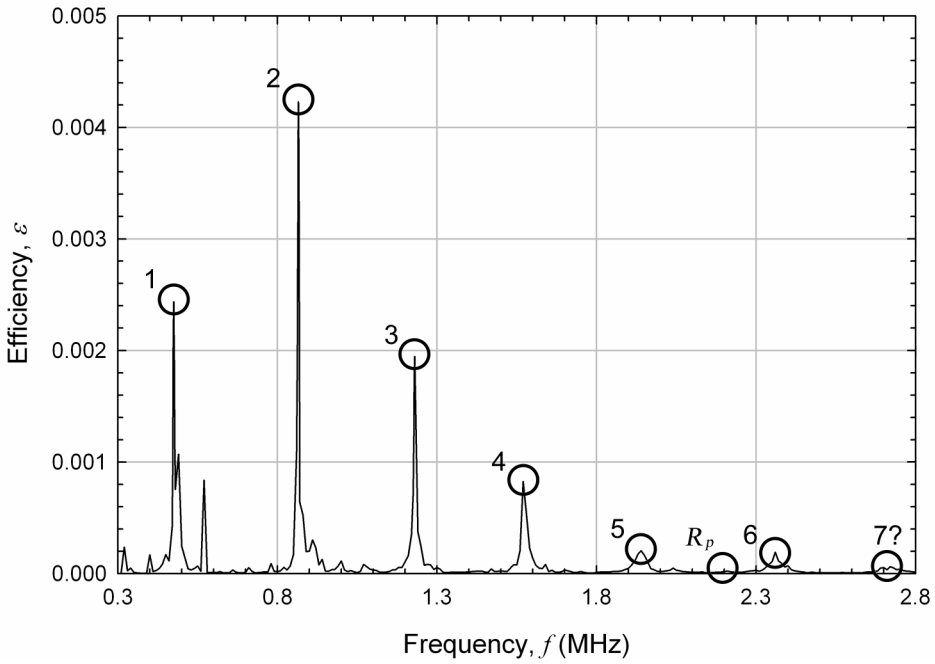

Figure 3.20. Ejector efficiency as a function of driving transducer frequency for a 1 mm thick lead zirconate titanate (PZT-8) piezoelectric transducer driving a water-loaded device with a 500 μm thick silicon ejector plate and a 1.5 mm thick spacer. The first seven resonant modes corresponding to acoustic wave focusing are highlighted.

the cavity resonant mode (e.g., the efficiency of resonant mode 2 in Figures 3.18 and 3.19 at f = ~1.62 MHz with ε = ~0.0008 is approximately the same as that of resonant mode 4 in Figure 3.20 at f = ~1.58 MHz with ε = ~0.0008). The previous discussion of a device driven by the 2 mm piezoelectric transducer suggested that only the first two cavity resonances could be found by looking at the pressure field simulation results. The possible explanation is that the efficiency at higher resonant modes is simply extremely low as shown in Figure 3.19.

Table 3.2 is a summary of results of the ANSYS simulations including resonant frequencies, electrical input power and power imparted to the fluid, and power transfer efficiency for each of the three devices under investigation. Additional insight is gained

Table 3.2. Summary of results of the ANSYS simulations of the acoustic response of the system.

Transducer Thickness, t_{piezo} (mm)	Spacer Thickness, t_{spacer} (mm)	Transducer ½-wave Resonance, R_p (MHz)	Cavity Resonances		Electrical Power, P_E (W)	Fluid Power, P_F (mW)	Efficiency, ε
			Mode	Frequency, f_c (MHz)			
1.0	0.5	2.17	1	0.98	0.030	0.084	0.0028
			2	1.62	0.528	0.406	0.0008
			3	2.40	2.760	0.636	0.0002
2.0	0.5	1.11	1	0.94	0.574	0.350	0.0006
			2	1.64	0.099	0.081	0.0008
			3	N/A	N/A	N/A	N/A
1.0	1.5	2.19	1	0.47	0.176	0.197	0.0011
			2	0.86	2.436	8.739	0.0036
			3	1.23	1.322	1.428	0.0011
			4	1.57	2.364	1.950	0.0008
			5	1.94	3.130	0.637	0.0002
			6	2.36	5.733	1.094	0.0002

through a comparison of the data for each device. For example, a comparison of the results for the 1 mm transducer with a 500 μm spacer and those for the 2 mm transducer with a 500 μm spacer suggests that the piezoelectric resonance should lie significantly above the cavity resonance to be suitable for ejection. As noted above, the efficiency at the second cavity resonance (f_c = ~1.6 MHz) is approximately 0.008 for both cases; however, the electrical input power and the power imparted to the fluid are much lower for the 2 mm transducer, which has a longitudinal resonance at 1.11 MHz, compared to the resonance at 2.17 MHz for the 1 mm transducer. This result emphasizes that the efficiency should not be used as the sole indicator of device performance; consideration must also be given to the magnitude of the power imparted to the fluid. Operation at the

first cavity resonance of the device with the 1 mm piezoelectric transducer and 500 μm spacer is more efficient than operation at the second cavity resonance of the same device so the same ejector performance could be attained with a lower electrical power input; however, a much higher voltage would be necessary, which may not be achievable due to limitations on the power supply.

3.9 Concluding Remarks on the Acoustical Response of the System

In this chapter, experimentally-validated finite element analysis (FEA) simulations of the acoustical response of the system are used to investigate the operating principles of the droplet generator developed in this thesis. Not only do the simulations predict the cavity resonant frequencies, but the acoustic wave focusing within the pyramidal nozzles is also confirmed at each predicted resonance corresponding to a favorable circumstance for fluid ejection, i.e., a large pressure gradient located at the tips of the nozzles.

An estimate of the ejector efficiency at each resonance is obtained by comparing the power imparted to the ejected fluid with the electrical input power to the piezoelectric transducer. Results of this efficiency analysis indicate that, although counterintuitive, it is not optimal to design the ejector such that a cavity resonance coincides with the longitudinal resonance of the piezoelectric transducer; rather, it appears that the efficiency of the device increases with decreasing frequency; therefore, it is desirable to design the ejector so that it operates at its first cavity resonance and with the piezoelectric transducer sufficiently thin so that its longitudinal resonance is much higher than this cavity resonance.

CHAPTER 4

FLUID MECHANICS OF ATOMIZATION: VISUALIZATION AND SCALING

A combination of high-spatial-resolution stroboscopic optical visualization of fluid ejection enabled by the periodic acoustic pumping of liquid horns and a scaling analysis of key phenomena is used to investigate the fluid physics governing the ejection process and to characterize the modes of operation of the micromachined ultrasonic droplet generator.

4.1 Visualization of the Ejection Process

Eggars[47] has presented a thorough discussion of the evolution of experimental techniques employed to observe the development of the flow during droplet formation through the breakup of a continuous jet exiting a nozzle at high speed. In 1686, Mariotte[48] was the first to note that a stream of water flowing from a hole in the bottom of a container decays into droplets; however, a detailed experimental analysis of this phenomenon did not appear until Savart[49] sought to carefully investigate the laws governing it in the early 1800s. The most significant contribution made by Savart was the discovery that periodic disturbances of the jet at the nozzle produced disturbances on the surface of the jet with the same frequency. Plateau[50] performed the first quantitative analysis of the decay of cylindrical jets into droplets while the experimental methodology employed by Savart was improved by Magnus[51,52] and perfected by Lord Rayleigh.[53,54] While investigating the capillary breakup of jets, Rayleigh used an electrically maintained tuning fork to control jet breakup while simultaneously interrupting the

primary current of an induction coil that generated a spark. In this way, the jet was illuminated during a particular phase of transformation and thus appeared almost perfectly steady. Remarkably, Rayleigh was even able to change the observed phase of the jet by pressing slightly upon the reservoir from which the jet issued; however, without photography, there were no methods available to record the shapes of the droplets in any detail.

Lord Rayleigh[55] eventually introduced photographic methods, but quantitative experiments had not been performed until much later. In 1925, Tyler and Richardson[56] examined detailed photographs of the breakup of capillary jets where the interplay between inertia and surface tension leads to the disruption of the jet and the formation of droplets. In addition to analysis of images of this Rayleigh-type breakup, Haenlein[57] and Ohnesorge[58] recorded images of a second type of high velocity jet breakup where the air resistance becomes more important to the breakup of the jet than the surface tension. They also presented pictures of jet atomization.

The techniques that are used to acquire images of droplet formation through the breakup of continuous jets have changed little since these first experiments were conducted; however, the sophistication of the image acquisition system has increased substantially, and improvements in both the source of illumination and imaging devices have enabled the visualization of minute details of the flow with extremely small exposure times. The electric spark that was used as the illumination source by the earliest researchers has been replaced by a pulsed light-emitting diode (LED);[45,47,59] and images that used to be captured on film are now recorded with a charge-couple device (CCD) camera attached to a personal computer and image processor.[47,59]

4.1.2 Experimental Setup

Figure 4.1 provides a schematic overview of the experimental setup that was developed for visualization of the ejection process. The piezoelectric transducer is driven by a sinusoidal AC voltage signal that is generated by the function generator (Stanford Research Systems, Model DS345) labeled "Function Generator 1" in Figure 4.1. The signal is then amplified using an RF amplifier (T&C Power Conversion, Inc., Model AG1020). An oscilloscope (Tektronix, Inc., Model TDS 2014) is used to monitor the

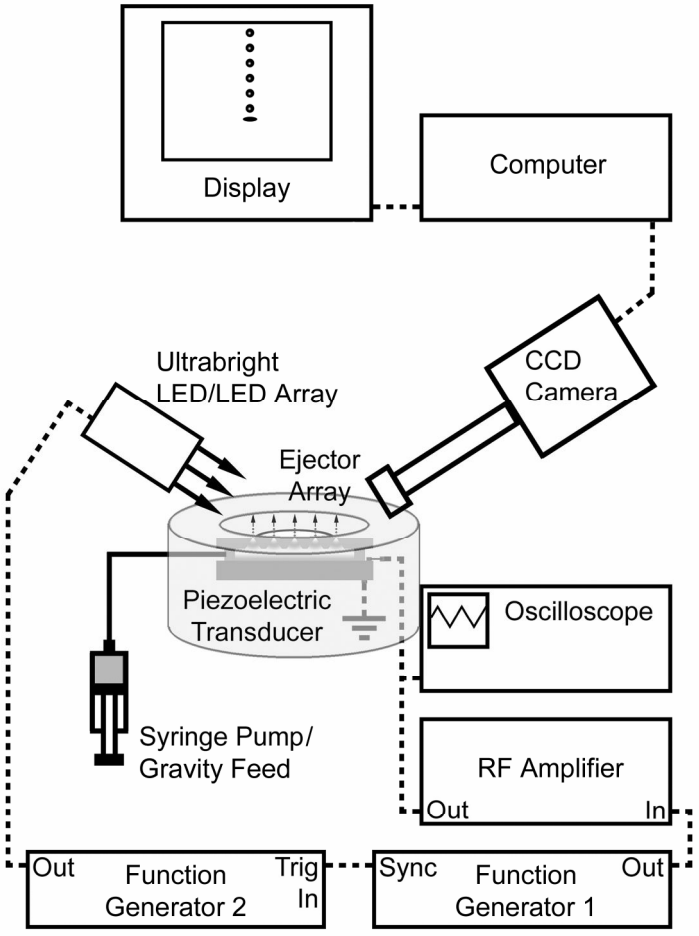

Figure 4.1. Schematic of the experimental setup used for stroboscopic visualization of the ejection process.

voltage signal applied to the piezoelectric transducer. Although the device is capable of self-pumping the ejection fluid through flexing of the piezoelectric transducer, either gravity feed or a syringe pump is used to maintain a steady supply of fluid to the ejector assembly.

The ejection process is periodic due to the periodic (sinusoidal) waveform of the AC signal driving the piezoelectric transducer so visualization is performed using the stroboscopic method. An arbitrary orifice, which exhibits steady ejection, is selected from the ejector nozzle array and is illuminated at the same frequency as that of the piezoelectric drive waveform. This is accomplished using an ultrabright LED array pulsed at a 100–200 ns pulse width using a second function generator (Agilent Technologies, Inc., Model 33250A) labeled "Function Generator 2" in Figure 4.1. This function generator is triggered externally using the sync signal from Function Generator 1 so that the pulse repetition frequency of the LEDs is the same as that of the signal driving the piezoelectric transducer of the ejector. Synchronization of the ejection and illumination frequencies allows one to "freeze" the image in space/time, and each such "frozen" image corresponds to the superposition of thousands of identical ejection events occurring during the time period when the camera shutter remains open (32 ms). Further, in order to observe the evolution of ejection events at various time instants during one ejection period (given by the inverse of the acoustic pumping frequency), a trigger delay of varying duration (such that 10 delay steps are equal to the ejection period) is applied to the waveform driving the LED array. A series of microscope lenses provides adjustable magnification (20–140X) of the image which is then recorded with a CCD camera (Redlake MASD, Inc., Model MegaPlus ES 1.0). The camera output is connected to an

image acquisition module (National Instruments Corporation, Model 1422 Digital IMAQ) for capture and storage of images onto a computer. Automation of the image capture process is achieved using a National Instruments (NI) LabVIEW[60] (version 7.0) virtual instrument (VI) that sweeps through a range of desired driving voltages and illumination delay steps and captures an image at each step. Further details on the experimental apparatus and its assembly are given in Appendix F.

4.1.3 Analysis of Acquired Images

All image acquisition was performed at the same microscope magnification level (60X). An orifice of known diameter (calibration standard) was used to define the scale for measurements taken from the acquired images. An optical microscope image of this orifice is shown in Figure 4.2a. Using a scanning electron microscope (SEM), the diameter of the orifice used as the length calibration standard was measured to be 15.7 μm. NI Vision Assistant[61] software (version 7.0.0) was then used to measure the diameter of this orifice in pixels as shown in Figures 4.2b–4.2d. The clamp function measures the horizontal and vertical distances between the first and last edges found in a rectangular

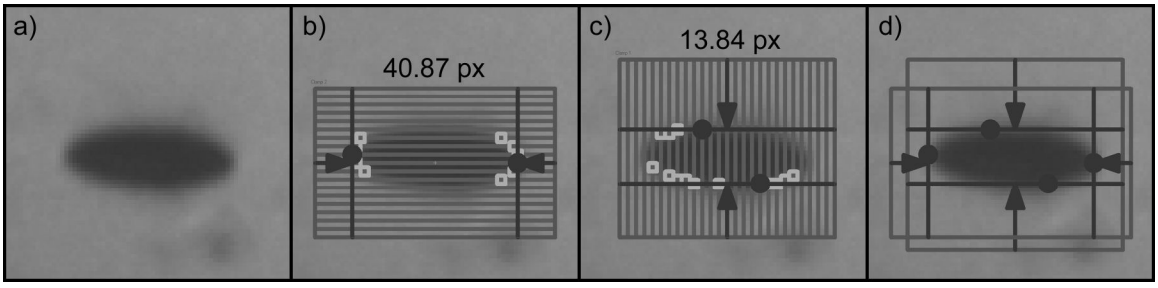

Figure 4.2. Determination of the scale for performing measurements on the acquired images: a) optical image of an orifice of known diameter (measured using a scanning electron microscope (SEM)), b) measurement of the horizontal diameter in pixels, c) measurement of the vertical diameter in pixels, and d) check of edges used for determination of the orifice diameter.

region of interest. As shown in Figures 4.2b and 4.2c, the horizontal distance representing the orifice diameter is 40.87 pixels and the vertical distance is 13.84 pixels. Accounting for the 20° inclination angle of the microscope lens (line of sight) to the ejector surface, the rescaled vertical distance representing the true diameter of the orifice is equal to 40.46 pixels [= 13.84/sin(20°) pixels], which is very close to the horizontal distance (40.87 pixels) as expected for the circular orifice. The ratio of the size of the calibration standard orifice in pixels (40.61 pixels) to its actual size (15.7 μm) yields a conversion factor of 2.6 pixels/μm that is used for reporting all measurements. Note that due to the fuzziness of the images, the uncertainty in the measurements is approximately ±4 pixels or ±1.5 μm.

Measurements of the droplet diameter, the distance between successive droplets, and the wavelength of the jets were also performed using the NI Vision Assistant software. For example, measurement of the horizontal and vertical distances representing the diameter of droplets ejected from a 4.5 μm orifice is shown in Figure 4.3. For this case, the horizontal distance representing the diameter of the droplet in the image is equal to 15.76 pixels or 6.1 μm, and the measured vertical distance is 14.71 pixels. After taking the inclination angle (20°) of the microscope lens into account, the rescaled vertical distance is 15.65 pixels [= 14.71/cos(20°)] or 6.0 μm. Therefore the average diameter of the droplets, which is used in the data analysis, is 6.1 μm.

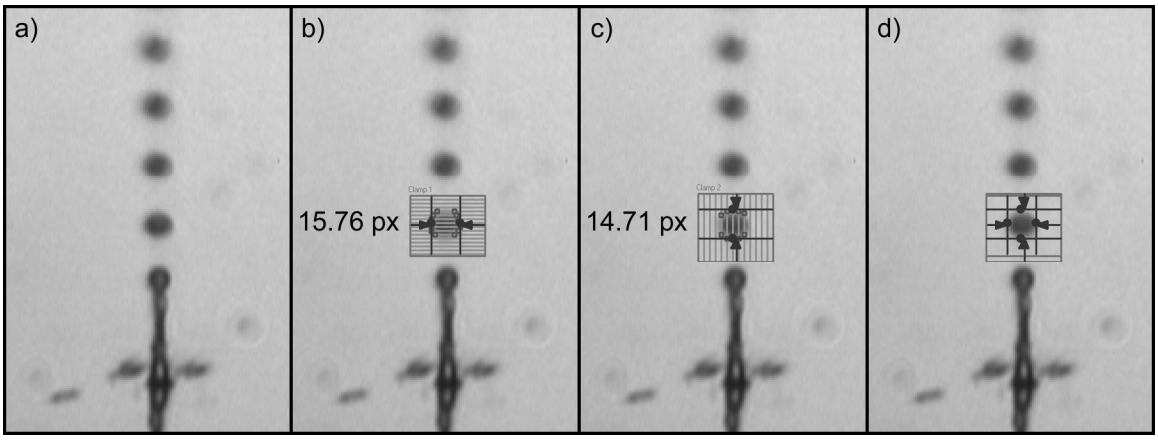

Figure 4.3. Measurement of the droplet diameter: a) acquired image of droplet ejection, b) measurement of the horizontal diameter in pixels, c) measurement of the vertical diameter in pixels, and d) check of edges used for determination of the droplet diameter.

4.1.4 Representative Visualization Results

In all experiments reported here, water was used as the working fluid. Stroboscopic visualization of the ejection process was conducted for two different ejector designs: type 1 which features orifices etched in bulk silicon forming short channels at the tips of the nozzles (Figure 2.11b) and type 2 in which the tips of the nozzles terminate at orifices etched in thin nitride membranes (Figure 2.11a). As has been shown in Chapter 2, the specific type/design of the ejector is dictated by the thickness of the silicon ejector plate as compared to the width of the square base of the pyramidal nozzles.

4.1.4.1 Ejection from Orifices (Microchannels) Etched in Bulk Silicon

Two geometries of the first ejector design (type 1) have been investigated; both ejector plates measured 24x24 mm^2 in footprint and 520 μm thick, and had a 15x15 array of nozzles. Both geometries also had the same length of etched cylindrical channel (~5.0 μm) at the nozzle tips, but with different diameters of 5.9 μm and 11.9 μm. A 600 μm thick Kapton® tape spacer was used to define the fluid chamber, and the ejector was

driven by a 1 mm thick, 24x28 mm^2 piezoelectric PZT-8 transducer. Since the resonant frequencies at which the device operates are only dependant on the fluid chamber geometry (and not on the orifice size in the limit of small orifices) the two ejectors operated at the same frequencies. These resonant frequencies of 0.95, 1.5, and 2.1 MHz were predicted by the ANSYS[36] simulations and verified experimentally by measuring the electrical input impedance of the device using a network analyzer (Agilent Technologies, Inc., Model 8753 ES). Indeed, ejection experiments confirmed that operation of the device at the predicted resonant frequencies led to successful fluid ejection.

Visualization of device operation under various operating conditions (e.g., frequency and amplitude of the driving AC signal) revealed three distinct modes of device operation: (1) no ejection (idling mode), (2) ejection of a stream of individual droplets (discrete-droplet mode), and (3) ejection of a continuous jet which does (transition mode) or does not (jet mode) break into droplets within a short distance away from the ejection point. Reading left to right and top to bottom, Figure 4.4 shows a series of sequential images of ejection of individual droplets from a 5.9 μm orifice at 0.952 MHz. Figures 4.5 and 4.6 show representative images of jet-mode operation that leads to continuous-jet ejection from an 11.9 μm orifice at 0.937 and 1.456 MHz, respectively. Transition (jet-to-droplet) behavior was found to occur when the 5.9 μm ejector was driven at 1.463 MHz as shown in Figure 4.7. In this case, ejection starts in a "continuous-jet" mode; however, the jet quickly degenerates into droplets after traveling approximately two wavelengths away from the orifice. The transition from jet to droplet

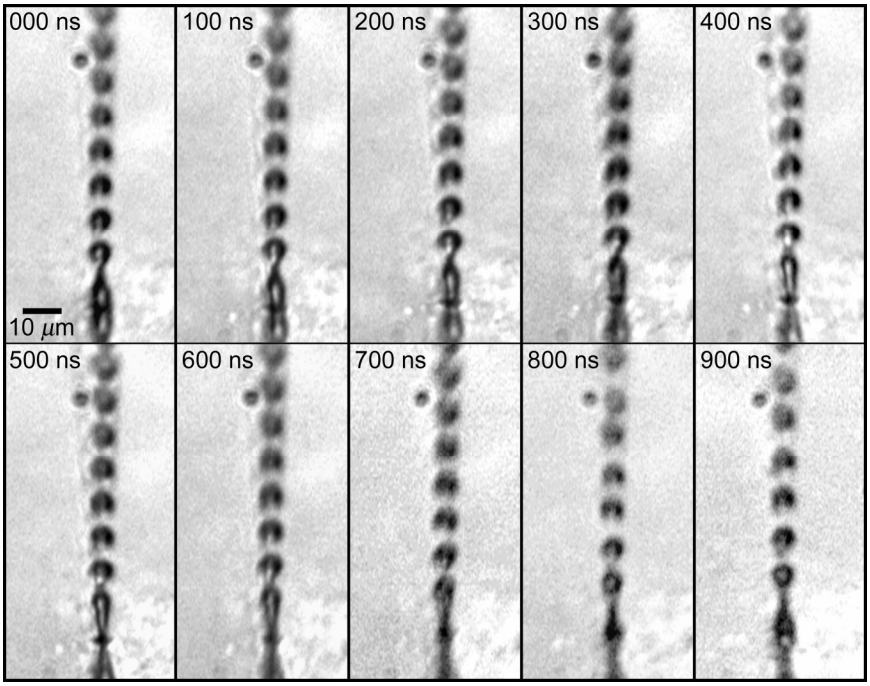

Figure 4.4. Sequential stroboscopic images of droplet ejection from a 5.9 μm orifice of a device with short channels etched in bulk silicon at the nozzle tips and operated at a driving frequency of 0.952 MHz. The delay between successive images is 100 ns.

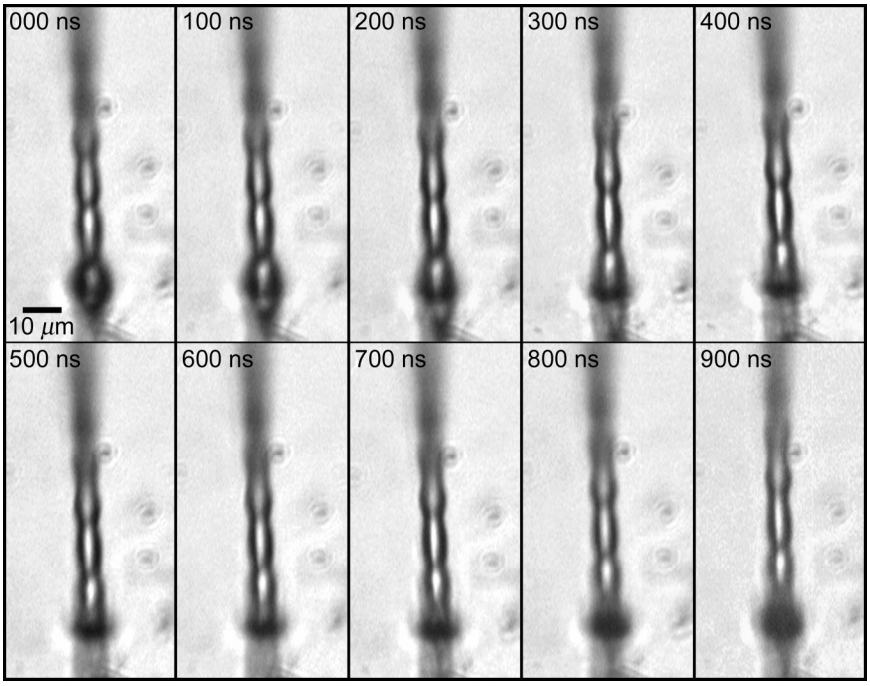

Figure 4.5. Sequential stroboscopic images of continuous-jet ejection from an 11.9 μm orifice of a device with short channels etched in bulk silicon at the nozzle tips and operated at a driving frequency of 0.937 MHz. The delay between successive images is 100 ns.

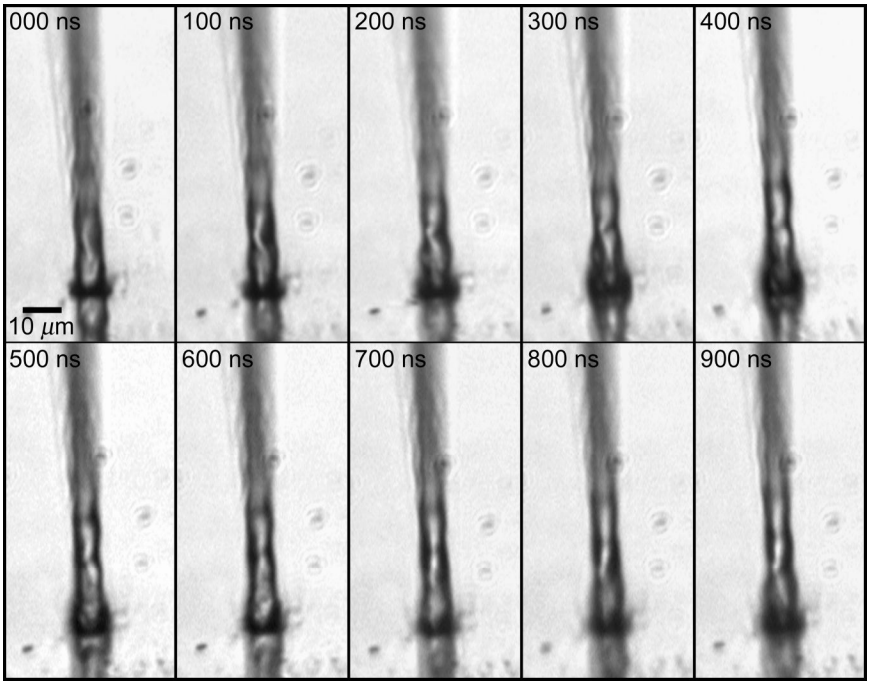

Figure 4.6. Sequential stroboscopic images of continuous-jet ejection from an 11.9 μm orifice of a device with short channels etched in bulk silicon at the nozzle tips and operated at a driving frequency of 1.456 MHz. The delay between successive images is 100 ns.

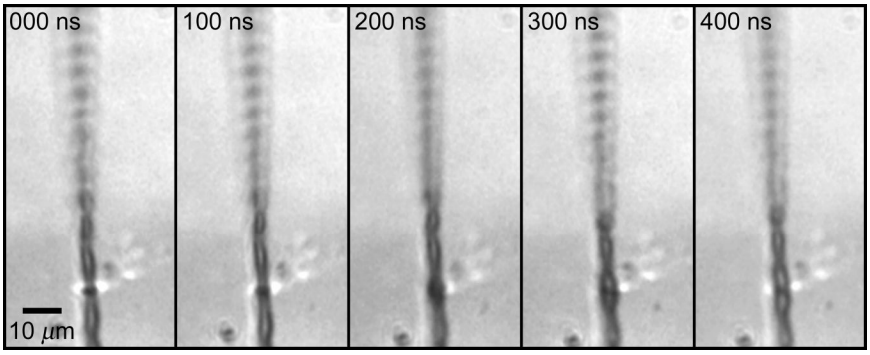

Figure 4.7. Sequential stroboscopic images of the transition from discrete-droplet to continuous-jet mode of ejection from a 5.9 μm orifice of a device with short channels etched in bulk silicon at the nozzle tips and operated at a driving frequency of 1.463 MHz. The delay between successive images is 100 ns.

ejection does not occur at a single driving frequency but over a range of frequencies for an orifice of a given diameter. This phenomenon is discussed in further detail in Section 4.4 of this thesis. In all cases shown in Figures 4.4–4.7, the trigger delay of the pulse waveform driving the LED array is 100 ns between each pair of successive images.

By analyzing the images in Figure 4.4, the diameter of the droplets ejected from the 5.9 μm orifice was found to be 7.2 μm which is slightly larger than the orifice size consistent with observations of ejection from similar devices reported in the literature.[26,44-46] The droplet velocity of 11.8 m/s was determined by measuring the distance traveled by the leading edge of an ejected droplet over the known delay time of the images. The equidistant translation (upward shift) of the "frozen" droplets obtained for progressively longer trigger delays within one period of the acoustic wave oscillation (see Figure 4.4) indicates that a new droplet is ejected at each time period corresponding to the frequency of the AC voltage signal used to drive the piezoelectric transducer. For the case depicted in Figure 4.4, the period of the driving signal was equal to 1.05 μs (f = 0.952 MHz), and the total time delay between the first and last image in the picture is 900 ns. By extrapolation, the stream of droplets at a delay of 1 μs would be essentially identical in shape and position to (i.e., overlapping) the first image of the series, which means that the frequency of ejection (~1 MHz) must be the same as the driving frequency of the device.

The mean diameter and wavelength of the interface wave of the jet ejected from the 11.9 μm orifice at 0.937 MHz (Figure 4.5) were computed from image analysis of the jet to be 6.4 and 17.0 μm, respectively. The interface velocity of 15.9 m/s was determined by tracking the leading edge of the section of the jet just emerging from the orifice in the

first frame over the known delay time between the images. A similar image analysis of the jet ejected at 1.456 MHz (Figure 4.6) indicates that it has a diameter of 8.0 μm, a wavelength of 14.4 μm, and an interface velocity of 21.0 m/s. As was the case for the ejection of droplets, the frequency at which surface waves form at the jet interface is identical to the frequency of the signal driving the piezoelectric transducer.

4.1.4.2 Ejection from Orifices Etched in Thin Nitride Membranes

Two geometries of the second ejector design (type 2) have also been investigated in which the orifices were etched in the center of thin nitride membranes located at the tips of the nozzles. Specifically, a 4.5 μm diameter orifice was etched in an 11 μm wide, 2.5 μm thick nitride/tungsten membrane, and a 15.7 μm diameter orifice was etched in a 26 μm wide, 2.5 μm thick nitride/tungsten membrane. Both ejector plates measured 24x24 mm^2 and featured a 20x20 array of nozzles. A variable thickness (0.63, 1.25, or 1.85 mm) brass spacer was used to define the fluid chamber, and either a 1 or 2 mm thick, 24x28 mm^2 piezoelectric PZT-8 transducer was used to actuate the device. Again, since the resonant frequencies at which the device operates are only dependent on the fluid chamber geometry, the two ejectors operated at the same frequencies; due to the variable thickness of the spacer, ejection was observed at 11 different resonant frequencies corresponding to the first three resonances of the fluid cavity formed by the 1.25 and 1.85 mm thick spacers, and the first four resonances of the fluid cavity formed by the 0.63 mm spacer.

Three distinct modes (idling, discrete-droplet, and continuous-jet) of operation were observed, along with the transition from the continuous-jet to the discrete-droplet mode of ejection. Figure 4.8 shows a series of sequential images of ejection of individual

droplets from a 4.5 μm orifice at 0.785 MHz. Continuous-jet ejection from a 15.7 μm orifice at 0.883 MHz is shown in Figure 4.9, and the sequence of images shown in Figure 4.10 represents the transition from continuous-jet to discrete-droplet ejection from a 15.7 μm orifice at 0.604 MHz.

Image analysis of Figures 4.8 and 4.10 indicates that the diameter of the droplets ejected from the 4.5 μm orifice is 7.0 μm and that of the droplets formed upon breakup of the jet ejected from the 15.7 μm orifice is 11.2 μm. In addition, the undisturbed jet diameter corresponding to the continuous jet shown in Figure 4.9 is estimated to be 5.8 μm.

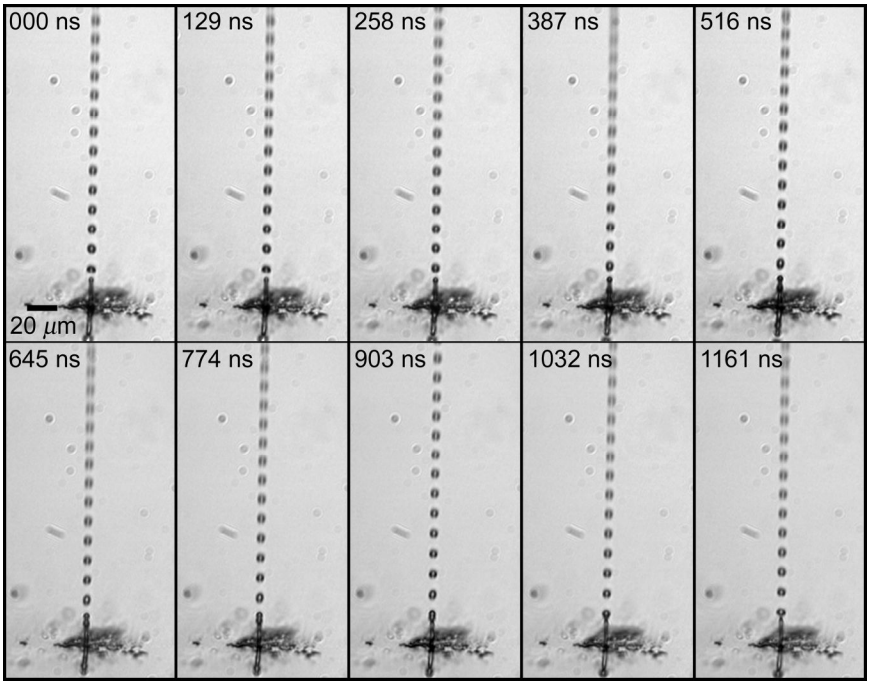

Figure 4.8. Sequential stroboscopic images of droplet ejection from a 4.5 μm orifice of a device with thin nitride membranes at the nozzle tips and operated at a driving frequency of 0.785 MHz. The delay between successive images is 129 ns.

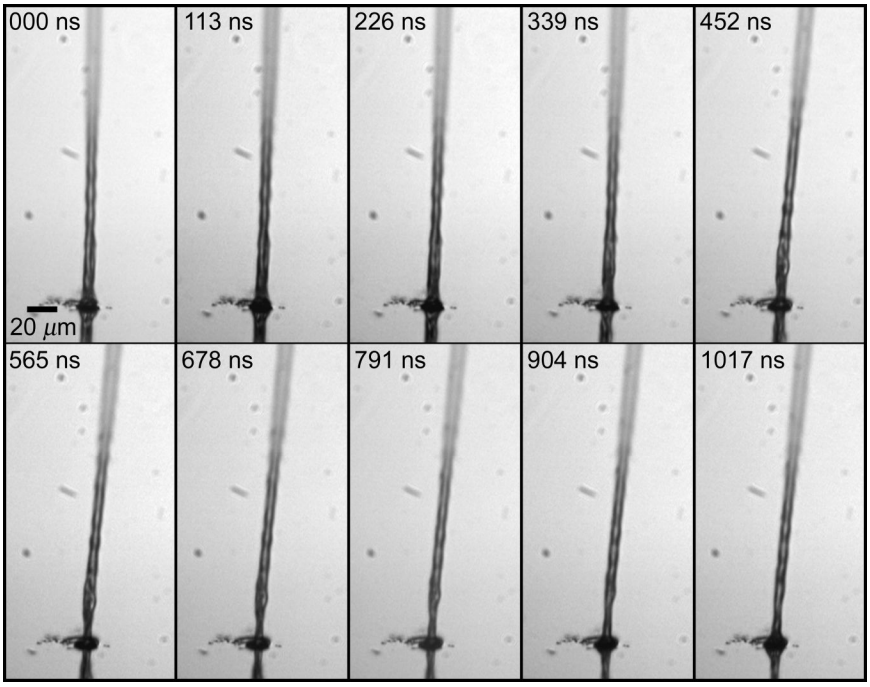

Figure 4.9. Sequential stroboscopic images of continuous-jet ejection from a 15.7 μm orifice of a device with thin nitride membranes at the nozzle tips and operated at a driving frequency of 0.883 MHz. The delay between successive images is 113 ns.

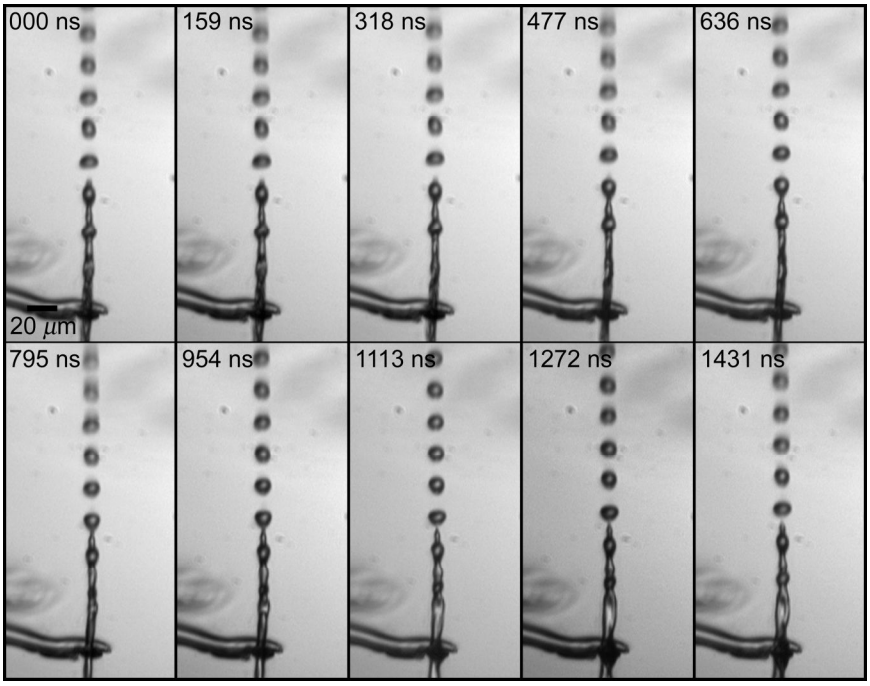

Figure 4.10. Sequential stroboscopic images of the transition from discrete-droplet to continuous-jet mode of ejection from a 15.7 μm orifice of a device with thin nitride membranes at the nozzle tips and operated at a driving frequency of 0.604 MHz. The delay between successive images is 159 ns.

The delay between successive images in Figures 4.8–4.10 is such that a complete period of ejection is shown for each case. Figures 4.8 and 4.10 indicate that a new droplet is ejected at each cycle corresponding to the frequency of the AC voltage signal used to drive the piezoelectric transducer (by extrapolation, if there were another frame in each image sequence, it would be identical to the very first frame). Therefore, the velocity of the droplets (or jet interface) can be determined either by measuring the distance traveled by the leading edge of an ejected droplet (or interface crest) over the delay time of the images or by multiplying the distance between the leading edge of two consecutive droplets (or interface crests) in a single image by the driving frequency of operation. The velocity of the droplets/interface shown in Figures 4.8–4.10 is found to be 10.9 m/s, 14.3 m/s, and 14.0 m/s, respectively.

4.2 Theory of the Ejection Process

The use of periodic acoustic excitation for droplet generation has been studied by several investigators,[4,21,22,24,25,30,62,63] who proposed different, sometimes competing, theories on the fluid mechanics of the process. In particular, it has been suggested that the formation of capillary waves at the liquid-air interface located at the nozzle tips plays a critical role in whether or not ejection is possible, either in discrete-droplet or continuous-jet mode. The wavelength λ of capillary waves on a free surface is prescribed by the Kelvin equation[64]

$$\lambda^3 = \frac{2\pi\sigma_l}{\rho_l f_w^2}, \tag{13}$$

where σ_l and ρ_l are the liquid surface tension and density, respectively, and f_w is the frequency of the capillary waves formed on the free surface of the liquid. Lang[62] applied

this relation to the study of acoustically-driven atomization where the ultrasonic vibration of a liquid surface that is large in extent leads to the rupture of capillary surface waves and the subsequent ejection of droplets from the wave peaks. For ultrasonically generated capillary waves, the driving frequency has been shown to be twice the frequency of the surface waves;[65] therefore, the capillary wavelength is

$$\lambda = \left(\frac{8\pi\sigma_l}{\rho_l f^2} \right)^{1/3}, \tag{14}$$

where, f is the driving ultrasonic frequency. Lang[62] modified Equation (14) to obtain an empirical correlation for the diameter d_d of the resulting droplets:

$$d_d = 0.34 \left(\frac{8\pi\sigma_l}{\rho_l f^2} \right)^{1/3}. \tag{15}$$

Although Equation (15) does not indicate a dependence of the droplet diameter on the liquid phase viscosity or volumetric flow rate, it has been shown to be generally applicable for a variety of fluids.[63] In the spirit of these earlier developments, Perçin *et al.*[4,22,24,25,30] suggested that a relation between the size of an ejector orifice and the wavelength of capillary waves formed by external acoustic pumping must play a role in describing the ejection physics. The criterion governing this balance was presented as a dimensionless surface tension parameter S which is based on Equation (14).

$$S = \frac{2\sigma_l}{\rho_l r_o^3 f^2}, \tag{16}$$

where r_o is the radius of the orifice. Further, Perçin *et al.*[4,22,24,25,30] speculated that when this parameter is less than 1, i.e., the wavelength of the capillary waves is smaller than the size of the orifice, the acoustic energy applied to the liquid-air interface forms small capillary waves that are quickly dissipated by viscous forces, and no ejection takes place.

No reasons have been given as to why small wavelength capillary waves should be more prone to acoustic energy dissipation, as well as why the viscous forces should play a role of any significance in the energy dissipation in the largely static (only acoustically perturbed) fluid. Use of Equation (16) to predict a threshold for ejection of water (σ_l = 72.5x10^{-3} N/m and ρ_l = 1000 kg/m^3) into air yields a limiting (maximum) orifice diameter of 10 μm for driving frequencies ranging from 1–5 MHz; however, in contrast to this prediction, successful ejection of water from an ejector array with 30 μm diameter orifices at driving frequencies up to 2.5 MHz has been achieved with the micromachined atomizer under investigation.

Another possibility is that droplet generation occurs via the breakup of a continuous jet. The phenomena leading to the breakup of a continuous jet of liquid issuing from a nozzle into air have been thoroughly investigated.[48,50-54,56-58,66-68] Depending on the fluid properties (of the liquid jet and the ambient) and the jet velocity, three different types of jet breakup have been observed: (1) varicose breakup due to the capillary instability of the jet,[53,57,58,66,68,69] (2) sinuous breakup due to the resistance of the ambient fluid to the passage of the wave crests on the surface of the jet,[57,58,68,69] and (3) "atomization" where the jet is immediately and violently disrupted to yield a mist of very fine droplets upon exiting the nozzle.[57,58,69]

Linear stability analysis of a long, circular, inviscid, and incompressible liquid jet excited by axisymmetric, spatially harmonic disturbances was performed by Lord Rayleigh[66] who discovered that the wavelength of maximum instability is determined by the interplay between inertia and surface tension. Rayleigh[53,54] confirmed this behavior (varicose breakup) experimentally and found that disturbances are unstable if their

wavelength λ is greater than the circumference, $2\pi r_j$, of the undisturbed jet. In addition, the maximum instability (i.e., the fastest growth rate) occurs for a disturbance having a wavelength of 4.51 times the jet diameter. Smith and Moss[67] found that the continuous length of the jet before breakup by Rayleigh-type capillary instability is proportional to the jet velocity since the most unstable disturbance will grow to break the jet in a fixed amount of time (constant growth rate), and the distance that the jet has traveled during that time is proportional to the jet velocity.

If disturbances arising from the resistance by the ambient environment to the passage of the liquid jet grow at a faster rate than those due to surface tension, the continuous length of the jet before breakup will begin to decrease with increasing velocity.[69] A semi-empirical description of this second type of breakup (varicose breakup) was developed by Weber.[68] Haenlein[57] and Ohnesorge[58] experimentally found that a further increase in the jet velocity leads to a third type of breakup termed "atomization" in which the velocity of the jet is so high that the jet immediately disintegrates (atomizes) into a mist of small droplets upon exiting the orifice. Whether breakup of a continuous jet occurs a short distance from a nozzle or the jet immediately disintegrates, viscous and inertia forces are found to govern breakup at velocities above the critical value where the sinuous disturbance grows at the same rate as the varicose disturbance.[57,58,68,69]

The critical review of the literature calls for a careful investigation of the fundamental fluid physics of the ejection process enabled by the micromachined ultrasonic atomizer. Previously proposed theories of ultrasonically-driven droplet generation from micromachined devices lack sufficient physical justification and fail in

predicting behavior (e.g., threshold of ejection) observed in the ejection experiments. On the other hand, if jet-mode ejection occurs, the classical theories describing continuous jet breakup cannot be used for the acoustically-driven atomization investigated here, as they are only applicable to initially undisturbed, constant velocity jets.[69] In particular, two key questions must be answered: (1) what are the competing physical processes that dictate under what conditions ejection is possible and (2) what controls the mode of ejection, i.e., whether a stream of discrete droplets or a continuous jet of fluid is produced, and if the latter occurs, what causes the jet to break into droplets (transition behavior). The ultimate goal is to develop scaling relationships in terms of relevant physical scales and dimensionless numbers that would allow an *a priori* prediction of the threshold and the mode of ejection, which would lead to rational design and operation of the device for any desired application.

4.2.2 Conceptual Physics of the Ultrasonically-Driven Ejection Process

The micromachined ultrasonic ejector operates in a periodic fashion with the pressure gradient applied near the orifice within the chamber in a pulsating, "push-pull" manner with a frequency equal to that of the waveform driving the piezoelectric transducer. Figure 4.11 illustrates a conceptual representation of the full ejection cycle that one could envision for the discrete-droplet (top) and continuous-jet (bottom) modes. During half of the cycle, the fluid near the nozzle orifice is being pushed out and accelerated by the positive pressure gradient, whereas during the other half of the cycle,

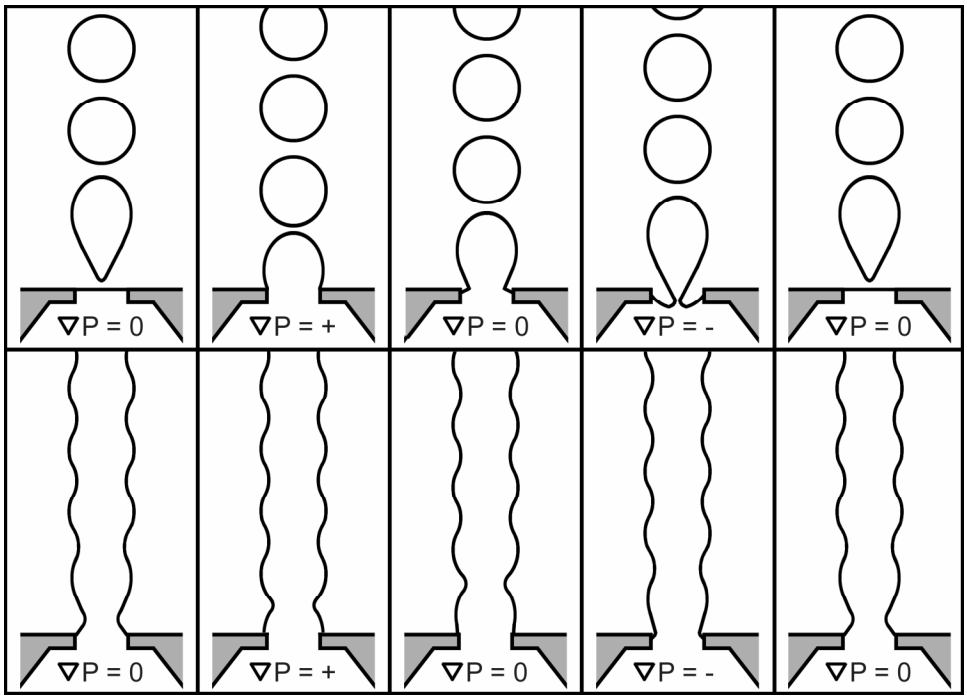

Figure 4.11. Physical interpretation of the ejection process. Discrete-droplet (upper sequence) and continuous-jet (lower sequence) mode ejection processes are illustrated.

the negative pressure gradient acts to slow down or reverse the direction of fluid flow. When the fluid element near the nozzle orifice carries sufficient inertia to overcome surface tension, ejection should occur, and the only effect of the negative pressure gradient during the "pull"-half cycle is to thin the neck upstream of the ejected fluid element near the nozzle orifice. If the neck of the ejected fluid element is sufficiently thin, the surface tension provides a driving force for neck breakup to form a droplet due to the thermodynamically favorable minimum specific surface energy of the droplet; however, this would only occur if the surface tension acts more quickly than the positive pressure gradient, due to the external acoustic pumping, is restored, leading to creation and ejection of an individual droplet as shown in the upper sequence of Figure 4.11. On the other hand, if the positive (pushing) pressure gradient replaces the negative (pulling) pressure gradient acting on the fluid faster than the surface tension can break the

interface, a wavy, but continuous jet should result as shown in the lower sequence of Figure 4.11. In this case, jet breakup and droplet formation may also occur under some conditions, but further away from the nozzle orifice. This conceptual description of the physics of the ejection process provides a theoretical framework for a detailed investigation of the origin and mechanisms of the acoustically driven fluid ejection process via scaling analysis of the basic fluid mechanics phenomena supported by the results of extensive high-spatial-resolution stroboscopic visualization experiments.

4.2.3 Scaling Analysis: Relevant Time Scales and Dimensionless Numbers

Scaling analysis provides a simple and elegant approach to gain basic insight into the physics of many fluid mechanics problems, and the one investigated in this thesis is no exception. When a fluid is slowly released from a large nozzle (e.g., a pendant droplet), the gravitational force must overcome the surface tension force for a droplet to form and detach;[26] however, for systems characterized by an extremely small relevant length scale (i.e., droplet size), the gravitational force is negligible. Another force must drive the ejection process, and for the case under investigation, this is the periodic acoustic pumping. Since the size of the nozzle orifice roughly dictates the size of the ejected droplets in both drop-on-demand (DOD) and continuous-jetting devices,[26,44-46,70] the radius r_o of the orifice is the natural choice of the characteristic dimension for scaling of the ejection process. The frequency of the standing pressure wave within the chamber is identical to that of the voltage waveform used to drive the piezoelectric transducer. The periodicity of the droplet ejection process dictates that the inverse of the driving frequency should be used as the characteristic time scale for the ejection process (hereafter called the process time scale t_f). Since the scaling analysis is an approximate

technique and results are strictly valid for an "on the order of" basis, including numerical factors on the order of 1 (e.g., multiplying or dividing by 2) is beyond the predictive power of this method. In addition to the process time scale, three other time scales can be identified as relevant:

(1) The inertial time scale t_U characterizes the impetus for fluid motion and is defined as the ratio of the characteristic length scale r_o to the velocity U of the fluid prior to ejection.

(2) The capillary time scale t_σ is the time scale at which the surface tension acts at the interface, thereby giving a measure of the time constant that defines the dynamics of the interface deformation. This time scale is a function of the surface tension σ, the characteristic length scale r_o, and the fluid density ρ.

(3) The viscous time scale t_μ characterizes fluid relaxation via viscous forces generated by the fluid motion and is defined as the square of the characteristic length scale r_o divided by the viscous diffusivity μ/ρ.

In summary, the four time scales governing the ejection process are expressed as

$$t_f = \frac{1}{f},\ t_U = \frac{r_o}{U},\ t_\sigma = \sqrt{\frac{\rho r_o^3}{\sigma}},\ \text{and}\ t_\mu = \frac{\rho r_o^2}{\mu}. \tag{17}$$

Following the conceptual framework for understanding the physics of the ejection process put forward in Section 4.2.2, when $t_\sigma < t_f$, the surface tension reacts more quickly than the positive pressure gradient is restored. This results in the disruption of the unstable neck of the wavy jet near the orifice, leading to creation and ejection of an individual droplet (discrete-droplet-mode ejection). On the other hand, when $t_\sigma > t_f$, the positive (pushing) pressure gradient replaces the negative (pulling) gradient acting on the

fluid element before the surface tension can break the interface, and this should result in continuous-jet-mode ejection. In this case, jet breakup and droplet formation will occur on a longer time scale due to surface tension, inertia, or viscous forces. Finally, one would expect that when $t_f \sim t_\sigma$ the transition from droplet- to continuous-jet-mode ejection should occur (indeed this was observed in the representative experiments described in Section 4.1.4), when ejection starts as a jet which quickly (after one or two wavelengths) breaks up into droplets. These scaling arguments, although very simple, have significant implications on the selection of the design and operating conditions for ejectors that produce a desired mode (continuous-jet vs. discrete-droplet) of operation.

The transition from continuous-jet ejection to individual-droplet generation can also be expressed by introducing the dimensionless Weber number, $We = \rho U^2 r_o/\sigma$, and Strouhal number, $St = fr_o/U$, based on the driving frequency, and determining the relationship between these parameters that marks the transition from continuous-jet- to discrete-droplet-mode ejection. From the scaling analysis, the transition is expected to occur when $t_f \sim t_\sigma$, implying that the critical Weber number for transition (We_c) must be of the order of the reciprocal of the square of the Strouhal number, $1/St^2$ (i.e., if $We < We_c$, individual droplet ejection is expected to occur, and $We > We_c$ is expected to yield continuous-jet ejection for any given value of the Strouhal number).

4.3 Validation: Comparison of Scaling Analysis Predictions and Experiments

To support the theoretical development and to validate the predictions of the scaling analysis, a series of careful stroboscopic visualization experiments were performed following the experimental protocol discussed in Sections 4.1.2 and 4.1.3. As described in Section 4.1.4, representative experiments with different devices and under

different test conditions reveal that three possible modes of operation of the ultrasonic droplet ejector can be observed when an AC voltage signal of a certain frequency and amplitude is used to drive the piezoelectric transducer. These include: (1) no ejection (idling mode), (2) continuous-jet ejection which may (unstable-jet/transition mode) or may not (stable-jet mode) lead to breakup of the jet into droplets, and (3) individual discrete-droplet generation. These ejection modes have been found to consistently occur for ejection from devices of different geometries and under varying operating conditions.

The data collected through the visualization experiments enable the time scales relevant to the ejection process to be determined for each test case. Tables 4.1–4.4 provide a summary of these time scales for the cases of water ejection described in

Table 4.1. Summary of operating parameters and time scales for ejection from the 5.9 μm orifice of a device with small channels etched in bulk silicon.

Nozzle Diameter, d_o = 5.9 μm (Radius, r_o = 3.0 μm)							
Mode	Frequency, f (MHz)	Jet/Droplet Radius, r_j (μm)	Jet/Droplet Wavelength, λ_j (μm)	Jet/Droplet Velocity, U_j (m/s)	Process Time Scale, t_f (μs)	Inertial Time Scale, t_U (μs)	Capillary Time Scale, t_σ (μs)
D	0.952	3.6	12.4	11.8	1.05	0.25	0.60
T	1.463	2.1	14.6	21.4	0.68	0.14	0.60
J	2.100	2.5	10.9	22.9	0.48	0.13	0.60

Table 4.2. Summary of operating parameters and time scales for ejection from the 11.9 μm orifice of a device with small channels etched in bulk silicon.

Nozzle Diameter, d_o = 11.9 μm (Radius, r_o = 6.0 μm)							
Mode	Frequency, f (MHz)	Jet/Droplet Radius, r_j (μm)	Jet/Droplet Wavelength, λ_j (μm)	Jet/Droplet Velocity, U_j (m/s)	Process Time Scale, t_f (μs)	Inertial Time Scale, t_U (μs)	Capillary Time Scale, t_σ (μs)
J	0.937	3.2	17.0	15.9	1.07	0.37	1.69
J	1.456	4.0	14.4	21.0	0.69	0.28	1.69

Table 4.3. Summary of operating parameters and time scales for ejection from the 4.5 μm orifice of a device with thin nitride membranes at the nozzle tips.

Nozzle Diameter, d_o = 4.5 μm (Radius, r_o = 2.3 μm)							
Mode	Frequency, f (MHz)	Jet/Droplet Radius, r_j (μm)	Jet/Droplet Wavelength, λ_j (μm)	Jet/Droplet Velocity, U_j (m/s)	Process Time Scale, t_f (μs)	Inertial Time Scale, t_U (μs)	Capillary Time Scale, t_σ (μs)
D	0.444	4.1	19.3	8.6	2.25	0.26	0.40
D	0.605	3.7	23.8	14.4	1.65	0.16	0.40
D	0.785	3.5	13.9	10.9	1.27	0.21	0.40
D	0.885	3.3	16.0	14.2	1.13	0.16	0.40
D	0.978	3.0	12.7	12.4	1.02	0.18	0.40
D	0.994	3.1	11.5	11.4	1.01	0.20	0.40
D	0.990	3.1	16.4	16.2	1.01	0.14	0.40
D	0.983	3.0	16.4	16.1	1.02	0.14	0.40
D	1.044	3.1	22.6	23.6	0.96	0.10	0.40
D	1.126	2.9	20.9	23.6	0.89	0.10	0.40
D	1.410	2.7	18.0	25.4	0.71	0.09	0.40
D	1.475	2.8	11.5	16.9	0.68	0.13	0.40
D	1.475	2.7	15.6	23.0	0.68	0.10	0.40
D	1.992	2.4	12.3	24.5	0.50	0.09	0.40
D	2.521	2.1	11.1	27.9	0.40	0.08	0.40

Sections 4.3.4.1 and 4.3.4.2 along with values for a number of additional experiments. Tables 4.1 and 4.2 contain data resulting from the experiments conducted with type 1 devices featuring 5.9 and 11.9 μm, respectively, orifice channels etched in bulk silicon, and Tables 4.3 and 4.4 contain data for type 2 devices featuring 4.5 and 15.7 μm, respectively, orifices etched in thin (2.5 μm) nitride/tungsten membranes. Note that the viscous time scale has been omitted from Tables 4.1–4.4 because in all cases it is much larger, in most case by one to two orders of magnitude, than the other relevant time scales for all experimental conditions. In addition, although the acoustic field within the static

Table 4.4. Summary of operating parameters and time scales for ejection from the 15.7 μm orifice of a device with thin nitride membranes at the nozzle tips.

Nozzle Diameter, d_o = 15.7 μm (Radius, r_o = 7.9 μm)							
Mode	Frequency, f (MHz)	Jet/Droplet Radius, r_j (μm)	Jet/Droplet Wavelength, λ_j (μm)	Jet/Droplet Velocity, U_j (m/s)	Process Time Scale, t_f (μs)	Inertial Time Scale, t_U (μs)	Capillary Time Scale, t_σ (μs)
T	0.455	3.5/5.8	26.98	12.3	2.20	0.64	2.58
T	0.604	3.3/5.6	23.13	14.0	1.66	0.56	2.58
J	0.604	3.5/NA	21.59	13.0	1.66	0.60	2.58
T	0.604	3.3/5.0	18.50	11.2	1.66	0.70	2.58
J[a]	0.775	3.3/5.8	18.89	14.6	1.29	0.54	2.58
J	0.779	2.9/NA	18.50	14.4	1.28	0.54	2.58
J[b]	0.881	3.1/4.8	19.27	17.0	1.14	0.46	2.58
J[b]	0.883	3.1/4.8	18.50	16.3	1.13	0.48	2.58
J[b]	0.883	2.9/4.8	17.35	15.3	1.13	0.51	2.58
J	0.883	2.9/NA	16.19	14.3	1.13	0.55	2.58
J[b]	0.986	3.1/4.4	14.65	14.4	1.01	0.54	2.58
J[a]	1.057	3.3/4.8	20.43	10.8	0.95	0.73	2.58
J	1.058	3.3/NA	13.49	14.3	0.95	0.55	2.58
J	1.500	2.7/NA	11.56	17.3	0.67	0.45	2.58

[a] Jet breakup occurs approximately six wavelengths from the orifice.

[b] It appears that jet-mode operation would be observed; however, a non-axisymmetric disturbance causes the jet to breakup within 1–10 wavelengths of the orifice.

fluid in the reservoir is generated due to the compressibility of the fluid, compressibility effects are neglected in the fluid dynamics analysis because, even for extremely large fluctuations in the pressure, the properties of the fluid change very little.

Since operation in the idling (no-ejection) mode is difficult to characterize experimentally due to resolution limitations of the visualization optics, only results for discrete-droplet and continuous-jet mode of ejection are reported. The first column of the tables indicates the mode (D, discrete-droplet; J, continuous-jet; T, transition) of operation that was observed in a given experiment. For any ejection (either via jet or discrete-droplet mode) to occur, the inertial time scale t_U must be sufficiently small and

smaller than the process time scale t_f dictated by the frequency of the external force driving the ejection process. If the opposite is true, no ejection will take place. Comparison of the inertial time scale and the process time scale yields the scale for the minimum velocity of the ejected jet/droplets as given by $U = r_0 f$. Thus, for an ejector operating in the 1–5 MHz frequency range, one would expect the minimum ejection velocity for 5 μm diameter droplets to be of the order of 2.5–15 m/s, which is consistent with the measurements reported in Tables 4.1–4.4. In addition, the inertial time scale t_U is the smallest time scale when ejection takes place; however, it is important to note that the calculation of the inertial time scale for continuous-jet-mode operation assumes that the scale for jet velocity is equal to the velocity of the interface motion. This assumption is reasonable since the frequency of the surface waves is equal to the driving frequency.

Tables 4.1–4.4 also elucidate the relationship between the process time scale t_f and the capillary time scale t_σ, which must be satisfied in order to achieve either discrete-droplet or continuous-jet ejection. Indeed, when $t_f > t_\sigma$ (5.93 μm orifice, 0.952 MHz and all 4.5 μm orifice cases) individual droplets are generated; however, when $t_f < t_\sigma$ a transition to continuous-jet-mode generation is observed. This is consistent with the earlier scaling analysis argument that surface tension must react more quickly than the oscillating pressure gradient is reversed (to push the ejected fluid) during each cycle in order for ejection of individual droplets to occur owing to disruption of the neck near the ejection orifice. The opposite is true (i.e., the surface tension is not fast enough in affecting the interface deformation to lead to its rupture) for jet-mode operation. For the case shown in Figure 4.7, $t_f \sim t_\sigma$, and the jet quickly breaks up into droplets. This observation strengthens the conclusion that it is the relationship between t_f and t_σ that

delineates the transition from continuous-jet ejection to individual discrete-droplet generation; however, as was mentioned earlier, the transition from jet to droplet ejection does not take place at a single frequency for a given orifice diameter. The data provided in Table 4.4 suggest that for ejection from orifices etched into thin membranes this transition occurs over a range of frequencies, and in some cases, transition behavior is observed with a capillary time scale t_σ up to 1.5 times the process time scale t_f. This further demonstrates that the scaling analysis is an approximate technique and implies that transition occurs when t_σ is on the order of t_f and not necessarily equal to t_f. Continuous-jet ejection from orifices etched in thin membranes requires special consideration. As is discussed in subsequent sections of this thesis, the presence of a thin membrane appears to introduce additional disturbances which may prematurely break a continuous-jet into droplets.

As discussed in detail in Section 4.2.3, the scaling analysis suggests that the Weber number (We) and the Strouhal number (St) based on the driving frequency can be used to predict the transition from continuous-jet to discrete-droplet mode of ejection. That is, the critical Weber number (We_c) must be of the order of the reciprocal of the square of the Strouhal number, $O(1/St^2)$, for the transition to occur. It should be borne in mind that this transition criterion is applicable only if (1) it is the interplay between the surface tension and external ultrasonic pumping that defines the physics of ejection (i.e., it terms of time scales when $t_f \sim t_\sigma$), and also (2) the viscous forces are weak and act on much greater time scale (i.e., $t_\mu >> t_f, t_\sigma$).

Figure 4.12 is a regime map defined by the transition $We_c \sim O(1/St^2)$ relationship and populated with all experimental data points given in Tables 4.1–4.4. The

experimental results clearly support the predictions of the scaling analysis; that is, all operating points where discrete-droplet generation was experimentally observed do lie in the predicted droplet ejection domain, and all operating points where continuous-jet ejection was found to occur do lie in the theoretically-predicted continuous-jet ejection domain; as expected from the approximate (order-of-magnitude) nature of the scaling analysis, the transition from discrete- droplet to continuous-jet ejection is not instantaneous due to the presence of other factors of minor significance, which are not captured by the scaling analysis which only focuses on comparison of dominant physical mechanisms. Specifically, for the device with 15.7 μm orifices etched in thin membranes

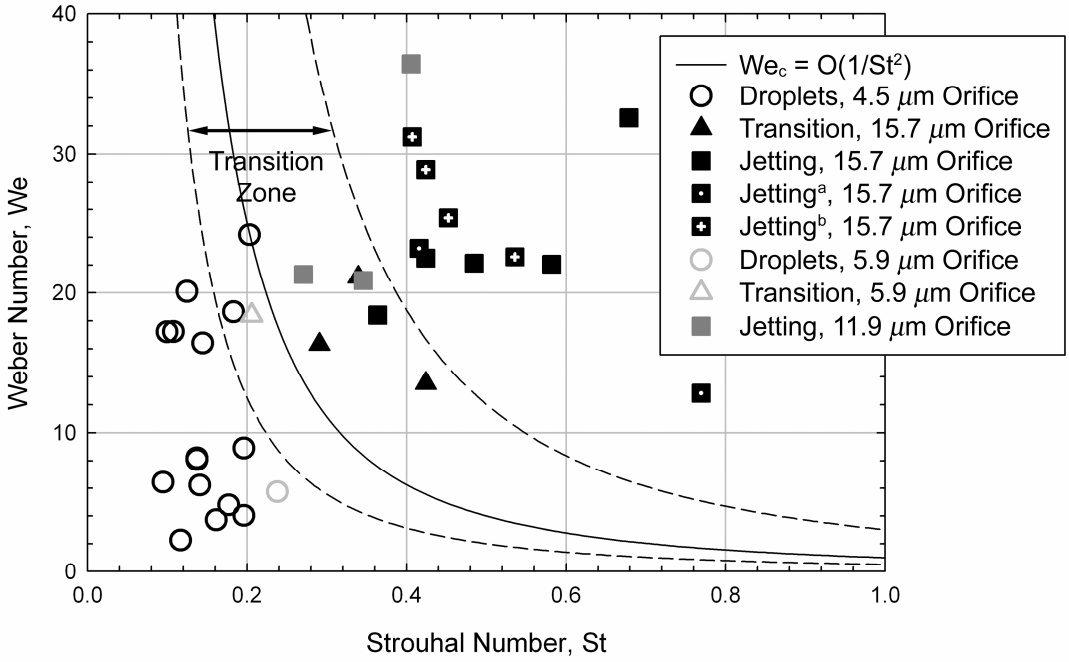

Figure 4.12. Regime map showing the relationship between the critical Weber number We_c defining the transition from continuous-jet operation to droplet generation and the Strouhal number St and a comparison with experimental results. The zone between the dashed lines indicates the region for transition between discrete-droplet and continuous-jet domains.

[a] Jet breakup occurs approximately six wavelengths from the orifice.

[b] It appears that jet-mode operation would be observed; however, a non-axisymmetric disturbance causes the jet to breakup within 1–10 wavelengths of the orifice.

data points representing the experimentally observed transition from discrete-droplet to continuous-jet mode of ejection lie within a narrow band between $We = 1/St^2$ and $We = 3/St^2$, which is well within the fundamental limits of the predictive power of any scaling analysis.

4.4 Additional Observed Ejection Phenomena

The most important and fundamentally new result obtained from the high-spatial-resolution visualization and scaling analysis of device operation under various operating conditions is that both discrete-droplet and continuous-jet ejection are possible, and that there is a predictable transition from one ejection mode to the other; however, a number of other interesting, and often unexpected phenomena have also been observed in experiments, which are summarized here and, in combination with data analysis, yield additional insight into the fascinating physics of ultrasonically-driven fluid ejection from micromachined liquid horns.

4.4.1 Variation of Droplet Diameter with Driving Frequency

Experiments performed at different resonant frequencies revealed that the diameter of the ejected droplets decreases with increasing frequency. For example, Figure 4.13 shows that as the driving frequency increases from 0.444 to 2.521 MHz, the diameter of the droplets generated by a device with 4.5 μm orifices etched in thin membranes decreases significantly from 8.3 μm (Figure 4.13a) to 4.2 μm (Figure 4.13d). A simple mass balance applied to the fluid element near the tip of the orifice that is converted into a droplet upon ejection readily explains this result. During each ejection

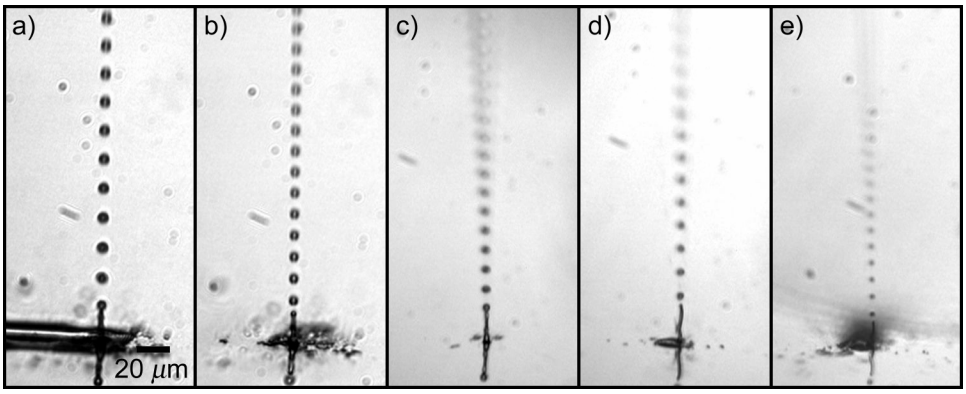

Figure 4.13. Droplet ejection from the 4.5 μm orifice etched in a thin membrane. Droplet generation occurs at driving frequencies of a) 0.444 MHz, b) 0.785 MHz, c) 0.978 MHz, d) 1.475 MHz, and e) 2.521 MHz.

cycle, an "imaginary" cylinder of fluid with diameter equal to that of the orifice (d_o) leaves the nozzle to become a spherical droplet of diameter d_d. The length of the fluid cylinder is represented by the ratio of the fluid velocity U to the frequency f of operation. This periodic-steady-state mass balance for the fluid element can be expressed mathematically as

$$\rho_o \frac{U}{f} \frac{\pi d_o^2}{4} = \rho_o \frac{4}{3} \frac{\pi d_d^3}{8}, \tag{18}$$

where ρ_o is the fluid density. The fluid velocity within the chamber prior to ejection does not depend on the frequency of operation as it is independently controlled by the amplitude of the voltage signal applied to the piezoelectric transducer; therefore, Equation (18) indicates that the droplet diameter scales with the cube root of the inverse of the frequency, $f^{-1/3}$. A log-log plot of the droplet diameter as a function of frequency for ejection from the device with 4.5 μm orifices etched in thin membranes is given in Figure 4.14. A regression analysis performed using statistical analysis software

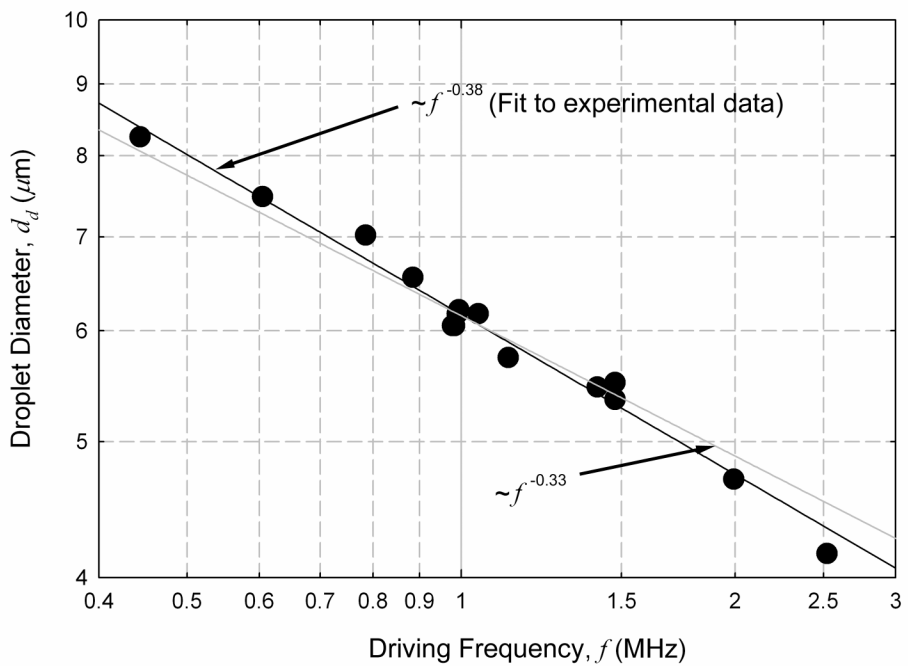

Figure 4.14. Droplet diameter d_d as a function of frequency f for ejection from the 4.5 μm orifice etched in a thin membrane. The experimentally determined relationship $d_d \sim f^{-0.38}$ follows closely the predicted trend ($d_d \sim f^{-0.33}$) obtained via mass balance considerations.

(SigmaPlot,[71] version 7.0) indicates that $d_d \sim f^{-0.38}$ (dark black line in Figure 4.14), which is sufficiently close to the predicted relationship of $d_d \sim f^{-0.33}$ given by Equation (18) (light gray line in Figure 4.14).

4.4.2 Effect of Increasing the Amplitude of the AC Driving Signal

Due to the large number of interacting variables affecting the ejection process from a particular orifice, it is difficult to establish an exact correlation between the amplitude of the AC voltage signal applied to the piezoelectric transducer and the velocity imparted to the fluid ejected from that orifice. However, if the threshold value of the voltage amplitude needed to initiate ejection from a particular nozzle of an ejector array operating at a given frequency is determined, the visualization experiments provide insight into the relationship between the voltage signal amplitude and the velocity of the

ejected fluid. Figures 4.15a–4.15c show the progression of ejected droplets from the 5.9 μm orifice operating at 0.979 MHz as the applied peak-to-peak voltage is increased from a threshold value of 30 V needed to initiate ejection to 36 V. The images of the actual ejected droplets as well as that of their reflections from the silicon ejector surface (shown with an arrow pointer in Figure 4.15) indicate that as the amplitude of the driving voltage signal is increased, the spacing between the droplets and therefore the velocity of the ejected droplets also increases.

Since the acoustic pressure field within the fluid chamber of the array is not laterally uniform as discussed in Section 3.3, the pressure gradient generated at the tip of each nozzle in the array is different. In order to force ejection from a large number of nozzles simultaneously, the piezoelectric transducer must be driven by applying an AC voltage signal beyond the threshold for ejection, and therefore the pressure gradient near the orifice of some nozzles may be much greater than that necessary for ejection. If this is the case, a third type of ejection shown in Figure 4.15d is observed. It is difficult to resolve the detail of the jet shown in Figure 4.15d because ejection is no longer periodic

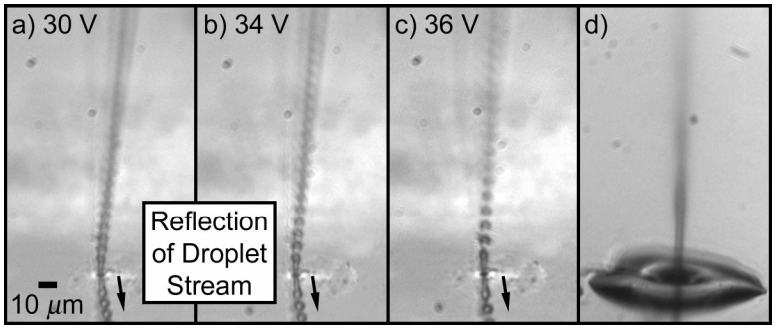

Figure 4.15. Effect of increasing the peak-to-peak amplitude of the AC voltage signal driving the piezoelectric transducer: a)–c) if ejection occurs in discrete-droplet mode, the velocity of the ejected droplets increases with increasing voltage amplitude (d_o = 5.9 μm, f = 0.969 MHz, ejection threshold = 30 V) and d) if ejection occurs in continuous-jet mode, an increase in the voltage amplitude eventually leads to ejection of a jet of fine mist (d_o = 15.7 μm, f = 0.454 MHz).

and in sync with the stroboscopic illumination, but from a close examination it appears to be a mist of extremely small droplets. Thus, it is possible that this mode of ejection represents what was termed "atomization" by Haenlin[57] and Ohnesorge.[58]

4.4.3 Breakup Due to Capillary Instability and Non-Axisymmetric Disturbances

Continuous-jet ejection from the orifices etched into thin membranes exhibited some additional behavioral features not found in the case of ejection from the devices with small channels at the tips of the nozzles, which warrant further discussion. Specifically, a few data points, that are given in Table 4.4 and shown in Figure 4.12 with an identifying superscript symbol "a" in the legend, are for ejection which exhibits breakup of a continuous jet within the field of view of the microscope, but further away from the orifice. It appears that in these cases the jet breakup is caused by the capillary instability of the continuous jet as shown in Figure 4.16. Further, for the cases of jet ejection from a microchannel orifice etched through bulk silicon, the wavelength of the interface wave on the surface of the jet can be easily measured. On the contrary, for the case shown in Figure 4.16 (obtained with a membrane-based device) it is not possible to define a single interface wavelength; yet, the wavelength at which droplets break from the jet appears to remain constant at approximately 30 μm (close-up, Figure 4.16b). The diameter of the jet is estimated to be between 6 and 7 μm, which means that the ratio of the wavelength at which breakup occurs to the diameter of the jet is between 4.3 and 5. For a continuous jet undergoing an axisymmetric disturbance, Rayleigh[53] found that the maximum instability (i.e., the fastest growth rate) occurs for a disturbance having a wavelength of 4.51 times the jet diameter. Thus, it is plausible to suggest that the

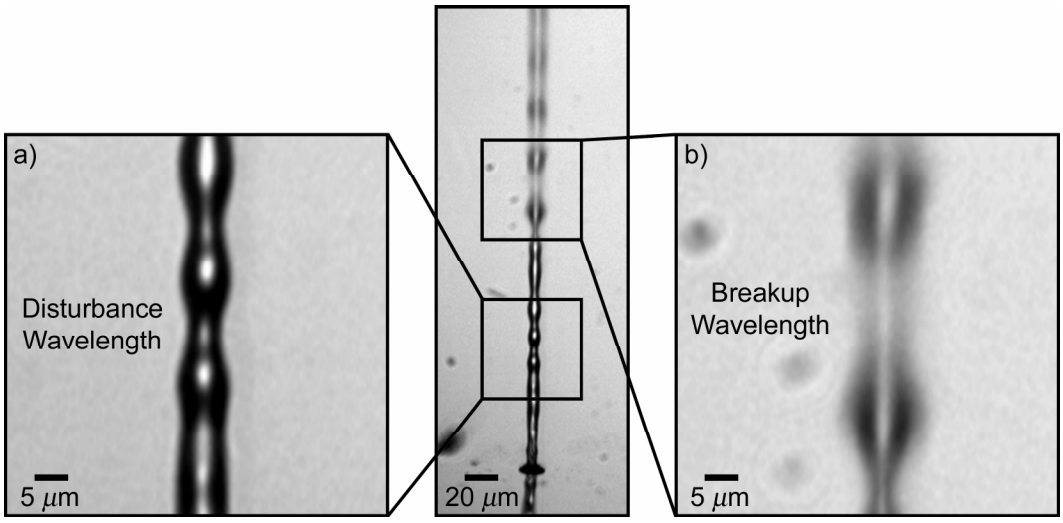

Figure 4.16. Breakup of a continuous jet due to capillary instability at a wavelength of approximately 4.5 times the jet diameter: a) disturbance wavelength and b) breakup wavelength.

continuous jet shown in Figure 4.16 experiences broad band disturbances (e.g., with frequencies ranging from that of the oscillating pressure gradient to those of the membrane resonances), and Rayleigh's "most dangerous" disturbance, which has the wavelength of maximum instability (growth rate), breaks the jet into droplets further downstream.

In addition to disturbances due to the oscillating pressure gradient and possible membrane resonances, the devices featuring orifices etched into thin membranes also exhibit non-axisymmetric disturbances of the interface wave that appear to be caused by either the roughness of the orifice itself or trapped debris. Figure 4.17 illustrates this type of jet disturbance. A sheet of liquid (close-up, Figure 4.17b) periodically forms and sheds small droplets (close-up, Figure 4.17a) from the jet, which breaks up after traveling approximately five wavelengths from the orifice.

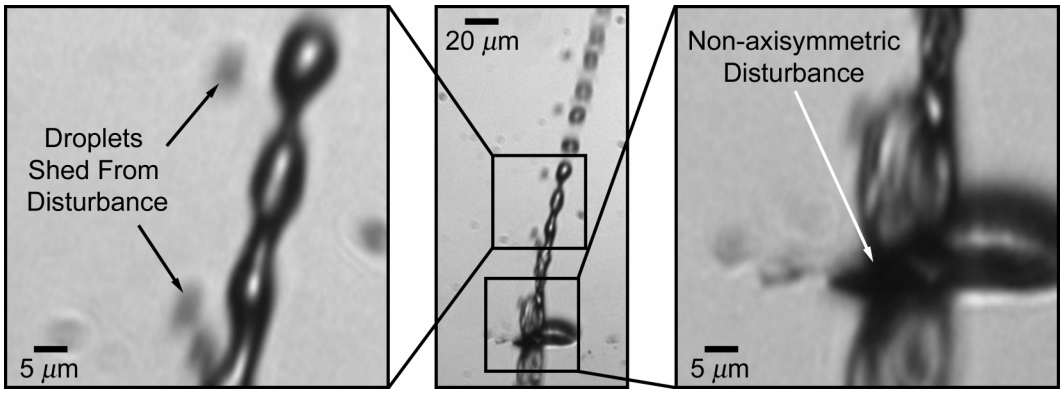

Figure 4.17. Breakup of a continuous-jet due to a non-axisymmetric periodic disturbance.

4.5 Concluding Remarks on the Fluid Mechanics of Atomization

In this chapter, the fundamental physics governing the ultrasonically-driven fluid ejection from an array of micromachined liquid horns has been explored via complimentary experimental and theoretical investigation. In particular, stroboscopic visualization of the periodic ejection of water at MHz-frequencies has been used to reveal the details of the liquid interface evolution during the ejection process with a spatial resolution of down to 1.5 μm. Following the development of a conceptual framework that qualitatively explains the ejection process, an analysis of the relevant time scales has been used to quantitatively explain the observed trends in behavior as well as the measurement data obtained through the visualization experiments. Device operation covering a wide range of experimental conditions has enabled the differences in fluid ejection between micromachined ejector devices with two different orifice designs (membrane-based vs. microchannel-based nozzle termination) to be investigated in detail. Specifically, the effects of orifice diameter (in the range of 4.5–15.7 μm), operating frequency (in the range of 0.44–2.52 MHz), and amplitude of the driving AC voltage signal applied to the transducer (in the range 10–100 V) were quantified with respect to

the threshold for ejection, the mode of ejection, and the ejection velocity. The results have been presented in terms of a regime map using relevant dimensionless numbers. These concerted experimental and theoretical efforts have led to the following specific conclusions:

- Regardless of the specific device design, ejection can be made to consistently occur via two distinctly different modes: (1) by forming a stream of individual droplets (termed "discrete-droplet" mode) or (2) as a continuous jet (termed "continuous-jet" mode). The highly periodic ejection occurs at the same frequency as that of the driving ultrasonic excitation, which either results in formation and ejection of a new droplet at each cycle for operation in the discrete-droplet mode or, in the case of continuous-jet mode of operation, establishment of a constant wavelength periodic wavy interface. The gradual transition from continuous-jet ejection to droplet formation, which is defined by jet breakup very near (within ~1–2 orifice diameters) the nozzle orifice, is induced by changing the balance between the surface tension (capillary) and acoustic pumping (process) effects.
- When the interplay between surface tension and the acoustic pumping does not result in discrete-droplets, two other modes of breakup of the resulting jet have been observed. These are more random in nature, difficult to establish at will, and occur either in the far-field (termed Rayleigh-type due to the observed similarity to the classical Rayleigh-type breakup of jets[53,54,66]) or as a violent explosion of the jet into a mist of small droplets immediately upon ejection (termed "atomization" following the pioneering work of Haenlin[57] and Ohnesorge[58]). The

Rayleigh-type transition has been shown to occur only in the membrane-terminated liquid horns, wherein broad-band disturbances (covering a wide range of frequencies), including the most unstable one leading to eventual jet breakup, are excited on the free surface of the jet.

- The criterion that defines the gradual transition from continuous-jet ejection to individual-droplet generation has been established through comparison of four relevant time scales: the process time scale, $t_f = 1/f$, the inertial time scale, $t_U = r_o/U$, the capillary time scale, $t_\sigma = (\rho r_o^3/\sigma)^{1/2}$, and the viscous time scale, $t_\mu = \rho r_o^2/\mu$. It has been demonstrated that the capillary and the process time scales define the ejection mode for operation in the range of experimental conditions described above with water as the working fluid, i.e. when $t_\sigma < t_f$, ejection of individual droplets results, and $t_\sigma > t_f$ leads to continuous-jet mode of ejection. The transition from continuous-jet to discrete-droplet mode of ejection has been found to occur when $t_f \sim t_\sigma$. Due to the approximate nature of the scaling analysis this transition occurs over a narrow range of operating conditions for which t_σ is "on the order of" t_f and not necessarily equal to t_f. These predictive scaling relationships have been verified experimentally for a wide range of operating conditions, enabling not only clear insight into the basic physics of the ejection process, but also making them practically useful as simple design rules for optimal device operation.
- The gradual transition between ejection modes can also be expressed by introducing the dimensionless Weber number, $We = \rho U^2 r_o/\sigma$, and Strouhal number, $St = fr_o/U$, based on the driving frequency. The transition occurs when t_f

$\sim t_\sigma$ suggesting that the critical Weber number for transition (We_c) must be of the order of the reciprocal of the square of the Strouhal number, $1/St^2$ (i.e., if $We < We_c$, individual droplet ejection is expected to occur, and $We > We_c$ is expected to yield continuous-jet ejection for any given value of the Strouhal number). These predictions have been confirmed experimentally.

- An increase in the ejection frequency has been shown to lead to a decrease in the ejected droplet diameter (for the discrete-droplet mode of ejection) according to the experimentally determined relationship $d_d \sim f^{-0.38}$. It has been shown that such behavior can be explained using simple mass conservation considerations in the limit of a single ejected droplet, which yields a theoretical scaling law ($d_d \sim f^{-0.33}$). This result is in excellent agreement with experiments.
- The threshold for ejection has been shown to occur when the piezoelectric transducer supplies sufficient power to accelerate the fluid near the orifice to achieve a minimum velocity, which is given by the product of the orifice radius and operating frequency, $U = r_o f$. Thus, for an ejector operating in the 1–5 MHz frequency range, one would expect the threshold ejection velocity for representative 5 μm diameter droplets to be of the order of 2.5–25 m/s, which has been confirmed experimentally for a wide range of conditions. An increase in amplitude of the electrical signal driving piezoelectric transducer beyond the critical ejection threshold leads to an increase in the number of active ejectors in the array as well as an increase in the velocity of ejected fluid beyond that given by the threshold relationship; however, this increase is non-linear and may result

in an unpredictable change in the ejection mode, for example, from stable continuous-jet ejection to uncontrollable “atomization”.

Although the scaling analysis has been shown to enable accurate definition of which physical processes dictate under what conditions ejection is possible and what controls the mode of ejection for the entire range of investigated experimental conditions, the results and thus the conclusions presented in this chapter are only valid when the interplay between acoustic pumping and surface tension controls the atomization process. For water as a working fluid, the viscous time scale t_μ is one to two orders of magnitude greater than the time scales for the process (acoustic-pumping frequency) and capillary effects (surface tension) for all experimental cases, which makes the presented analysis physically sound and quantitatively accurate. However, as the radius of the orifice decreases ($t_\mu \sim r_o^2$) or if a higher viscosity fluid is employed ($t_\mu \sim \mu^{-1}$), the viscous time scale will become important. It is therefore important to establish the limits of validity of the scaling analysis reported here in terms of the fluid properties and device geometry.

CHAPTER 5

MODELING OF THE INTERFACE EVOLUTION DURING EJECTION

The commercial computational fluid dynamics (CFD) software Fluent[72] is used to model the interface evolution during fluid ejection. Although the high-spatial-resolution visualization experiments have provided a detailed description of the ejection process, they are unable to fully validate the previously developed conceptual framework. It is likely that the phenomena that dictate the mode of ejection (i.e., discrete-droplet vs. continuous-jet) do not occur within the field of view of the microscope. Further, the most important features that determine the initial interface evolution (i.e., formation of a neck, its thinning and disruption, and eventual droplet ejection) occur within the nozzle orifice, and therefore are out of reach of the camera. The CFD analysis not only provides details of the flow within the liquid horns of the ejector before the fluid exits the orifice, but it also yields information about the flow within an ejected droplet or the jet itself.

The scaling analysis has been shown to accurately predict the physical conditions for which ejection is possible as well as what controls the mode of ejection for the range of experimental conditions investigated; indeed, the analysis presented in Chapter 4 is only appropriate when the interplay between acoustic pumping and surface tension controls the ejection process. However, as the orifice radius decreases or if the viscosity of the working fluid increases, viscous effects become important. The Fluent simulations, once validated using experimental data, allow one to perform "virtual" experiments in

order to establish the limits of validity of the scaling analysis, and therefore provide further insight into the physics governing the ejection process.

5.1 Volume of Fluid Method

5.1.1 Review of Techniques for Modeling Free-Surface Flows

The complexity associated with modeling free-surface flows motivates development of reduced-order methods and simplified equations which are still capable of capturing the fundamental physics governing these problems. To this end, a review of the techniques for modeling free-surface flows is given to establish the limits of applicability of each method.

The one-dimensional (1-D) or slender-jet approximations accurately describe the dynamics of drop formation and jet breakup for three-dimensional, axisymmetric and two-dimensional situations in which the fluid flow is directed mostly along the axis so that the velocity field is effectively one-dimensional. Although Lee[73] and Pimbley[74] earlier developed 1-D models while studying the dynamics of inviscid jets, only later had the first derivations of the correct set of 1-D counterparts of the Navier-Stokes (N-S) system of equations been carried out by Bechtel *et al*.[75] for jets in which inertia, viscosity, surface tension, and gravity were the dominant effects. They used a perturbation method to obtain 1-D equations to arbitrarily high order. Similar derivations have been performed by Ting and Keller[76] for an inviscid jet, and Eggers,[77] Eggers and Dupont,[78] Garcia and Castellanos,[79] and Papageorgiou[80] for viscous jets. Eggers and Dupont[78] and Garcia and Castellanos[79] coupled the surface tension/curvature term to all orders to the leading order approximations of other physical effects. Although this allowed their numerical results to closely match experiments, according to Bechtel *et al*.[81] this *ad hoc* model was not

derived self-consistently from the three-dimensional (3-D) N-S equations. The 1-D approximations are found to be broadly applicable close to pinchoff of a droplet that is grown quasi-statically, and recently Ambravaneswaran *et al*.[82] have evaluated the accuracy of 1-D algorithms over a wider range of governing parameters that included the effects of viscous, inertial, and capillary forces and found the approximations to be reasonably accurate.

The main contribution of the 1-D models has been a better understanding of the microscopic details of interface rupture. Shi *et al*.[83] and Brenner *et al*.[84] showed experimentally and computationally that a series of necks are formed from the main thread just before breakup. Eggers[77] demonstrated the continuation of the governing macroscopic equations through the point at which the interface ruptures by solving the 1-D equations before and after breakup. Although Eggers[47] has asserted that the 1-D models correctly predict the global shape, the drop size, and the length of the neck if higher-order corrections are included in the analysis, these models have not been able to capture these macroscopic features at any given flow rate and the microscopic features of the flow simultaneously.[85] For this reason, the 1-D Navier-Stokes equations are not expected to accurately predict the behavior of the flow presently under investigation.

The boundary element/boundary integral methods reduce the 3-D, axisymmetric problem to solution of a 1-D integral equation. Schulkes[86] analyzed drop formation of an inviscid fluid by numerically solving the potential flow problem using boundary integrals. By forcing the calculation to continue past the interface rupture, he was able to study the recoiling of the thread and the formation of satellite droplets. The opposite extreme of Stokes flow was considered by Zhang and Stone[87] who also applied boundary

integral methods to the analysis of droplet formation from a vertical capillary tube. The boundary element/boundary integral methods yield extremely accurate results for 3-D, axisymmetric flows; however, their utility is limited either to inviscid, irrotational cases or to Stokes flow situations.

Wilkes *et al*.[85] have attempted to address the shortcomings of 1-D slender jet approximations and boundary element/boundary integral methods by introducing a finite element method (FEM) for modeling drop formation from a capillary tube. This was accomplished by using a deforming mesh that conforms to the liquid phase allowing for extremely large interface deformations. The resulting computational algorithm was highly accurate and not restricted to the limit of creeping flow or that of irrotational flow of an inviscid fluid. The results reported by Wilkes *et al*.[85] extend only to the point of breakup; however, Notz *et al*.[88] have used the same FEM algorithm to extend this analysis beyond the bifurcation point. This analysis established the presence of overturning of portions of the interface; therefore, 1-D models could not be used to predict the dynamics of satellite droplets for the range of parameters considered.

Surface/volume tracking schemes are the most general methods for describing the break up and coalescence that occur in many free surface flows. Surface tracking methods include the front tracking scheme of Unverdi and Tryggvason,[89,90] an approach based on the level set method used by Sussman *et al*.,[91,92] and the surface capturing technique of Kelecy and Pletcher.[93] Volume tracking techniques include the marker and cell (MAC) method that was developed by Harlow and Welch[94] and volume of fluid (VOF) techniques first introduced by Hirt and Nichols.[95] In MAC, massless Lagrangian marker particles are advected with the local fluid velocity such that cells with markers are

the fluid and fluid cells that are bordering empty cells are the interface. In VOF, a fractional volume or color function is defined that indicates the fraction of a mesh cell that is filled with a particular fluid.

5.1.2 Methodology

The VOF technique is used in the present work due to its applicability to free surface flows where interface breakup and coalescence are important. A limited review of VOF methods has been presented by Eggers,[47] while a more comprehensive discussion of the evolution of VOF techniques including various advection methods is given by Rudman,[96,97] Rider and Kothe,[98] and Harvie and Fletcher.[99] The basic idea of VOF is to retain the volume data in each cell of a fixed computational domain as a volume fraction *C*, thereby mixed cells that define the interface between two fluids will have a volume fraction between zero and one, and cells away from the interface will have a volume fraction equal to zero or unity. The interface between two fluids is then tracked by advancing fluid volumes forward in time through the solution of an advection equation.

5.1.2.1 Modeling Technique

If inertia, viscosity, and surface tension are the dominant effects, the 3-D non-dimensionalized Navier-Stokes equations of motion for a two-phase (liquid-gas), incompressible fluid are

$$\frac{\partial C}{\partial t} + \nabla \cdot \left(\mathbf{U} C \right) = 0 \,, \tag{19}$$

$$\rho = \rho_1 C + \rho_2 \left(1 - C \right), \tag{20}$$

$$\frac{\partial \rho \mathbf{U}}{\partial t} + \nabla \cdot \left(\rho \mathbf{U} \mathbf{U} \right) = -\nabla P + \frac{1}{\mathrm{We}} \mathbf{F}_\mathrm{s} + \frac{1}{\mathrm{Re}} \nabla \cdot \boldsymbol{\tau} \,, \text{ and} \tag{21}$$

$$\nabla \cdot \mathbf{U} = 0\,, \tag{22}$$

where C is the volume fraction of the liquid, $\mathbf{U}$ is the velocity vector, P is pressure, $\mathbf{F_S}$ is a body force that is used to account for interfacial effects, $\boldsymbol{\tau}$ is the shear stress tensor, and the dimensionless density ρ is the weighted average of the scaled densities, ρ_1 and ρ_2, of the two fluids, the liquid and gas in this case (note that all other properties, e.g., viscosity, are also computed in this manner).[97] The Weber number We and Reynolds number Re are expressed as

$$\mathrm{We} = \frac{\rho_o U^2 l}{\sigma} \text{ and } \mathrm{Re} = \frac{\rho_o U l}{\mu_o}\,, \tag{23}$$

where U and l are appropriate velocity and length scales, respectively, ρ_o and μ_o are the density and viscosity scales, respectively, for the liquid, and σ is the surface tension between the participating fluids (72.5×10^{-3} N/m for water in air). Details of the implementation of the volume of fluid (VOF) solution technique in Fluent are provided in Appendix G.

5.1.2.2 Incorporating the Effect of Surface Tension

In Equations (19)–(22), the effect of interfacial tension has been accounted for through the use of an equivalent virtual body force as first introduced by Brackbill *et al.*[100] as the continuum surface force (CSF) method. This is the same model that is used by Fluent.[72] An expression for the body force due to surface tension is given by Rudman[97] as

$$\mathbf{F_S} = \kappa \delta(r_I)\hat{\mathbf{n}}\,, \tag{24}$$

where κ is the radius of curvature of the interface at a location r_I, $\delta(r_I)$ is a one-dimensional indicator function that is zero everywhere except at the interface, and $\hat{\mathbf{n}}$ is

the unit normal to the interface. The unit normal, $\hat{\mathbf{n}} = \mathbf{n}/|\mathbf{n}|$, is constructed from the interface normal $\mathbf{n} \equiv \nabla C$, where as before, C is the scalar function that indicates the volume fraction of the liquid in a given computational cell. The curvature κ is defined in terms of the divergence of the unit normal, $\kappa = \nabla \cdot \hat{\mathbf{n}}$. It is also convenient to define the interface indicator function $\delta(r_I) = |\mathbf{n}|$.[97] Richards *et al.*[101,102] accounted for surface tension by implementing the same technique in cylindrical, axisymmetric coordinates.

5.1.2.3 Advection of the Volume Fraction C

The greatest variation between implementations of VOF techniques is found in the method by which the volume faction C is advected. Interface geometry reconstruction methods usually fall into one of two general categories, piecewise constant or piecewise linear. Although multidimensional algorithms exist, typical implementations are still quasi-one-dimensional and operator splitting, i.e., performing an x_i-direction sweep followed by an x_j-direction sweep, is used to obtain multidimensionality. The simplest reconstruction technique is the simplified line interface calculation (SLIC) method that defines the interface in a cell using a straight line parallel to one of the coordinate directions. The method of Hirt and Nichols[95] is similar in principle to SLIC, but uses eight neighboring cells to estimate the surface normal, whereas in SLIC only the four adjacent cells are used. A more accurate interface reconstruction technique was introduced in Youngs'[103] VOF method. The interface within a cell is approximated by a straight line segment that cuts the cell such that the fractional fluid volume is conserved. Increased accuracy is achieved because the interface does not have to be parallel to one

of the coordinate directions. Fluent[72] uses Youngs'[103] advection scheme to track the liquid-air interface.

5.1.2.4 Simulation Domain

Fluent simulations are performed for conical, 3-D axisymmetric nozzles, which are represented by the two-dimensional (2-D) domains shown in Figure 5.1. Results are obtained for both microchannel-based (type 1, Figure 5.1a) and membrane-based (type 2, Figure 5.1b) nozzle terminations. In both cases, the circular sector (AN in Figure 5.1a and AFP in Figure 5.1b) centered at point C serves as the fluid inlet. The walls of the nozzle and microchannel (or membrane) are represented by line NGHK in Figure 5.1a (or PNGHK in Figure 5.1b), the fluid outlet by lines KLMJF and KLMJE in Figures 5.1a and 5.1b, respectively, and the axis of symmetry by line ABDEF in Figure 5.1a and line AOBDE in Figure 5.1b. Lines DH and BH in Figures 5.1a and 5.1b, respectively, represent the nozzle orifice.

For simulations using the type 1 domain (Figure 5.1a), the centerline distance l_c from the fluid inlet to the nozzle orifice is 30 μm, the length l_{mc} of the microchannel at the nozzle tip is 10 μm, and the radius r_o is 3 μm (corresponding to an orifice diameter of 6 μm). For all simulations using the type 2 domain (Figure 5.1b), the half-width (radius) and thickness of the membrane are set at 10 and 2.5 μm, respectively. In addition, ejection from orifices with radii of 1.5, 2.5, and 6.5 μm is simulated. The centerline distance from the fluid inlet to the nozzle orifice is set at 27.5 μm for domains with 1.5 and 2.5 μm radius orifices, and is increased to 47.5 μm for the 6.5 μm radius orifice.

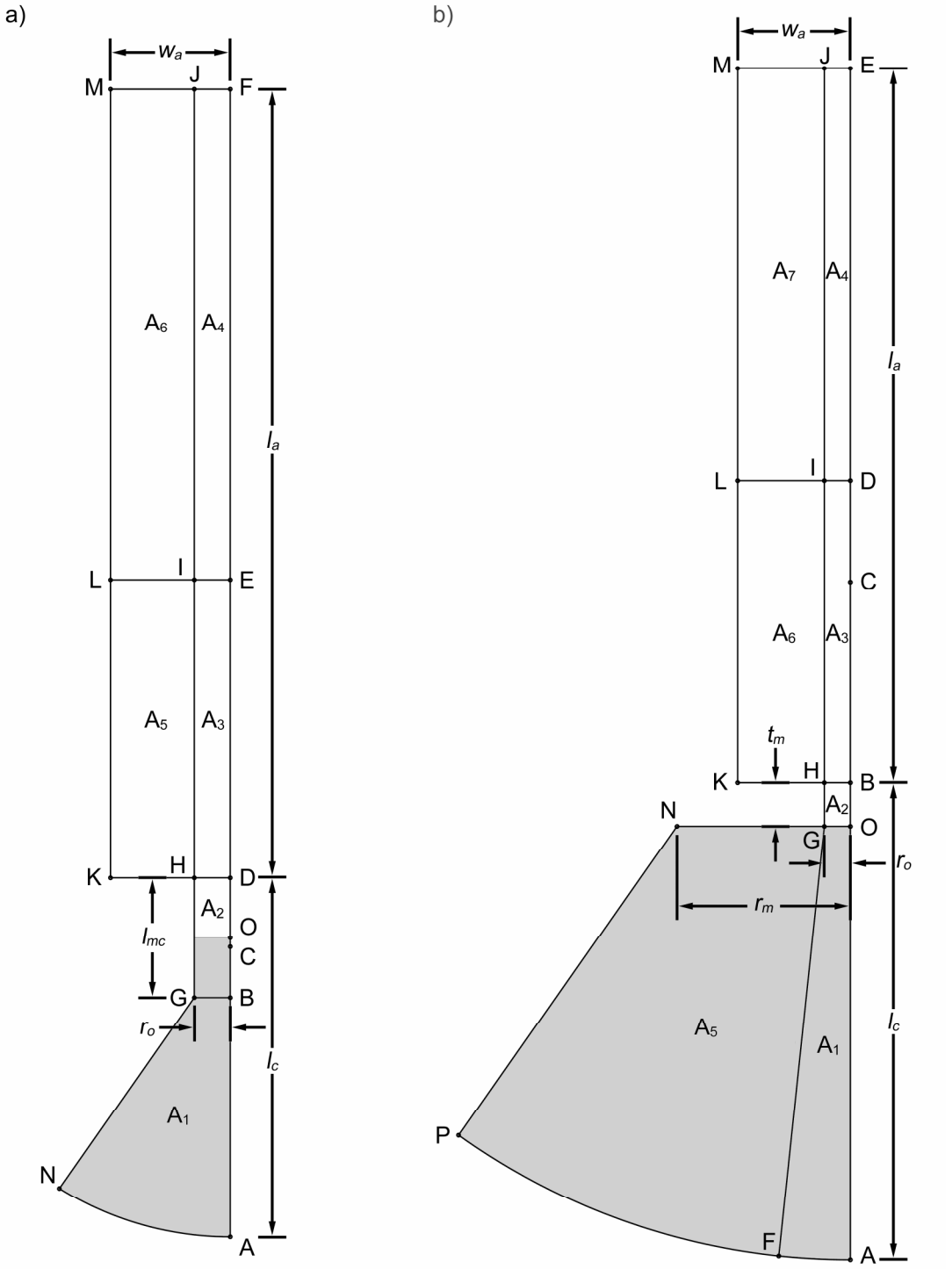

Figure 5.1. Two-dimensional (2-D) computational domains used to simulate ejection from conical, three-dimensional (3-D) axisymmetric nozzles representing the pyramidal nozzles of the ejector: a) domain with microchannel nozzle termination and b) domain with membrane nozzle termination. The nozzle domain initially filled with liquid is shaded.

Sensitivity studies were performed to minimize grid dependency on the mesh density, cell shape, and domain size. It is recommended that quadrilateral elements be used in portions of the domain where surface tension effects are thought to be important;[72] however, a comparison of results obtained by meshing the interior of the nozzle (area A_1 in Figure 5.1a and areas A_1 and A_5 in Figure 5.1b) with triangular and mapped quadrilateral elements for both 2-D simulation domains revealed no noticeable difference in the observed interface evolution.

The size and shape of the elements within the microchannel (or membrane orifice) are found to have the greatest effect on the simulation results. If the element size is not small enough to capture the quickly advancing interface during the "push"-half of the ejection cycle, air will become artificially trapped within the liquid phase. This problem is minimized by meshing the area within the microchannel (or membrane orifice) with mapped quadrilateral elements with a radial mesh density ranging from 10 elements per μm for the 1.5 μm radius orifice to approximately 4 elements per μm for the 6.5 μm radius orifice and an axial mesh density of 10 elements per μm for all cases; however, even with this refined mesh, the presence of trapped air remains a problem for the cases exhibiting transition (continuous-jet to discrete-droplet mode of ejection) behavior.

The sensitivity of the results with respect to the size (width w_a and length l_a) of the external domain was also investigated. As long as w_a is greater than three orifice diameters and l_a is long enough to capture two wavelengths (droplet-to-droplet or interface crest-to-interface crest) of the ejection cycle no difference is observed in the ejection results. For the type 1 simulation domain, the minimum length (40 μm) of the external domain is limited by a maximum ejection velocity of ~20 m/s and a minimum

operating frequency of 1 MHz. Since all simulations using the type 2 domain are performed at an ejection velocity of approximately 10 m/s (see Section 5.4), the minimum length of the external domain is also limited to 40 μm by the lowest operating frequency (500 kHz) investigated.

5.1.2.5 Initial and Boundary Conditions

The velocity field and gage pressure are initialized to 0 for the entire simulation domain. A liquid volume fraction of 1 is then "patched" on the cells in the portion of the domain representing the nozzle, i.e., the nozzle is initially filled with liquid as illustrated by the shaded areas of Figure 5.1. In addition, it is recommended that the reference pressure be located at a position that will always contain the gas phase.[72] Therefore, the reference pressure location is moved from the default origin point O to a location near point M (see Figure 5.1).

The ANSYS[36] simulations indicate that the amplitude of the oscillating pressure field is uniform along a hemispherical section centered around the orifice. Therefore, an oscillating pressure boundary condition is applied to the circular sector (lines AN and AFP in Figures 5.1a and 5.1b, respectively) representing the fluid inlet using a user defined function (UDF) in Fluent. The amplitude A_P of this oscillating pressure is used to control the velocity of the ejected fluid such that a valid comparison between the Fluent simulations and experiments can be made. The boundary of the external domain is specified as a pressure-outlet in Fluent,[72] which uses a global mass balance to ensure that the outflow is equal to the inflow at the fluid inlet.

A no-slip condition is applied at the walls of the nozzle and microchannel (or membrane). In conjunction with the surface tension model described above, a wall

contact angle θ_w of 90° is prescribed. Following the method of Brackbill *et al.*,[100] this contact angle is not imposed as a boundary condition at the wall itself, but rather the contact angle that the fluid is assumed to make with the wall is used to adjust the surface normal in cells near the wall so that the surface normal of cells adjacent to the wall is

$$\hat{n} = \hat{n}_w \cos\theta_w + \hat{t}_w \sin\theta_w, \tag{25}$$

where $\hat{n}_w$ and $\hat{t}_w$ are the unit vectors normal and tangential to the wall, respectively.

5.1.2.6 Convergence and Determination of Periodic Steady State

An implicit time discretization scheme with a time step of $5\text{x}10^{-10}$ s is used in the solution of the momentum and continuity equations. Fluent uses an explicit time-marching scheme to solve the volume fraction advection equation.[72] The time step used in the explicit scheme is automatically determined to ensure stability of the solution; however, the time step calculation can be influenced by modifying the Courant number (see Appendix G). Convergence within each time step is achieved when the residuals corresponding to the velocity components and continuity drop to $1\text{x}10^{-7}$, which usually occurs after approximately 20 iterations. This represents a decrease in the residuals of about four orders of magnitude.

Solution of the transient problem is concluded when a periodic steady state is reached, i.e., the liquid air interface profile at a particular phase of the ejection cycle is identical to the profile at the same phase of the previous cycle. Starting from the initially flat liquid-air interface at the nozzle orifice, most simulations achieve a periodic steady state after approximately 15–20 ejection cycles.

5.2 Validation of the Simulations

Validation of the Fluent simulations has been achieved through a comparison of the predicted interface evolution and the high-spatial-resolution images that were acquired during the visualization experiments. Experimentally-acquired images corresponding to the discrete-droplet and continuous-jet modes of ejection, along with the transition from jet to droplet ejection, were used for the validation study. The experiments were performed with the first device design (type 1 from Chapter 4) that featured a short channel with a length of approximately 5.0 μm and a 5.9 μm diameter orifice. For this device, discrete-droplet and continuous-jet ejection occurred at driving frequencies of 0.952 and 2.100 MHz, respectively; the transition between these two modes of operation was found at an operating frequency of 1.463 MHz. The type 1, 2-D axisymmetric domain used to simulate ejection from this device is shown in Figure 5.1a. The centerline distance from the oscillating pressure boundary to the nozzle exit was 30 μm, and the microchannel at the apex of the nozzle was 10 μm long and 3 μm in radius (corresponding to an orifice diameter of 6 μm). As was previously discussed, the amplitude A_P of the oscillating pressure at the boundary representing the fluid inlet was adjusted in order to achieve a desired ejection velocity. Since the amplitude of the acoustic pressure at the boundary is not measurable, for each of the simulations performed in the validation study, an attempt was made to adjust A_P in order to exactly match the ejection velocity to that observed experimentally.

Figures 5.2a through 5.2c provide side-by-side comparisons of the simulation results and experimentally-obtained images for each of the observed modes (discrete-droplet, continuous-jet, and transition) of ejection. Although good qualitative agreement

is seen between the simulation results and the acquired images for the droplet and jet ejection cases (Figures 5.2a and 5.2c, respectively), the transition from droplets to jet is not predicted at a frequency of 1.463MHz; the simulations show ejection of a continuous jet. This is, however, not surprising as the Fluent simulations cannot be expected to predict the exact frequency at which the transition from droplet to jet ejection occurs. Even this rather sophisticated analysis involves making a number of idealizations, including the geometry of the simulation domain (e.g., representing pyramidal nozzles by axisymmetric cones), and a large number of variables are not necessarily accounted for in the model (e.g., contact angle evolution and thermal effects due to viscous heating are neglected, which may affect relevant physical properties such as density, viscosity, and

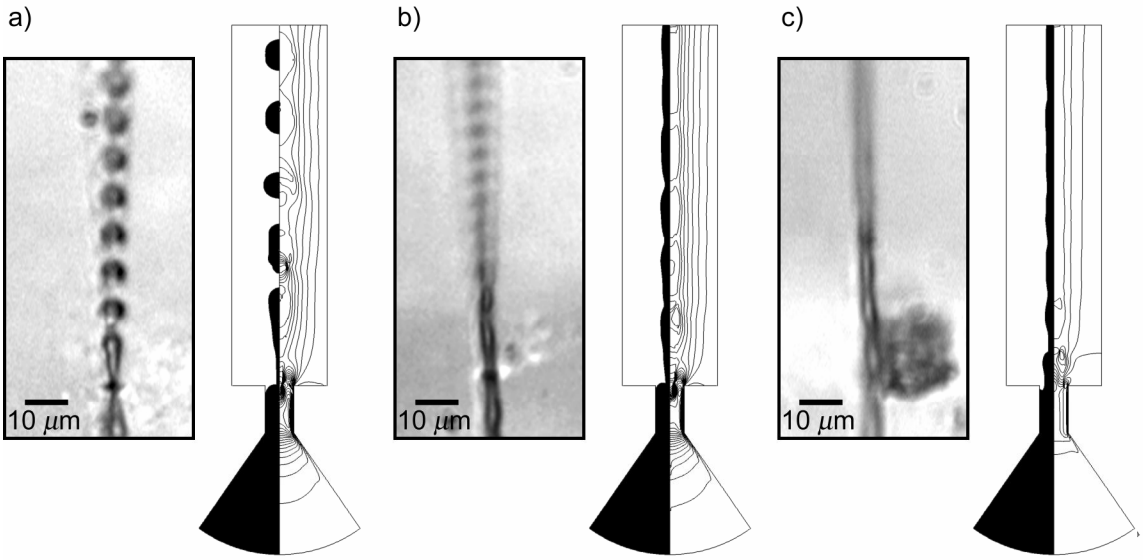

Figure 5.2. Comparison of experimentally-acquired images and simulations of fluid ejection from the ~6.0 μm orifice of a device with short channels at the tips of the nozzles: a) discrete-droplet mode of ejection at a frequency of 0.952 MHz and droplet velocity of 12 m/s, b) transition from droplet to jet mode of ejection at a frequency of 1.463 MHz and droplet/jet velocity of 21 m/s, and c) continuous-jet mode of ejection at a frequency of 2.100 MHz and a jet velocity of 22 m/s. The left side of the simulated virtual ejection images shows the interface profile, and the right provides contours of the axial velocity, which ranges from a maximum of ~40 m/s within the channel to a minimum of between 12 and 20 m/s in the ejected liquid.

surface tension). However, based on the simulation results shown in Figures 5.2a and 5.2b, the transition from discrete-droplet to continuous-jet mode of ejection is predicted to occur within a fairly narrow range of frequencies between 0.952 and 1.463 MHz, which indicates that the simulations do in fact capture the essential physics governing the ejection process.

5.3 Confirmation of the Conceptual Description of the Ejection Process

By enabling the interface evolution within the nozzle orifice to be observed during the ejection process, the Fluent simulations can confirm the description of the ejection process introduced in Chapter 4 and used as a conceptual framework for the scaling analysis. Figure 5.3 provides sequential virtual images of simulated droplet ejection from the 1.5 μm radius orifice of the type 2 simulation domain. For this case, the frequency of the oscillating pressure boundary condition at the fluid inlet is 1.0 MHz. Figure 5.4 provides sequential virtual images of jet ejection from the 6.5 μm radius orifice of the type 2 simulation domain at a driving frequency of 1.0 MHz. The delay between successive images is such that a complete period of ejection is shown for each case.

In Figure 5.3, the "push"-half cycle during which the fluid is pushed out of the nozzle orifice and accelerated by the positive pressure gradient is represented by frames 1 through 5. During the other "pull" half of the cycle (frames 5 through 9), the negative pressure gradient slows down and reverses the direction of flow, thus forming and thinning the neck upstream of the ejected fluid volume.

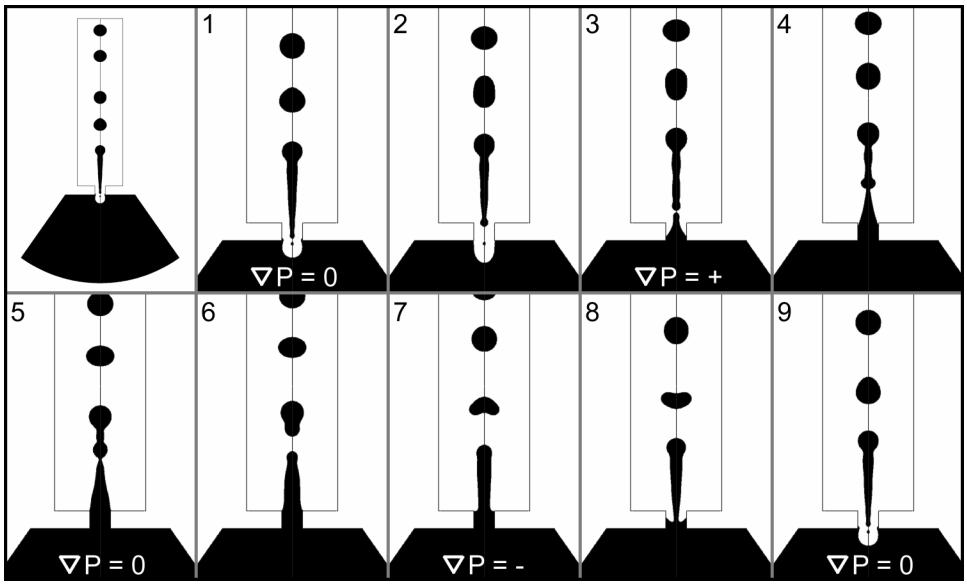

Figure 5.3. Fluent simulation results representing the interface profile at different instants of time during a single period of discrete-droplet ejection from a 3.0 μm diameter orifice at 1.0 MHz.

Similar behavior is seen in Figure 5.4. In the first five frames, the positive pressure gradient pushes the fluid from the nozzle orifice, and in frames 5 through 9, the negative pressure gradient acts to reverse the direction of flow and thin the neck of the ejected fluid; however, in this case, the neck is not sufficiently thin to allow surface tension to break the interface, and a wavy, continuous jet results. The simulations therefore confirm the conceptual framework put forward earlier (Figure 4.11 of Chapter 4) that describes the origin and mechanisms of the droplet ejection process. This also indirectly validates the method and predictions of the scaling analysis, which was developed in Chapter 4 based on this conceptual understanding of the ejection physics to successfully predict the modes of ejection observed in the experiments.

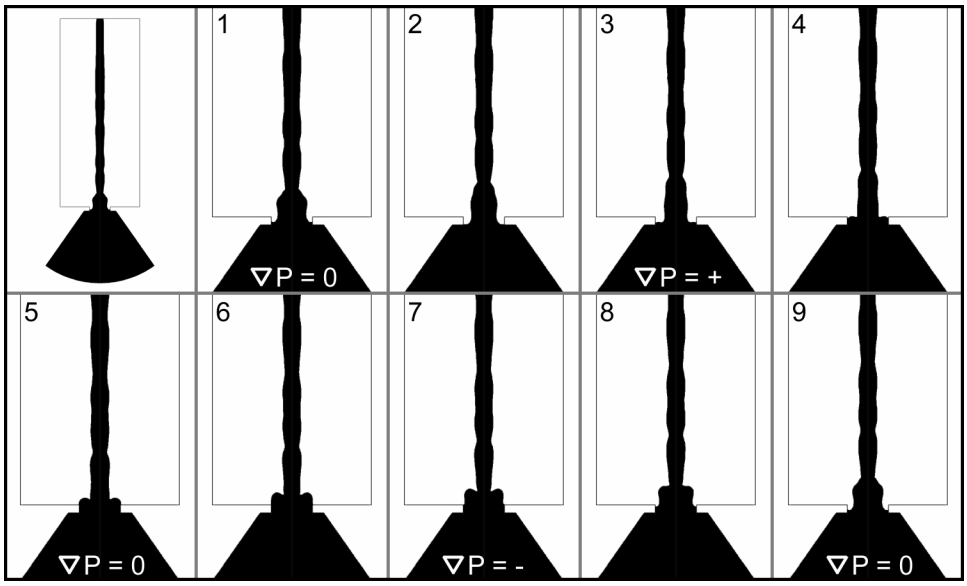

Figure 5.4. Fluent simulation results representing the interface profile at different instants of time during a single period of continuous-jet ejection from a 13.0 μm diameter orifice at 1.0 MHz.

5.4 Validation of the Scaling Analysis Using the Simulations

In order to determine the limits of validity of the scaling analysis discussed in Chapter 4, simulations are performed for a range of test conditions with the geometry of the type 2 domain shown in Figure 5.1b. For all simulations, the half-width (radius) and thickness of the membrane are set at 10 and 2.5 μm, respectively. Ejection from orifices with radii of 1.5, 2.5, and 6.5 μm is investigated at frequencies ranging from 0.5–2.0 MHz. The centerline distance from the oscillating pressure boundary to the exit of the nozzle is set at 27.5 μm for domains with the 1.5 and 2.5 μm radius orifices, and is increased to 47.5 μm for the 6.5 μm radius orifice. In order to remove the effect of changing velocity, an attempt is made to adjust the amplitude A_P of the process-driving pressure oscillation representing the fluid inlet boundary condition such that the velocity of the resulting droplets/jet will be approximately 10 m/s for the cases used to validate the scaling analysis.

Table 5.1 provides a summary of the time scales for water ejection from the nozzle geometries described above, as computed from virtual Fluent simulation experiments. As predicted by the scaling analysis, the simulated inertial time scale t_U is the smallest time scale for all cases. The scaling analysis argument that the relationship between the process time scale t_f and the capillary time scale t_σ prescribes the mode (discrete-droplet vs. continuous-jet) of ejection is also supported by the simulation data corresponding to ejection from the 1.5 and 6.5 μm radius orifices (Table 5.1). Indeed, for these nozzles, when $t_f > t_\sigma$, ejection does occur as discrete droplets (Figure 5.5a), and when $t_f < t_\sigma$, ejection of a continuous jet is observed (Figure 5.5c). In addition, for the two cases of ejection from the 6.5 μm radius orifice with time scales corresponding to transition behavior ($t_f \sim t_\sigma$), it appears that a continuous-jet is ejected and then quickly breaks into droplets approximately two wavelengths from the exit of the orifice as shown in Figure 5.5b (as previously mentioned, operation near the transition from discrete-droplet to jet mode of ejection exhibits greater problems with air becoming trapped within the liquid). Thus, these simulation results unconditionally support the conclusions of the scaling analysis.

The data corresponding to ejection from the 2.5 μm radius orifice in Table 5.1 also follow the trend predicted by the simple scaling analysis, but it appears that the transition from discrete-droplet to continuous-jet mode of ejection is predicted to occur at lower frequencies than expected. For the two highlighted cases, $t_f > t_\sigma$, yet jet-mode ejection is clearly observed. Granted, the magnitude of the process time scale is greater than but very close to that of the capillary time scale for both cases, and so these data

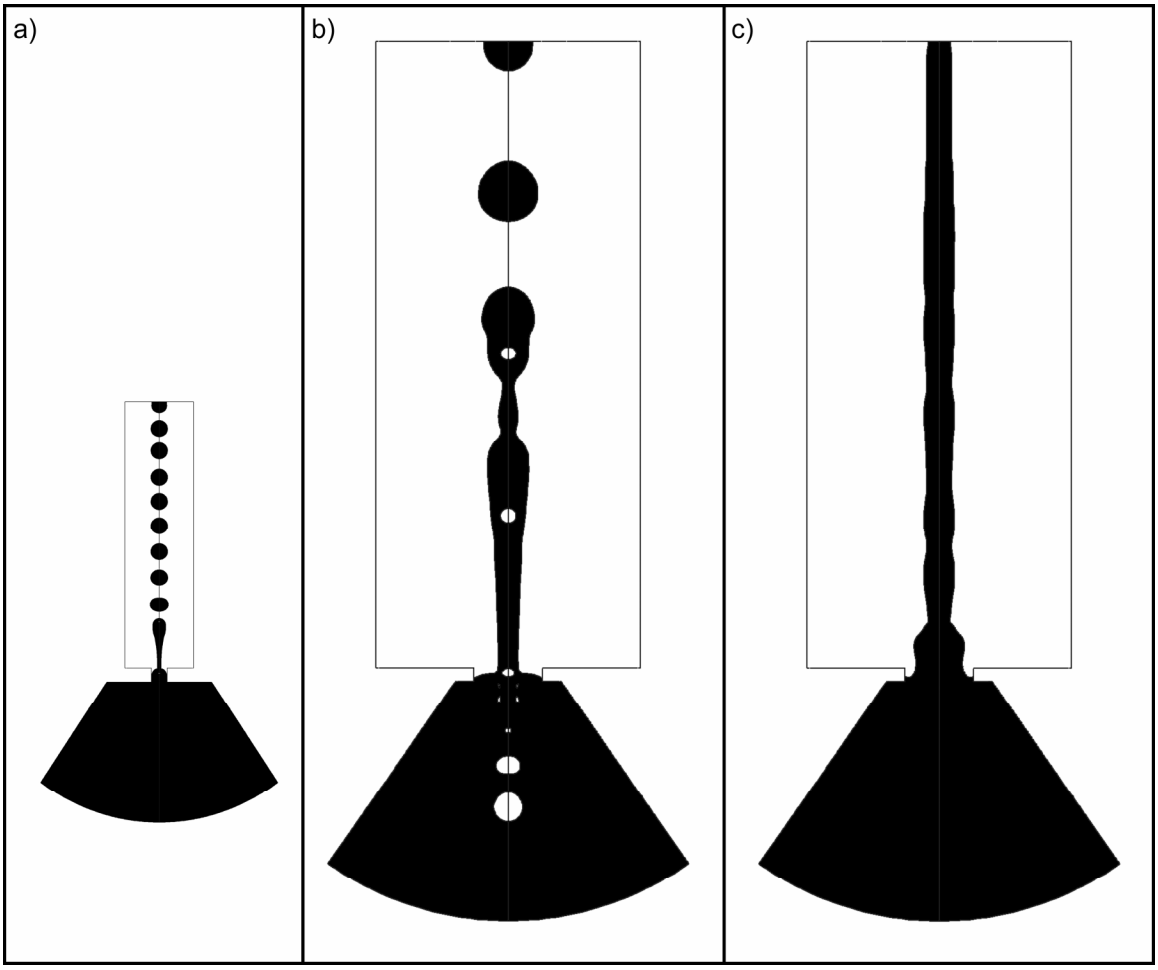

Figure 5.5. Fluent simulation results representing the three observed modes of ejection: a) discrete-droplet mode of ejection from a 3.0 μm diameter orifice at 2.0 MHz, b) transition from discrete-droplet to continuous-jet mode of ejection from a 13.0 μm diameter orifice at 0.500 MHz, and c) continuous-jet mode of ejection from a 13.0 μm diameter orifice at 2.0 MHz.

could also fall into the jet-to-droplet transition regime due to the approximate (order-of-magnitude) nature of the scaling analysis method; however, perhaps another phenomenon is at work. As the radius of the orifice decreases, the viscous time scale ($t_\mu \sim r_o^2$, see chapter 4) approaches the process and capillary time scales. Indeed, for the 1.5 and 2.5μm radius orifices, t_μ is only at most one order of magnitude greater than t_f and t_σ, and thus viscous effects may become important and need to be taken into account. The

Table 5.1. Summary of operating parameters and time scales for simulation of ejection from the orifice of two-dimensional (2-D) axisymmetric nozzle with a 10 μm wide, 2.5 μm thick membrane.

Mode	Frequency, f (MHz)	Orifice Radius, r_o (μm)	Process Time Scale, t_f (μs)	Inertial Time Scale, t_U (μs)	Capillary Time Scale, t_σ (μs)	Viscous Time Scale, t_μ (μs)
D	0.500	1.5	2.00	0.15	0.22	2.51
D	0.667	1.5	1.50	0.15	0.22	2.51
D	1.000	1.5	1.00	0.15	0.22	2.51
D	1.500	1.5	0.67	0.15	0.22	2.51
D[a]	2.000	1.5	0.50	0.15	0.22	2.51
D	0.500	2.5	2.00	0.25	0.46	6.98
D	0.667	2.5	1.50	0.25	0.46	6.98
D	1.000	2.5	1.00	0.25	0.46	6.98
J	1.500	2.5	0.67	0.25	0.46	6.98
J	2.000	2.5	0.50	0.25	0.46	6.98
T[b]	0.500	6.5	2.00	0.65	1.95	47.17
T	0.667	6.5	1.50	0.65	1.95	47.17
J	1.000	6.5	1.00	0.65	1.95	47.17
J	1.500	6.5	0.67	0.65	1.95	47.17
J[c]	2.000	6.5	0.50	0.65	1.95	47.17

[a] Operating point shown in Figure 5.5a exhibiting discrete-droplet ejection.
[b] Operating point shown in Figure 5.5b exhibiting transition behavior.
[c] Operating point shown in Figure 5.5c exhibiting continuous-jet ejection.

transition from discrete-droplet to continuous-jet mode ejection for the 1.5 μm radius orifice is not observed in the data provided in Table 5.1 because the capillary time scale is sufficiently small that discrete-droplets are always produced; however, the data for the 2.5 μm radius orifice clearly indicate that the transition has shifted to a lower frequency than that predicted by a comparison of the process and capillary time scales. In summary, conclusions drawn from comparing the relevant time scales calculated using the scaling analysis of the data of Table 5.1 do accurately predict the trends observed in the

simulation results; however, it appears that the limits of validity of the scaling analysis are being approached for the smallest orifices under investigation.

5.5 Additional Simulated Ejection Phenomena

In addition to confirming the conceptual description of the ultrasonically-driven ejection process and finding the limits of validity of the scaling laws introduced in Chapter 4, the Fluent simulations are also used to investigate other phenomena including the variation of the droplet diameter with driving frequency and the effect of increasing the amplitude of the oscillating pressure boundary at the fluid inlet.

Simulated images of droplets "virtually" ejected from the 1.5 μm radius orifice of the type 2 simulation domain operating at 0.5, 0.67, 1.0, 1.5, and 2.0 MHz are shown in Figure 5.6 along with a log-log plot of the droplet diameter as a function of frequency. Although it is obvious that the simulated droplet diameter decreases with increasing frequency as expected, a regression analysis performed using statistical analysis software (SigmaPlot,[71] version 7.0) indicates that $d_d \sim f^{-0.19}$ (dark black line in Figure 5.6), which is a significantly weaker relationship than that found experimentally ($d_d \sim f^{-0.38}$ from Section 4.4.1 and gray dashed line in Figure 5.6) or that predicted through a simple consideration of mass conservation ($d_d \sim f^{-0.33}$ from Section 4.4.1 and light gray lines in Figure 5.6). One possible explanation for this result relates to the artificially trapped air for cases where the simulations are unable to properly track the rapidly advancing interface during the "push"-half of the ejection cycle. The interface recedes much further into the fluid chamber for droplet generation at lower frequencies. When more air is trapped within the chamber, less volume of fluid is available to be ejected as a droplet.

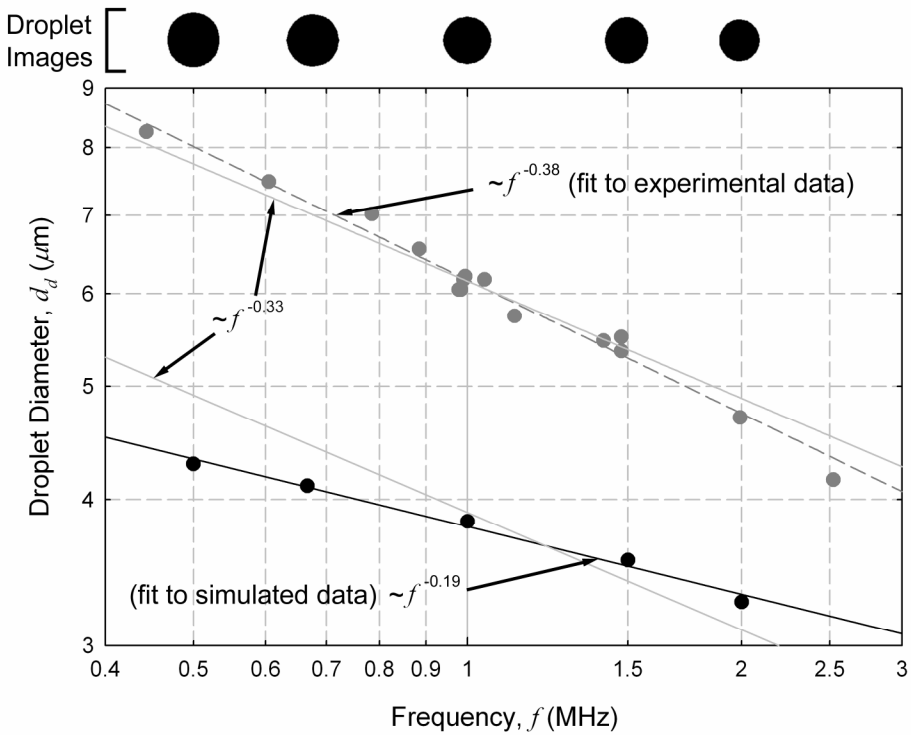

Figure 5.6. Simulated droplet diameter d_d as a function of frequency f for ejection from the 3.0 μm diameter orifice of the type 2 simulation domain. The relationship $d_d = f^{-0.20}$ fit to the simulation results (black line) is weaker than that predicted by the experimental results ($d_d = f^{-0.38}$ and gray dashed line) or a mass balance of the fluid contained within a droplet before and after ejection ($d_d = f^{-0.33}$ and light gray line).

For operation at higher frequencies, the push-pull behavior of the oscillating pressure gradient is more confined to the orifice itself and a gradual change in the slope of a curve fit to the data is seen at frequencies above 1.5 MHz as shown in Figure 5.6.

Figure 5.7 provides images of virtual droplet ejection from the 1.5 μm radius orifice of the type 2 simulation domain at three different amplitudes of the oscillating pressure boundary condition representing the fluid inlet and a driving frequency of 1.0 MHz. The amplitude A_P of the oscillating pressure located at a distance l_c = 27.5 μm from the orifice is 4.8, 5.0, and 5.2 atm (486, 507, and 527 kPa) for the simulation results shown in Figures 5.7a, 5.7b, and 5.7c, respectively. The velocity of the droplets increases

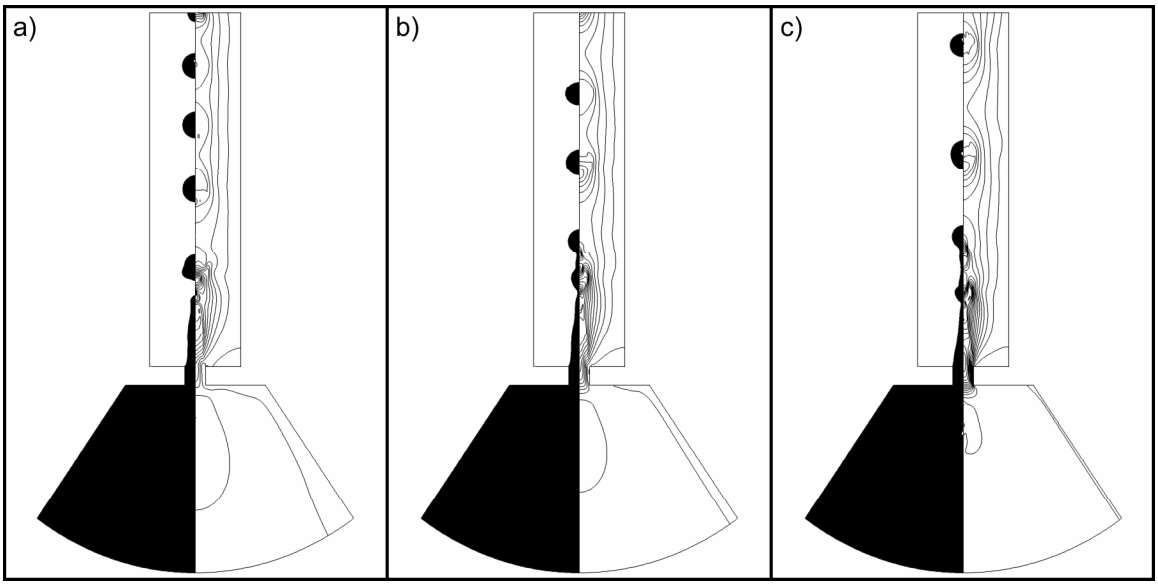

Figure 5.7. Simulated droplet ejection at a frequency of 1.0 MHz as a function of the amplitude A_P of the oscillating pressure boundary representing the fluid inlet: a) U_d = 11 m/s (A_P = 4.8 atm), b) U_d = 13.5 m/s (A_P = 5.0 atm), and c) U_d = 16 m/s (A_P = 5.2 atm). The left side of the simulated ejection images shows the interface profile, and the right provides contours of the axial velocity.

linearly with A_P from 11 m/s at 4.8 atm to 13.5 m/s at 5.0 atm and 16 m/s at 5.2 atm. In addition, the droplet diameter remains relatively constant as the ejection velocity increases.

5.6 Concluding Remarks on the Simulation of the Ejection Process

In this chapter, experimentally-validated computational fluid dynamics (CFD) simulations of the interface evolution during fluid ejection have been used to confirm the conceptual description of the ejection process introduced in Chapter 4. Specifically, simulated images of discrete-droplet ejection from a 1.5 μm radius orifice at a driving frequency of 1.0 MHz and continuous-jet ejection from a 6.5 μm radius orifice at 1.0 MHz support this conceptual understanding of the ejection physics that prescribe the mode (discrete-droplet vs. continuous-jet) of ejection and therefore indirectly validate the predictions of the scaling analysis developed in Chapter 4. Both simulations were

performed on a 2-D domain representing a conical, 3-D axisymmetric nozzle terminating in a 20 μm wide, 2.5 μm thick membrane.

In addition to confirming the conceptual theoretical developments of Chapter 4, simulations have been used to determine the limits of validity of the scaling analysis. As was previously discussed, for all experimental cases, the viscous time scale t_μ was one to two orders of magnitude greater than the time scales for the acoustic pumping frequency (process) t_f and surface tension (capillary) t_σ. In order to increase the importance of the viscous time scale with respect to the ejection process, simulations were performed for smaller orifices ($t_\mu \sim r_o^2$, see Chapter 4). In particular, the time scales for water ejection from 1.5, 2.5, and 6.5 μm radius orifices of the nozzle geometry described above operating at driving frequencies between 0.5 and 2.0 MHz were computed from simulated virtual experiments. This analysis has led to the following specific conclusions:

- As in the visualization experiments, two distinct modes of ejection are observed: discrete-droplet and continuous-jet. A gradual transition between operating modes when a continuous jet breaks up within ~1–2 wavelengths of the orifice is also seen for operation of the 6.5 μm radius orifice at the lowest driving frequencies (0.5 and 0.67 MHz). The droplet diameter is shown to decrease with increasing frequency although the frequency dependence ($d_d \sim f^{-0.20}$) is weaker than that predicted experimentally ($d_d \sim f^{-0.38}$) or through a simple consideration of mass conservation ($d_d \sim f^{-0.33}$). In addition, a linear increase in the ejection velocity is observed with an increase in the amplitude of the oscillating pressure boundary representing the fluid inlet, while the droplet diameter d_d remains relatively constant with increasing ejection velocity as was suggested in Chapter 4.

- A comparison of relevant time scales enables the criterion for gradual transition from discrete-droplet to continuous-jet mode of ejection to be established. As in the experimental time scale analysis, the process time scale, $t_f = 1/f$, the inertial time scale, $t_U = r_o/U$, the capillary time scale, $t_\sigma = (\rho r_o^3/\sigma)^{1/2}$, and the viscous time scale, $t_\mu = \rho r_o^2/\mu$, are found to play important roles in the ejection process. For the 1.5 and 6.5 μm radius orifices, when $t_\sigma > t_f$, continuous-jet ejection results, and $t_\sigma < t_f$ leads to ejection of a stream of individual droplets. In addition, the transition from continuous-jet to discrete-droplet mode of ejection has been found to occur when $t_f \sim t_\sigma$.
- Both discrete-droplet and continuous-jet mode of ejection from the 2.5 μm radius orifice are observed for operation over the frequency range of interest; however, the time scale analysis predicts that the transition from droplet to jet ejection should not occur until the operating frequency is increased to approximately 2.2 MHz for this orifice. The viscous time scale ($t_\mu \sim r_o^2$) for the 2.5 μm radius orifice is only one order of magnitude greater than t_f and t_σ, and thus viscous effects appear to be important and need to be accounted for in the time scale analysis for ejection of a high viscosity fluid or from a small orifice. Therefore, although a comparison of the relevant times scales resulting from analysis of the virtual ejection experiments does accurately predict the trends observed in the simulation results, for the smallest orifices under investigation the limits of validity of the scaling laws developed in Chapter 4 are being approached.

CHAPTER 6

APPLICATIONS UTILIZING THE MICROMACHINED ULTRASONIC ATOMIZER

In this chapter, three case studies are presented to illustrate the breadth of applications of the micromachined ultrasonic atomizer. In particular, the following three applications are described:

- The device has been found to be particularly well-suited to atomization of liquid fuels for small-scale, portable power generation due to its ability to achieve a high degree of control of the ejection process at low flow rates and with low power consumption.[17] Successful ejection of representative fuels is presented, and resulting atomization quality is discussed.
- The device potential for drug delivery applications has been demonstrated. Specifically, the ultrasonic atomizer has been found to meet the stringent requirements (in terms of droplet size, distribution, and volume and virus viability) of inhalation delivery of the measles vaccine.
- Lastly, the capability for ultra-soft ionization enabled by the ultrasonic atomizer used as an electrospray ion source for bioanalytical mass spectrometry has been shown by achieving efficient biomolecule charging and dry ion formation at a very low applied ionization voltage and also using pure water as a solvent.[14]

6.1 Atomization of Liquid Fuels for Microscale Fuel Processing

Existing battery technologies have become a major obstacle to advances in the performance of portable energy-intensive devices primarily due to a limited lifetime between charge cycles.[104,105] Fuel-cell-based energy sources are a viable alternative due to the high energy density stored in liquid fuels and the potential for high efficiency power generation. Recent work has focused on the development of two types of fuel cells for portable applications, hydrogen-based fuel cells with external fuel reformation, i.e., conversion to hydrogen, and direct-methanol fuel cells that oxidize methanol directly at the cell anode.[104,106] Regardless of whether internal or external fuel reformation is used, energy-efficient atomization of liquid fuels ranging from methanol to higher hydrocarbons and diesel to kerosene and logistic fuels, e.g., JP-8, is an essential processing step for conversion of a fuel from liquid to gas phase.

The micromachined ultrasonic atomizer developed in this thesis is particularly well-suited to these applications because it is capable of highly controlled atomization of a variety of liquid fuels at low flow rates. The low-flow-rate requirement intrinsic to the small-scale, portable power application is especially challenging since one cannot rely on the conventional jet-instability-based atomization approach. Using the developed atomizer, successful ejection of representative fuels has been achieved at low flow rates and input power. Figure 6.1a provides a still image of methanol atomization from an ejector array of 11.8 μm nozzle orifices with microchannel nozzle terminations operating at a transducer driving frequency of 0.561 MHz. Figure 6.1b shows kerosene atomization from the same ejector array operating at 0.830 MHz. The results of the ANSYS

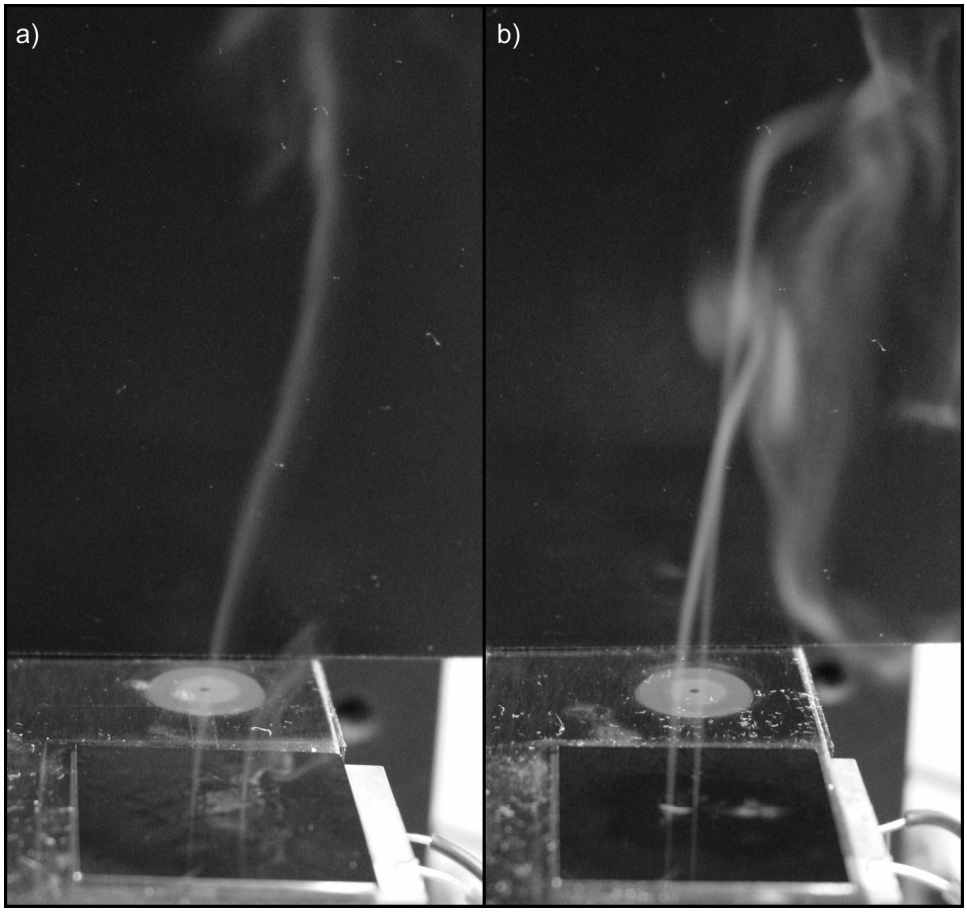

Figure 6.1. Methanol (a) and Kerosene (b) ejection by the micromachined ultrasonic atomizer with an array of 11.8 μm diameter orifices and microchannel-based nozzle terminations.

simulations using fuel properties do confirm that active ejectors are located near the middle of the ejector array where wave focusing is most efficient (as seen in Figures 6.1), and ejection does occur at the resonant frequencies predicted by ANSYS.

Successful atomization is obviously important for conversion of fuel from liquid to gas phase; however, ignition and combustion of a fuel-air mixture also require a high quality of atomization as indicated by the fineness of the spray and the droplet size distribution. Any suitable diameter can be used as a representative diameter of a spray, but the Sauter mean diameter has been shown to give the best indication of atomization quality.[107] In general, it has been found that large droplets (> 30 μm) inhibit flame

propagation, and suspensions of sub-10 μm diameter droplets burn like a gaseous fuel.[108,109] In order to determine the quality of the spray generated by the ultrasonic atomizer, droplet size distributions for water ejection from orifices ranging from 3.5 to 10 μm were measured using a laser diffraction instrument (Malvern Instruments, Spraytec Particle Analyzer with 0.1-2000 μm range). Table 6.1 summarizes the resulting parameters which determine the quality of the spray. In general, the Sauter mean diameter, $D_{3,2}$, is slightly smaller than the nominal orifice size of the ejector, d_o, and much smaller than most representative fuel droplet diameters (20–100 μm) for combustion studies reported in the literature.[108] The relative span factor, $\Delta = (D_{0.9} - D_{0.1})/D_{0.5}$, provides a direct indication of the range of drop sizes within a spray relative to the mass mean diameter, $D_{0.5}$.[108] Here, $D_{0.1}$ and $D_{0.9}$ are the diameters below which 10% and 90% by volume of the droplets in the spray are found, respectively. A narrow droplet size range is beneficial for combustion processes, and the relative span factor usually lies

Table 6.1. Atomization parameters resulting from the droplet size distribution measurements of water ejection from nozzle orifices ranging from 3.5 to 10 μm. Representative diameters include the mass mean diameter $D_{0.5}$, the diameter $D_{0.9}$ below which 90% of the droplets are found, and the Sauter mean diameter $D_{3,2}$. The relative span factor, Δ, provides an indication of the range of drop sizes in the spray.

Nominal Orifice Size, d_o (μm)	$D_{0.1}$ (μm)	$D_{0.5}$ (μm)	$D_{0.9}$ (μm)	$D_{3,2}$ (μm)	Relative Span Factor, Δ
3.5	1.8	4.9	10.3	3.2	1.74
6	3.3	6.7	15.1	5.4	1.76
7	4.3	8.3	20.8	7.1	1.99
8	4.0	8.7	22.6	6.7	2.14
10	6.7	20.6	50.9	13.8	2.14

between 1 and 1.5 for traditional fuel atomization; however, due to the extremely small droplet diameters seen in the current study, the atomization appears to be of high quality even for the comparatively larger relative span factor values reported here.

6.2 Inhalation Delivery of the Measles Vaccine

A comprehensive review of measles vaccination delivery methods has indicated that aerosol inhalation exhibits the greatest potential of nonpercutaneous routes.[110] In fact, this method has been shown to generate serological responses that exceed those achieved by needle injection. Typical nebulizers used for inhalation are not well suited to large scale vaccination programs in undeveloped regions due to a lack of portability, and other common aerosol delivery devices, e.g., pressurized Metered Dose Inhalers (pMDI), are unable to produce the monodisperse droplets necessary for effective aerosol inhalation.

Based on World Health Organization (WHO) requirements for inhalation vaccination three requirements must be met for vaccine administration: (1) generating a large fraction (> 75% of particles by volume) of sub-5 μm diameter droplets, (2) generating highly uniform ejection from a large fraction of orifices on a given device in order to achieve a flow rate of greater than 0.3 cc/min (approximately 100 orifices with a 5 μm diameter are required for operation at 1.0 MHz), and (3) operating at a temperature of less than 50°C to ensure viability of the ejected measles vaccine.

Figure 6.2 provides the results of preliminary viability tests performed using an array of 8 μm diameter orifices with the microchannel nozzle termination. Although the droplet size is not small enough to meet the requirements stated above, the operation of

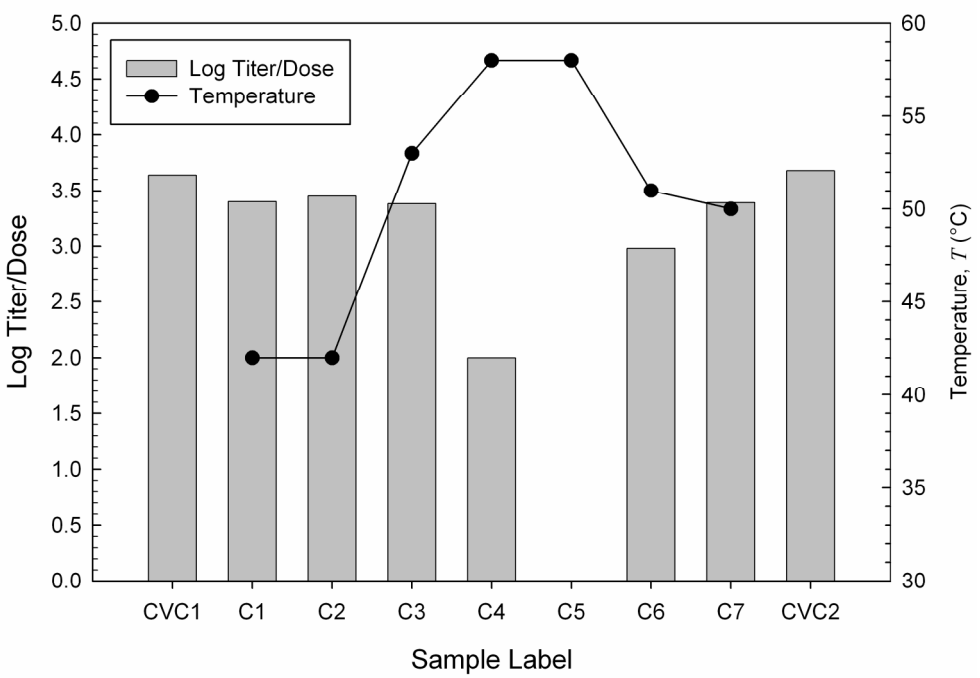

Figure 6.2. Viability of ejected measles vaccine as a function of operating temperature.

the device is not fundamentally different as the size of the orifice is decreased so successful ejection of live measles vaccine should be possible from smaller orifices. As shown in Fig. 6.2, the control samples CVC1 and CVC2 exhibited a potency of $10^{3.4}$ plaque forming units (pfu) per dose. The ejected virus exhibited a similar potency (10^3 pfu per dose) as long as the ejection temperature did not exceed 50°C.[111] The droplet size measurements reported in Section 6.1 indicate that ejection from 3.5 μm diameter orifices results in almost monodisperse 5 μm droplets. These results unambiguously indicate that the micromachined ultrasonic atomizer is capable of delivering aerosolized measles vaccine, while meeting the most stringent requirements on delivery efficacy (droplet size, distribution, and volume) as well as virus viability.

6.3 Ion Source for Bioanalytical Mass Spectrometry

Mass Spectrometry (MS) has become the technology of choice for accurate bioanalytical measurements, including protein identification. There is a strong momentum in the scientific community to develop miniaturized sample introduction platforms and lab-on-a-chip ion sources for proteomics because the samples available for analysis are frequently difficult to obtain and volumes very small. The main approaches using microfabrication techniques for electrospray (ESI) miniaturization can be broadly grouped as follows: (i) ESI devices incorporating fused silica capillary emitters,[112-114] (ii) devices that generate ESI from a microchannel exiting the blunt edge of a wafer,[115,116] and (iii) monolithic devices incorporating etched ESI tips.[117,118] Although some of these devices make use of highly innovative batch microfabrication processes reducing the ionization source manufacturing cost, they still rely on highly charged nozzles to create Taylor-cone electrospray. The micromachined ultrasonic atomizer platform investigated in this thesis has been applied as a high-throughput ion source for mass spectrometric analysis of biomolecules. Two key ideas lie in the foundation of this ion source: (1) to decouple aerosol formation from droplet charging, thereby providing a route for dramatic reduction of operating voltage and flexibility in the choice of solvent, enabling ultra-soft ionization and (2) to adopt a discrete (i.e., droplet-based) rather than continuous (i.e., jet-based) approach for controllable generation of charged droplets, thereby lowering the required sample size and improving sample utilization.

The ESI microarray has been interfaced with time-of-flight (TOF) (JEOL, Inc., model AccuTOF MS) and linear ion trap (Thermo Electron Corp., model Finnigan LTQ) mass spectrometers. As a first test, the standard calibration compound reserpine

(molecular weight 609.2 Da) in MeOH:H_2O:Acetic Acid (50:49.9:0.1 v/v) solution was successfully ionized repeatedly using the ultrasonic ejector/ion source. Ionization was achieved electrochemically by applying a DC bias electric potential to the piezoelectric transducer electrode facing the solution on top of the driving high frequency AC signal. Voltages in the range of 150 to 250 V were shown to be sufficient for ionization. This is an order of magnitude lower than the voltages required by conventional Taylor-cone-based electrospray sources, thus leading to ultra-soft ionization with little analyte fragmentation. Figure 6.3a shows a typical mass spectrum obtained after atomization with a strong and clear peak at 609.2 Da (197:1 signal-to-noise ratio) corresponding to the ^{12}C isotope of the reserpine ions followed by the least abundant carbon isotopes. Leucine Enkephalin (YGGFL) ($[M + H]^+$ = 556.67, $[2M + H]^+$ = 1111.09, $[3M + H]^+$ = 1665.73) in H_2O:Acetic Acid (99.9:0.1 v/v) solution has also been successfully ionized using the ultrasonic electrospray source and then detected by the linear ion trap MS. Interfacing between the ion source and mass spectrometer was made through a venturi device that focuses the ejected droplet streams emitted by the ejector array to the MS inlet enhancing sample transmission. Applied DC bias potential was ~100 V. The mass spectrum shown in Figure 6.3b indicates the presence of the YGGFL monomer (556.67), dimer (1111.09), and trimer (1665.73). These results clearly demonstrate the feasibility of the ultrasonic electrospray concept for low-voltage ionization of organic molecules and standard peptides (YGGFL).

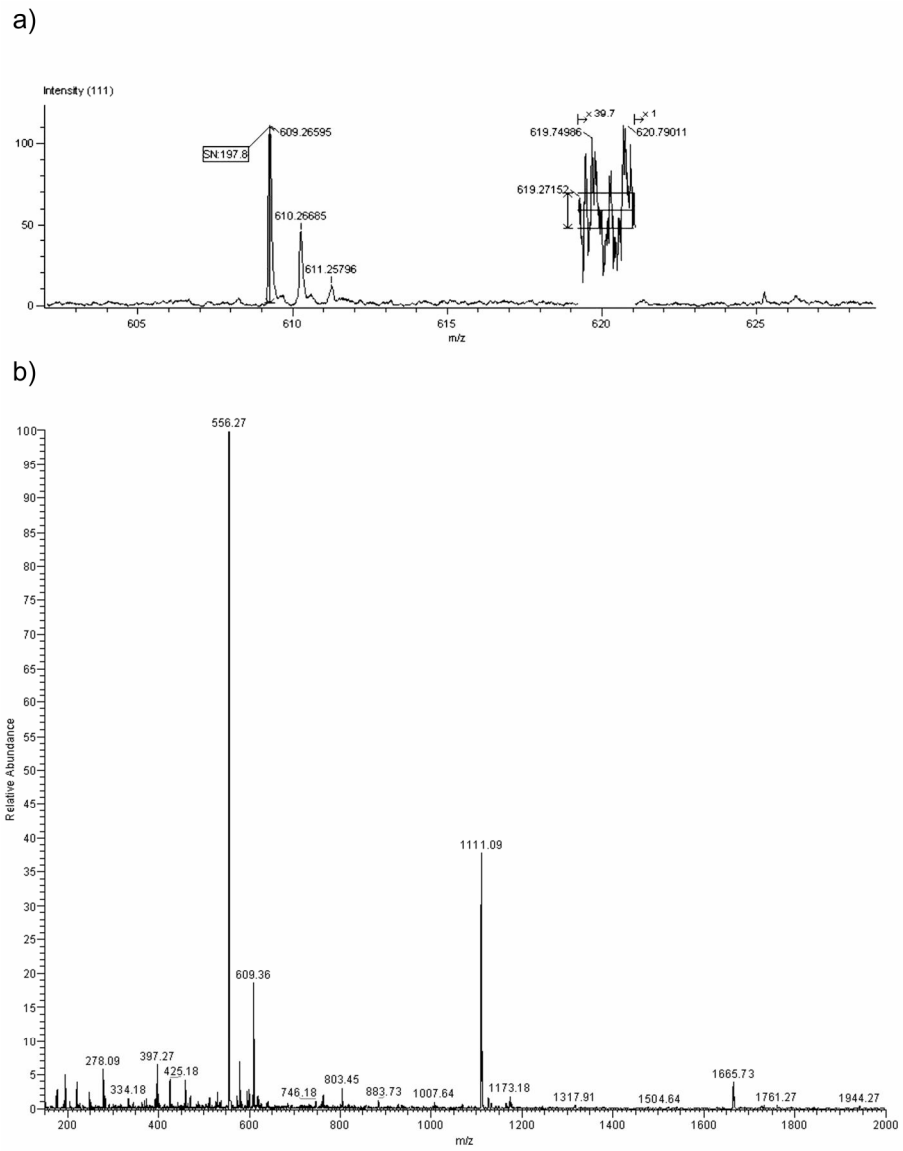

Figure 6.3. Mass Spectra (MS) obtained using the micromachined ultrasonic atomizer as an electrospray ion source: a) reserpine spectrum (MeOH:H_2O:Acetic Acid (50:49.9:0.1 v/v) solvent) and b) leucine enkephalin (YGGFL) spectrum (H_2O:Acetic Acid (99.9:0.1 v/v) solvent).

CHAPTER 7

CONCLUSIONS AND RECOMMENDATIONS FOR FUTURE WORK

This thesis presents the results of development and comprehensive investigation of a novel concept for ultrasonic atomization. The atomizer is a micro-electromechanical system (MEMS)-based device that exploits structural resonances and acoustic wave focusing by micromachined liquid horns to achieve fluid ejection and picoliter-scale droplet formation from a nozzle array over a broad range of flow rates and with low input power. Original contributions have been made in device design and fabrication (as described in Chapter 2) as well as acoustic and hydrodynamic characterization (Chapters 3 through 5) of device operation. The characterization efforts have been performed in concert with device development efforts, leading to an optimal design of the device, and include complimentary experimental and theoretical work. Successful operation of the ejector has been demonstrated for a number of working fluids (water, high viscosity mixtures of glycerol and water, and low surface tension methanol), but detailed performance characterization was limited to low viscosity, high surface tension liquids, using water as an important, broadly used, and representative example of these working fluids. Finally, the unique advantages enabled by the developed micromachined ultrasonic ejector are illustrated for challenging fluid atomization examples from a variety of applications, ranging from fuel processing on small scales to ultra-soft electrospray ionization of biomolecules for bioanalytical mass spectrometry.

The droplet generation concept introduced in Chapter 2 has been shown to address the challenges associated with conventional atomization techniques. This concept represents a flexible, low-cost platform for achieving low-power and low-temperature atomization of potentially any operating fluid. Despite demonstrated unique advantages of the developed atomizer concept, it has been found to be difficult to achieve reliable ejection of fluids with high viscosities and/or low surface tension, which presents unique challenges that provide a fruitful ground for future research. Achieving a high degree of control of the atomization of these fluids may require refinement of the ejector design. In particular, investigation of the following device modifications is recommended for future research:

1. *Effect of the Ejector Surface/Material Properties on Ejection of Low Surface Tension Liquids*: It has been found that ejection of low surface tension liquids is highly unstable, and they tend to weep from the nozzle orifices and also cover the front surface of the device with a thin liquid film that is detrimental to ejection. Preliminary attempts to address this issue by modifying the surface properties of the ejector, e.g., coating the top surface with a hydrophobic material (Parylene C), have been only partially successful. The observation of the ejection phenomena and experience with device operation suggest that it may be desirable to have a wetting (fluid-philic) surface within the nozzle (i.e., inside of the ejector) to avoid gas bubble formation and a non-wetting (fluid-phobic) surface on the front side (i.e., outside of the ejector) to prevent formation of blocking liquid film. Careful experimental and theoretical investigation of related fluid mechanics issues would be of significant value to refining ejector design and fabrication, which needs to

be complemented with analysis of manufacturing issues associated with the choice and method of application of various coatings with desired surface properties.

2. *Effect of the Ejector Structural Design on Ejection of Low Surface Tension Liquids*: If weeping cannot be controlled by modifying the surface properties alone, it may be necessary to change the physical design of the nozzle orifice. For example, other researchers have indicated that fabrication of a ring-shaped lip around the periphery of the orifice helps to minimize weeping of low surface tension ejection fluids.[12] This would require a significant modification of the current fabrication procedure, which could have implications on the ejection of other fluids (e.g., those with a high viscosity). Thus development of simple and robust micromachining approaches to maintain the "ease of manufacturability" advantage of the developed ejector concept is needed, as well as fundamental understanding of the fluid physics underlying ejection from corrugated orifices to support optimal ejector orifice design.

3. *Effect of the Ejector Orifice on Ejection of High Viscosity Liquids*: Ejection of high viscosity liquids by the ejector with a microchannel at the nozzle apex requires generation of a larger pressure gradient near the nozzle tip to overcome significant viscous losses at the orifice. As a result, such devices must be driven at higher power input levels and are therefore prone to measurable, and often detrimental, heating. The input power requirement is reduced for operation of devices with orifices in thin nitride membranes; however, membrane-based devices are not as robust leading to an increase in the likelihood of device failure

due to membranes breaking during operation. It is recommended that this design-for-manufacturability issue be investigated further to determine the best compromise between device robustness, power consumption, and simplicity of fabrication.

4. *Effect of the Nozzle Shape on Acoustic Focusing*: As has been discussed, the pyramidal nozzle shape was selected because it is easily created via a single step anisotropic wet etch of (100) oriented single crystal silicon. This does not mean that this shape is optimal for acoustic wave focusing. Therefore, it is recommended that an investigation into the use of other microfabrication methods (e.g., stamping in aluminum or injection molding in plastic followed by coating with an appropriate high impedance material) that may be capable of making nozzles of more complex shapes for focusing be conducted.

The experimentally-validated finite element analysis (FEA) simulations of the acoustical response of the system presented in Chapter 3 have been shown to predict the cavity resonant frequencies for efficient device operation and confirm the acoustic wave focusing within the pyramidal nozzles (liquid horns) for a variety of device geometries and working fluids. It is not anticipated that the trends in the acoustical response of the system will change significantly for typical operating fluids; however, these simulations are based on the assumption that the acoustic disturbances generate only small-amplitude perturbations of the ambient state of the fluid within the chamber, and therefore nonlinear terms are dropped from the equations governing the acoustic response. In addition, the FEA simulations neglect or incorrectly account for other important aspects of the acoustic

actuation (e.g., frictional losses in the fluid and heat generation in the piezoelectric transducer). Therefore, the following studies are recommended for future research:

1. Further study of the limits of validity of the approximations and methods used to investigate the acoustic response of the system should be conducted. This includes an evaluation of the linear approximation of the acoustic equations with respect to fluid properties, geometry of the device, amplitude of the acoustic pressure, and frequency of operation. A more accurate account of losses within the fluid should also be included in the model, and a non-isothermal analysis of the fluid heating near the ejection point is of considerable interest due to the implications of changing fluid properties, with increasing temperature, on the ejection process.
2. In addition to determining the validity of the methods used to model the acoustic response within the fluid chamber, an investigation of ohmic heat generation due to the oscillation of the piezoelectric transducer is also recommended.
3. In conjunction with the investigation of micromachining techniques capable of producing nozzles with more complex geometries, simulations of liquid horns of different geometries should be conducted to determine which horn shapes produce the greatest focusing.

In chapter 4, a complimentary experimental and theoretical investigation of the fundamental physics governing the fluid ejection has been presented. A conceptual description of the ejection process has been developed and used as the framework for the analysis of the relevant time scales, based on the premise that it is the relationship between the acoustic pumping frequency (process time scale t_f) and surface tension

(capillary time scale t_σ) that prescribes the mode of ejection (discrete-droplet vs. continuous-jet). An extensive range of experimental conditions was investigated in the limits of two available device geometries and the use of water as the working fluid. A scaling analysis of the key fluid mechanics phenomena was shown to be supported by the experimental data and yielded a set of simple laws that enable accurate definition of under what conditions ejection is possible and what controls the mode (discrete-droplet vs. continuous-jet) of ejection. However, it has been shown that even for ejection of water from smaller, sub-5 μm diameter orifices, the viscous effects also become important setting the limit on the validity of the scaling laws developed in this thesis. To this end, the following studies are recommended for future research:

1. From the scaling analysis it is expected that as the radius of the orifice decreases, viscous effects should become important ($t_\mu \sim r_o^2$) and must enter into consideration when deciding what controls the mode of ejection; however, since transition behavior was not observed for the smallest orifice diameter (d_o = 4.5 μm), it is not possible to evaluate the validity of this statement with the experimental data reported in this thesis. Additional experiments should be conducted on sub-5 μm diameter orifices at higher operating frequencies (> 2.5 MHz) to determine the conditions for the transition from discrete-droplet to continuous-jet mode operation, and thus to provide experimental guidelines on the validity limit of the scaling laws developed in this thesis.
2. The importance of viscous effects should also increase if a higher viscosity fluid is employed ($t_\mu \sim \mu^{-1}$). Therefore, careful visualization of ejection of higher

viscosity water-glycerol mixtures from sub-5 μm to 20 μm diameter orifices over the frequency range of interest (0.5–3 MHz) should be conducted.

3. Since the surface tension of the liquid has a significant effect on the operating frequency at which the transition from discrete-droplet to continuous-jet mode of ejection occurs (i.e., $t_\sigma = (\rho r_o^3/\sigma)^{1/2}$, and transition behavior is found to occur when $t_\sigma \sim t_f$), it is also recommended that further visualization experiments be performed with lower surface tension liquids such as methanol or kerosene.

4. And, finally, the outcomes of the experimental investigations proposed in bulleted items 1 through 3 above should be supplemented by the appropriate revisions and extension, if needed, of the scaling analysis and development of modified ejection regime maps that could be applicable for a broader range of operating conditions.

In chapter 5, the conceptual description of the ejection process introduced in Chapter 4 as well as the scaling laws were confirmed using experimentally-validated computational fluid dynamics (CFD) simulations of the interface evolution during fluid ejection. These simulations also enable "virtual" experiments to be conducted over a wide (potentially any) range of conditions (e.g., fluid properties and device geometries) within the limits of validity of the governing transport equations. This enabled simulation of ejection from the smallest diameter (3 and 5 μm) orifices under investigation to check the limits of validity of the scaling laws developed in Chapter 4 as the viscous effects become comparable to surface tension. Following careful experimental validation of the simulation method on relevant benchmark ejection cases, it is easier to investigate the effect of changing fluid properties and geometry on the ejection process by performing

virtual experiments than to investigate the large number of actual experimental cases. Therefore, the following studies are recommended for future research:

1. Based on the scanning electron microscope (SEM) images of the nozzle and orifice structure and geometry, the simulation domain could be modified to more accurately represent the shape of the nozzles and of the ejection orifices (i.e., the nozzles should be treated as pyramidal in shape, and not conical as has been done in this thesis, and the orifice of the membrane devices is a cylinder with tapered, not straight walls). This would demand, however, use of fully three-dimensional (3-D) simulations which can be highly computationally intensive. This should be combined with numerical investigation of a broader range of variation in possible dimensions (i.e., size of the orifice, including sub-5 μm diameter orifices operating at higher operating frequencies (> 2.5 MHz), and nozzle and orifice geometries) beyond what has been investigated in this thesis to provide a roadmap for development of an "optimal ejector" from the fluid mechanics prospective.
2. The effect of varying thermophysical and transport properties of the working fluid (i.e., considering high viscosity and lower surface tension fluids) should be extensively investigated to understand the basic physics of the ultrasonic atomization of such fluids using acoustic horns, as well as to provide guidance on the optimal operating conditions of the device. This includes simulation-driven development of the scaling laws for limiting transport processes (different in different cases), leading to simple "algebraic" operation rules in terms of relevant dimensionless numbers.

3. In addition to conducting virtual experiments with varying surface tension of the working fluid, it is also recommended that the effect of surface properties of the nozzle plate (i.e., fluid-phobic vs. fluid-philic behavior modification enabled by surface coating) on the ejection be investigated numerically, by modifying the contact angle/line dynamics in the FLUENT solver. This would be instrumental for development of an ejector capable of stable operation with low surface tension fluids.
4. In conjunction with the investigation of viscous fluid heating near the ejection point, this effect should be introduced into the fluid-mechanics problem via coupled thermal-fluid simulations.

In Chapter 6, the micromachined ultrasonic atomizer was shown to be well-suited for atomization of fuels for small-scale, portable fuel processors, aerosolization of measles vaccine for inhalation delivery, and ultra-soft ionization of biomolecules for mass spectrometry. Each of these applications relies on the unique combination of attributes of the droplet generation concept under investigation in this thesis. The ability to produce a high-quality fuel spray at low flow rates and with low power consumption is advantageous for small-scale fuel processing applications,[17] generation of monodisperse sub-5 μm droplets at low temperatures is required for oral delivery of biological fluids, and the capability for ultra-soft ionization by decoupling the aerosol formation and droplet charging,[14] yet achieving both operations in a single device, yields a dramatic improvement over traditional mass spectrometer interfaces.

The three applications described in Chapter 6 demonstrate the breadth of applications of the micromachined ultrasonic atomizer, but as discussed in Chapter 1, this technology can be utilized in any application that requires the production of monodisperse droplets using a repeatable and reliable process. As the ejection process becomes better characterized for atomization of higher viscosity liquids, a variety of applications ranging from manufacture of multilayer parts and circuits to deposition of polymers and photoresist without spinning should be investigated. Finally, cooling of microelectronics using direct jet (or droplet stream) impingement from an ejector array would allow for uniform cooling of a chip surface, while the possibility for individual activation of single ejector orifices would enable highly localized cooling of hotspots on a chip with nonuniform heat generation.

APPENDIX A

MATERIAL PROPERTIES USED IN THE ANSYS SIMULATIONS

The material properties needed to model the piezoelectric transducer, ejection fluid, and structural solids (silicon and silicon nitride) are found in Tables A.1 to A.3. Note that although the elastic and piezoelectric constants for lead zirconate titanate (PZT-8) piezoelectric material were obtained from APC International, Ltd.,[35] these parameters were adjusted slightly so that the electrical input impedance response of the two-dimensional simulation better matched that determined experimentally.

Table A.1. Properties that are used to model lead zirconate titanate (PZT-8) in the ANSYS simulations.[35]

Material	Property	Value
PZT-8	Young's modulus in the unpolarized direction, E_p	9.00×10^{10} N/m^2
	Young's modulus in the polarized direction, E_z	8.64×10^{10} N/m^2
	Poisson's ratio (unpolarized/polarized), ν_p	0.333
	Poisson's ratio (polarized/unpolarized), ν_{zp}	0.345
	Shear modulus in the polarized direction, G_{zp}	1.57×10^{10} N/m^2
	Mass density, ρ	7600 kg/m^3
	Piezoelectric constant relating voltage applied in the polarized direction to strain in the polarized direction, d_{33}	215×10^{-12} m/V
	Piezoelectric constant relating voltage applied in the polarized direction to strain in the unpolarized direction, d_{31}	-95×10^{-12} m/V
	Piezoelectric constant relating voltage applied in the unpolarized direction to the generated shear stress, d_{15}	330×10^{-12} m/V
	Relative permittivity in the unpolarized direction, $\varepsilon_{r,p}$	1290
	Relative permittivity in the polarized direction, $\varepsilon_{r,z}$	1000
	Damping Coefficient, γ	1×10^{-9}

Table A.2. Properties that are used to model the fluids in the ANSYS simulations.[38-42]

Material	Property	Value
Water	Mass density, $\rho_{o,water}$	1000 kg/m^3
	Speed of sound, c_{water}	1500 m/s
	Dynamic viscosity, μ_{water}	1.00x10^{-3} kg/m-s
Methanol	Mass density, $\rho_{o,MeOH}$	787 kg/m^3
	Speed of sound, c_{MeOH}	1089 m/s
	Dynamic viscosity, μ_{MeOH}	5.50x10^{-4} kg/m-s
Kerosene	Mass density, $\rho_{o,kerosene}$	820 kg/m^3
	Speed of sound, $c_{kerosene}$	1325 m/s
	Dynamic viscosity, $\mu_{kerosene}$	2.20x10^{-3} kg/m-s

Table A.3. Properties that are used to model the silicon and silicon nitride (Si_3N_4) in the ANSYS simulations.[33]

Material	Property	Value
Silicon	Young's Modulus, E_{Si}	150x10^9 N/m^2
	Poisson's ratio, ν_{Si}	0.21
	Mass Density, ρ_{Si}	2330 kg/m^3
	Damping Coefficient, γ_{Si}	6x10^{-9}
Si_3N_4	Young's Modulus, $E_{nitride}$	270x10^9 N/m^2
	Poisson's ratio, $\nu_{nitride}$	0.27
	Mass Density, $\rho_{nitride}$	2800 kg/m^3
	Damping Coefficient, $\gamma_{nitride}$	6x10^{-9}

APPENDIX B

TECHNICAL DETAILS OF THE SIMULATIONS PERFORMED IN ANSYS

Additional details of the implementation of the harmonic response analysis of the ejector assembly performed in ANSYS are provided here.

Modeling the Piezoelectric Transducer

ANSYS solves the constitutive equations[37] governing the piezoelectric behavior in the stress-charge form (as opposed to the strain-charge form discussed in Chapter 3) expressed as

$$\mathbf{T} = \mathbf{c_E} \cdot \mathbf{S} - \mathbf{e}^t \cdot \mathbf{E} \text{ and} \tag{B.1}$$

$$\mathbf{D} = \mathbf{e} \cdot \mathbf{S} + \boldsymbol{\varepsilon}_\mathbf{S} \cdot \mathbf{E}. \tag{B.2}$$

Therefore, the following matrix transformations are needed to convert the compliance matrix $\mathbf{s_E}$ found in Equation (1) of Chapter 3 to the elasticity (elastic stiffness) matrix $\mathbf{c_E}$ found in Equation (B.1) and the piezoelectric strain matrix **d** found in Equation (2) of Chapter 3 to the stress matrix **e** found in Equation (B.2):

$$\mathbf{c_E} = \mathbf{s_E^{-1}} \text{ and} \tag{B.3}$$

$$\mathbf{e} = \mathbf{d} \cdot \mathbf{s}_E^{-1}. \tag{B.4}$$

Additional matrix manipulations are required due to the ordering scheme used by ANSYS. The published data for the piezoelectric stress matrix **e** and stiffness matrix $\mathbf{c_E}$ are ordered x, y, z, yz, xz, xy;[35] however, the ANSYS input order is x, y, z, xy, yz, xz.[36] Therefore, rows and columns 4, 5, and 6 must be reordered to 6, 4, and 5. ANSYS

requires that two-dimensional simulations be modeled in the x-y plane (in this case, the piezoelectric transducer is polarized in the y-direction), but the matrices provided by Equations (B.3) and (B.4) are for a material polarized in the z-direction. Therefore, the second and third rows and fourth and sixth rows of both the piezoelectric stress and stiffness matrices must be interchanged. For the stiffness matrix, the second and third columns and fourth and sixth columns are also switched; however, for the piezoelectric stress matrix, only the second and third columns need to be interchanged.

Modeling the Fluid

As discussed in Chapter 3, the fluid is modeled using two-dimensional FLUID29 or FLUID30 acoustic fluid elements. A key option (KEYOPT (2) = 0) is used to specify the presence of a structure next to the fluid so that both the bulk fluid and the fluid located near an interface can be modeled using FLUID29 or FLUID30 elements. Even though the element type definitions allow the presence of a fluid-structure interface to be taken into account, the lines or surfaces corresponding to the interface between the fluid and the structures are flagged so that ANSYS includes the appropriate terms in the analysis.

APPENDIX C

COMPARISON OF PREDICTED AND MEASURED ELECTRICAL INPUT IMPEDANCE OF AN UNLOADED DEVICE

Figures C.1 and C.2 show the measured and predicted electrical input impedance of an unloaded device consisting of a 1 mm thick, 24x28 mm piezoelectric PZT-8 transducer, a 495 μm thick, 24x24 mm silicon ejector plate containing a 20x20 array of nozzles with 5 μm orifices, and a fluid reservoir bounded by a 630 μm thick, 24 mm wide spacer with a 2 mm wide sidewall. The two-dimensional (2-D) domain used to model this device comprises a 1 mm thick, 24 mm wide transducer, a 495 μm thick silicon ejector

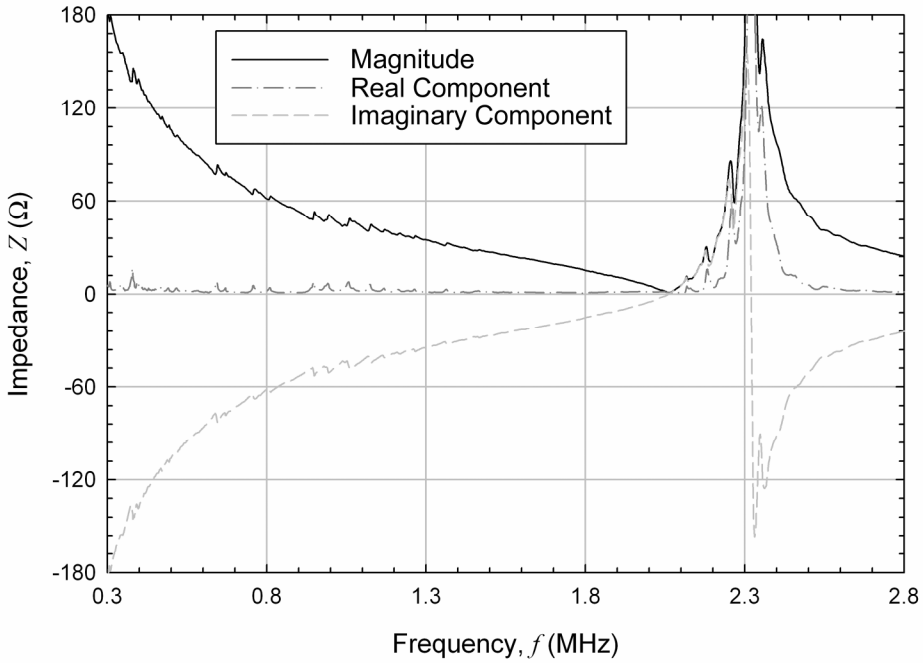

Figure C.1. Experimentally-measured electrical input impedance as a function of driving transducer frequency for a 1 mm thick lead zirconate titanate (PZT-8) piezoelectric transducer driving an unloaded device with a 495 μm thick silicon ejector plate and a 630 μm thick spacer.

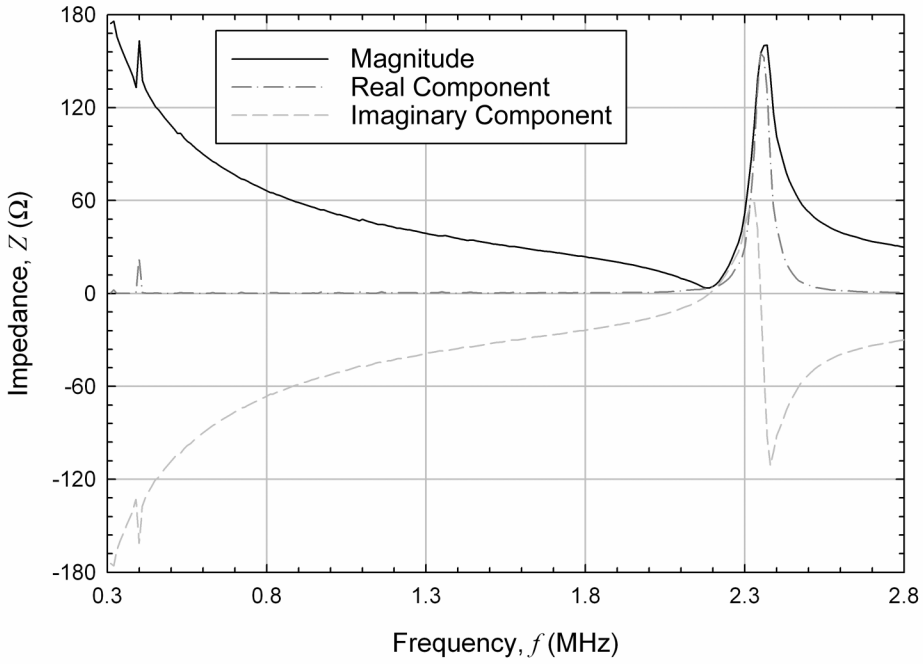

Figure C.2. Predicted electrical input impedance as a function of driving transducer frequency for a 1 mm thick lead zirconate titanate (PZT-8) piezoelectric transducer driving an unloaded device with a 495 μm thick silicon ejector plate and a 630 μm thick spacer.

plate containing an array of 15 nozzles with 5 μm orifices, and a 630 μm thick, 24 mm wide spacer with a 2 mm wide sidewall. The base of the nozzles is 720 μm wide, which yields 13 μm wide, 2 μm thick nitride membranes at the nozzle tips.

Although the acoustic response of the actual device is not as clean as that of the simulated device, the simulations match the measurements very well. The longitudinal resonance of the piezoelectric transducer is predicted to be at a slightly higher frequency (f = 2.35 MHz) than the measurement value (f = 2.32 MHz); however, this could easily be due to slight differences between the model and the geometry of the actual device. Figures C.1 and C.2, along with Figures 3.3 and 3.4 of Chapter 3, validate the use of the ANSYS model to predict the behavior of the ultrasonic atomizer under investigation in this thesis.

APPENDIX D

EFFECT OF THE NOZZLE TERMINATION (SHORT CHANNEL VS. THIN MEMBRANE) ON THE ACOUSTICAL RESPONSE OF THE DEVICE

Figures D.1 and D.2 show the electrical input impedance as a function of frequency for a two-dimensional (2-D) computational domain comprising a 1 mm thick, 24 mm wide piezoelectric PZT-8 transducer, a 500 μm thick silicon ejector plate containing 15 nozzles, and a fluid reservoir bounded by a 500 μm thick, 24 mm wide

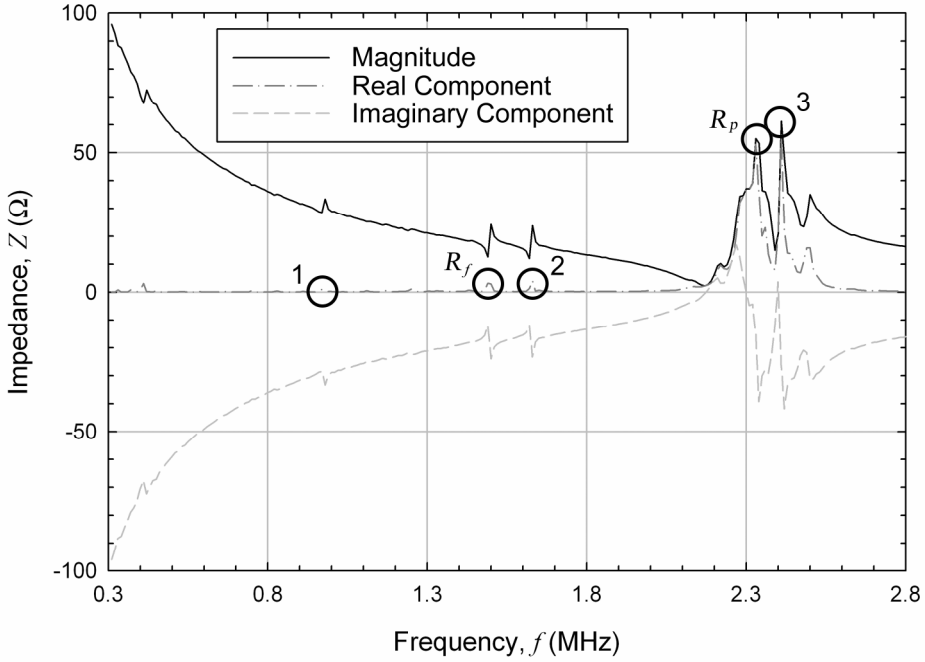

Figure D.1. Predicted electrical input impedance as a function of driving transducer frequency for a 1 mm thick lead zirconate titanate (PZT-8) piezoelectric transducer driving a water-loaded device with a 500 μm thick silicon ejector plate and a 500 μm thick spacer. The device nozzles terminate in 40 μm wide, 2 μm thick nitride membranes. The first three resonant modes corresponding to acoustic wave focusing and the longitudinal resonance of the piezoelectric are highlighted.

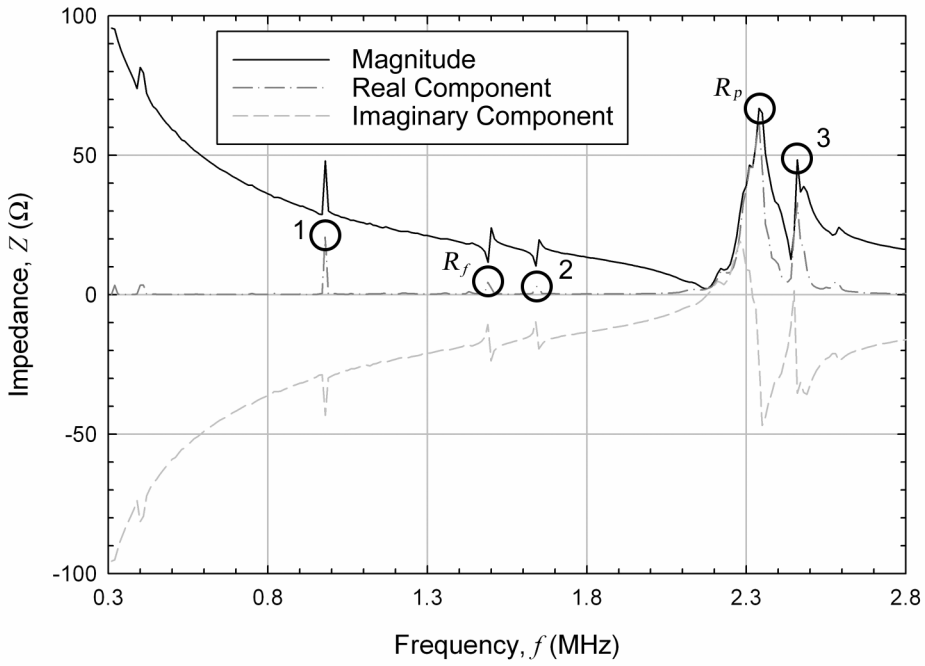

Figure D.2. Predicted electrical input impedance as a function of driving transducer frequency for a 1 mm thick lead zirconate titanate (PZT-8) piezoelectric transducer driving a water-loaded device with a 500 μm thick silicon ejector plate and a 500 μm thick spacer. The device nozzles terminate in short 5 μm long, 5 μm wide channels. The first three resonant modes corresponding to acoustic wave focusing and the longitudinal resonance of the piezoelectric are highlighted.

spacer with a 2 mm wide sidewall. Figure D.1, which is identical to Figure 3.4 of Chapter 3 corresponds to a nozzle terminating in a 40 μm wide, 2 μm thick membrane, and Figure D.2 corresponds to a nozzle terminating in a short 5 μm long, 5 μm wide channel.

Figures D.1 and D.2 are almost identical. As expected, the longitudinal resonance of the piezoelectric transducer and the first resonance corresponding to a standing wave located between the piezoelectric transducer and the flat area of the ejector plate on the periphery of the device are unchanged. The cavity resonances highlighted in Figure D.2, corresponding to pressure wave focusing at the nozzle tips, are located at slightly higher frequencies than those in Figure D.1 because the focal point is shifted farther into the cavity, which effectively shortens the chamber centerline height h_c. This effect is not

significant; therefore, the simulations of either design are expected to yield similar results.

APPENDIX E

COMPARISON OF THE ELECTRICAL INPUT POWER AND POWER TRANSFERRED TO THE FLUID FOR ADDITIONAL DEVICE GEOMETRIES

Figure E.1 provide the electrical input power and the power imparted to the ejected fluid as functions of frequency for a two-dimensional (2-D) computational domain comprising a 2 mm thick, 24 mm wide piezoelectric PZT-8 transducer, a 500 μm thick silicon ejector plate containing 15 nozzles, and a fluid reservoir bounded by a 500 μm thick, 24 mm wide spacer with a 2 mm wide sidewall. Figure E.2 shows the same information for a 2-D domain with a 1 mm thick transducer and a 1.5 mm thick spacer. All other geometry is the same as for the device with the 2 mm thick piezoelectric transducer.

Due to the decreasing power input to the transducer, it appears that operation at the lower frequency modes of the system is desirable. Operation at the longitudinal resonance of the piezoelectric transducer imparts significant power to the ejected fluid, especially for the device geometry represented in Figure E.1; however, the device efficiency is poor at this frequency because amplification of the electrical current and physical displacement of the piezoelectric transducer at resonance leads to significantly increased resistive and frictional losses without the benefit of acoustic wave focusing to amplify the fluid velocity.

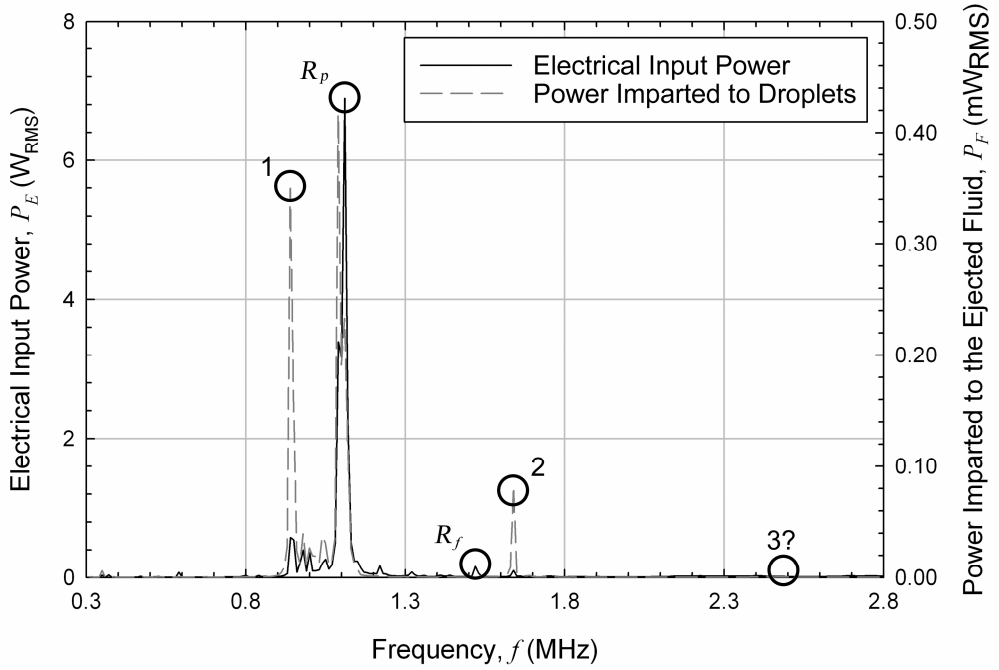

Figure E.1. Comparison of electrical input power with the power imparted to the ejected fluid as functions of driving transducer frequency for a 2 mm thick lead zirconate titanate (PZT-8) piezoelectric transducer driving a water-loaded device with a 500 μm thick silicon ejector plate and a 500 μm thick spacer. The first two resonant modes corresponding to acoustic wave focusing and the longitudinal resonance of the piezoelectric are highlighted.

In addition, negligible power transfer to the ejected droplets is observed for operation at resonant frequencies located far above the piezoelectric transducer resonance. The best performance (in terms of power transfer to the droplets) is seen at low frequency resonances that are significantly lower than that of the transducer (see resonance 2 in Figure E.2). Therefore, it is recommended that the droplet generator be designed with a thin enough piezoelectric transducer such that one of the device operating modes is at a much lower frequency than that of the piezoelectric longitudinal resonance.

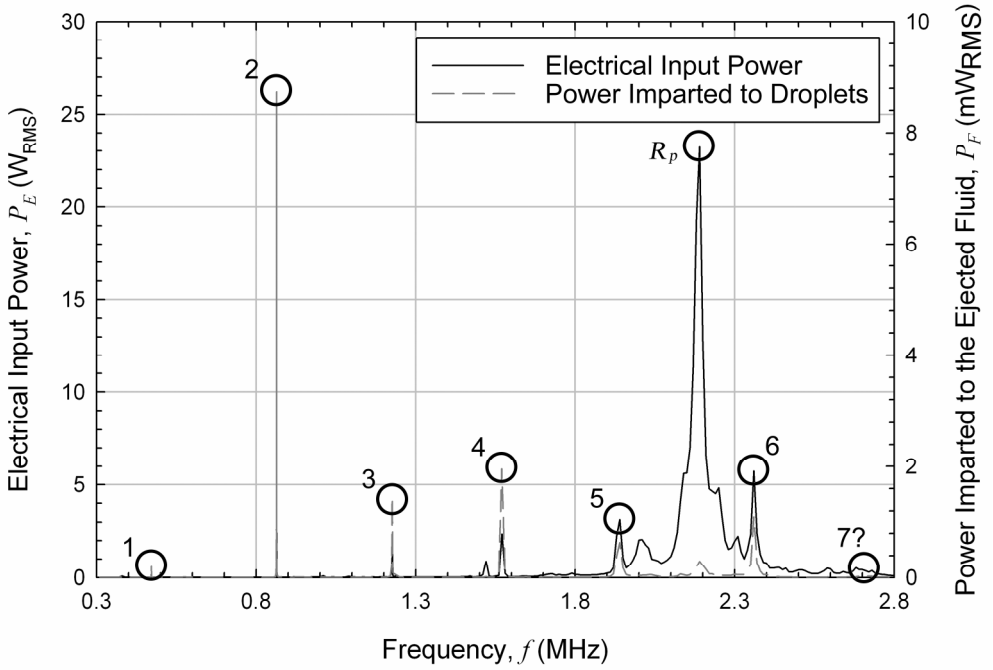

Figure E.2. Comparison of electrical input power with the power imparted to the ejected fluid as functions of driving transducer frequency for a 1 mm thick lead zirconate titanate (PZT-8) piezoelectric transducer driving a water-loaded device with a 500 μm thick silicon ejector plate and a 1.5 mm thick spacer. The first six resonant modes corresponding to acoustic wave focusing and the longitudinal resonance of the piezoelectric are highlighted.

APPENDIX F

TEST SECTION ASSEMBLY

Two different ejector fixtures have been used for image acquisition. Figure F.1 is a photograph of the original flow-through test section comprising a piezoelectric transducer, ejector plate, and Kapton® tape spacer mounted to a plastic base structure. The spacer is constructed of multiple layers of single- and double-stick Kapton® tape with adhesive top and bottom surfaces, a square 20x20 mm cutout for the fluid chamber, and channels cut into the middle Kapton® layer to serve as the inlet and outlet of the chamber. The piezoelectric transducer and ejector plate are mounted to the adhesive surfaces, and the ejector sandwich structure is mounted to the plastic base, which has a

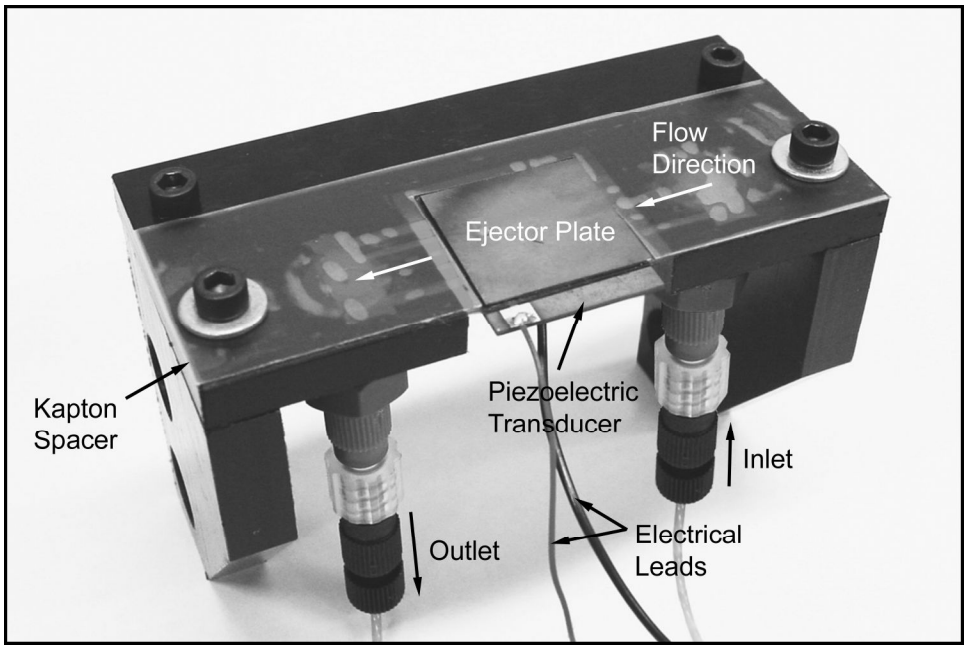

Figure F.1. Image of the original flow-through experimental fixture consisting of a piezoelectric transducer, ejector plate, and Kapton® tape spacer mounted to a plastic base structure.

cutout for the piezoelectric transducer. Therefore, the Kapton® tape not only serves as the spacer to dictate the fluid chamber height but it also supports the ejector assembly.

The flow-through test section is shown positioned in the experimental setup during visualization in Figure F.2. The microscope lens of the CCD camera is oriented at an angle to the surface of the ejector, and the LED array is positioned so that it provides backlighting to the ejected droplets/jets. The plastic base is attached to a three-axis stage that positions the ejector such that an active orifice is located in the field of view of the microscope lens.

A number of issues are associated with the use of the flow through experimental test section. Since the flexible Kapton® tape spacer acts as the support for the ejector assembly, the front edge of the sandwich structure sags during operation, which makes it

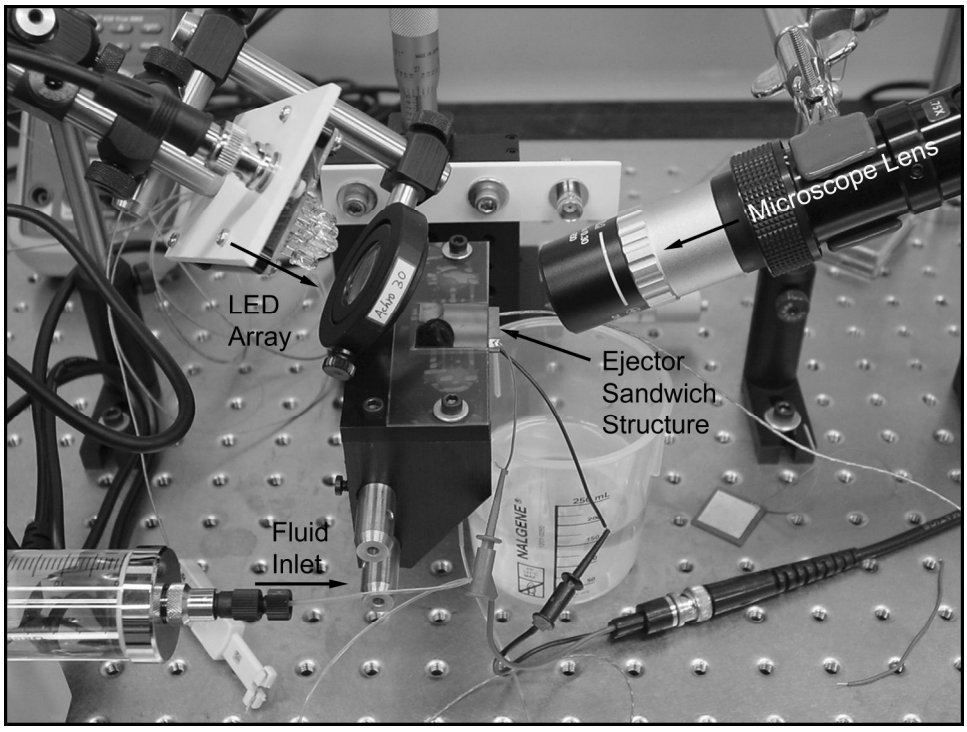

Figure F.2. Flow-through test section positioned in the experimental setup during visualization of the ejection process.

difficult to focus on an active orifice. In addition, the rough edges of the square fluid chamber cut out of the spacer trap air bubbles during operation leading to poor ejector performance. Although the Kapton® tape provides flexibility in making spacers of any thickness in 50 μm increments, spacers cannot be reused with different ejectors and piezoelectric transducers. Therefore, a new spacer must be made for each test condition, which is a time consuming process. With these issues in mind, a second test fixture was developed.

Figure F.3 provides images of the test fixture with and without the plastic housing clamped over the sandwich structure comprising the piezoelectric transducer, brass spacer, and ejector plate. An exploded schematic of the test section assembly is provided in Figure F.4. The design resembles a piston in a cylinder, which allows the test section to accommodate ejector assemblies with thicknesses of between 1 and 5 mm, and provides the flexibility to operate at a wide range of frequencies by increasing/decreasing the thickness of the piezoelectric transducer and spacer.

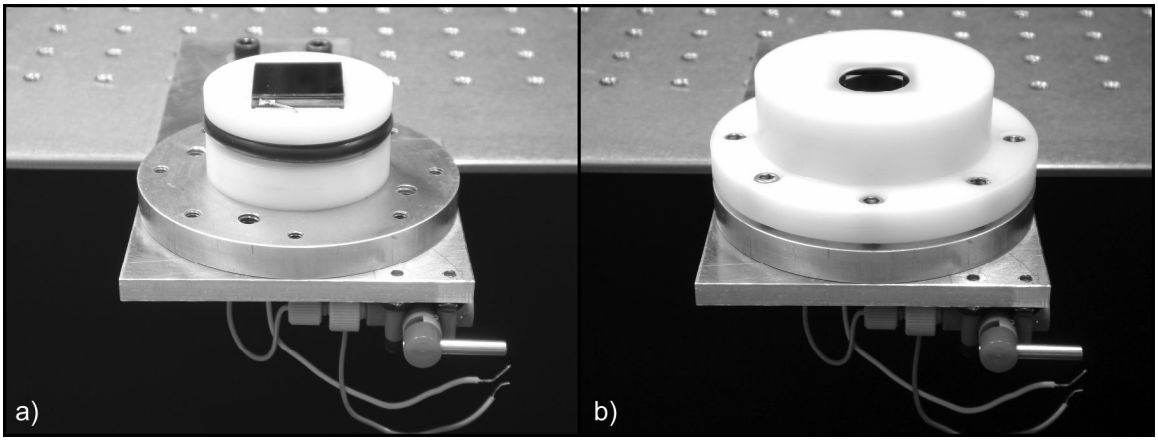

Figure F.3. Images of the test section: a) ejector sandwich structure comprising the piezoelectric transducer, silicon spacer, and ejector plate mounted on the plastic assembly base and b) complete test section assembly.

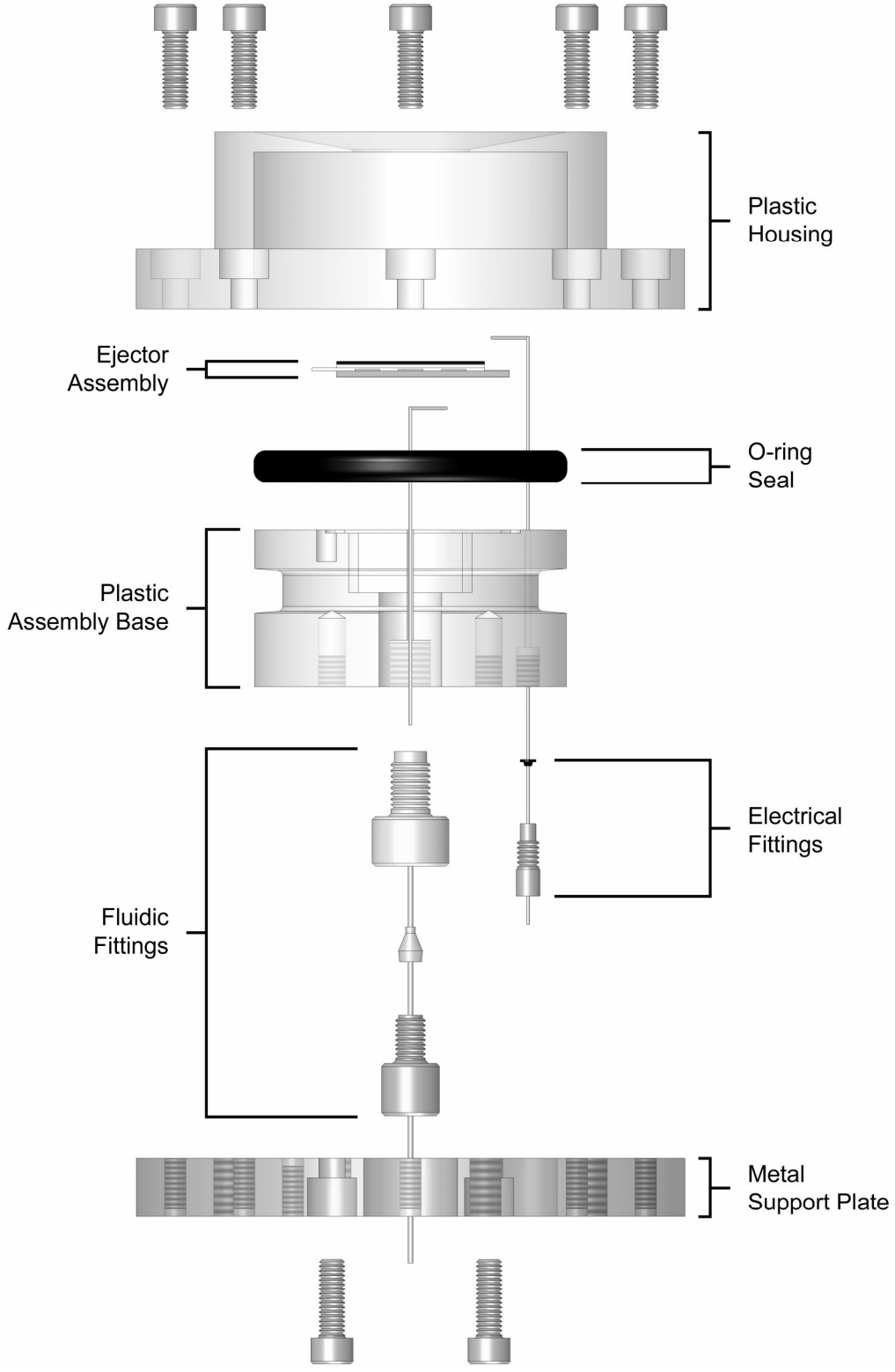

Figure F.4. Exploded schematic illustrating how the test section is assembled.

Figures F.3 and F.4 illustrate how the test section is assembled. The ejector sandwich structure is mounted to the plastic assembly base that serves as the piston. A small pocket machined out of the assembly base behind the transducer ensures that the motion of the piezoelectric transducer is not constrained. In addition, a hole connecting the bottom of the assembly base to the pocket behind the transducer allows an electrical lead to be connected to the back side of the piezoelectric transducer. The plastic housing is clamped over the entire assembly to form a small chamber around the ejector assembly that holds the ejection fluid during operation. The o-ring located between the plastic assembly base and housing prevents the chamber from leaking; the rubber gasket placed between the ejector assembly and the plastic housing also inhibits leakage, but more importantly, it cushions the ejector, which is easily broken during assembly. Two sets of fluidic fittings are secured to channels machined through the assembly base. The first set acts as the fluid inlet during device operation, and the other is used as a fluid outlet during filling of the device. A third set of fittings is used to seal around the electrical lead that is attached to the top side of the piezoelectric transducer within the fluid chamber. The entire test section assembly is mounted to an aluminum support plate, which is positioned on a three-axis stage so that the ejector can be moved to a desired location during visualization.

A cutaway schematic representing the ejector test section during device operation is shown in Figure F.5. The cross-sectional view clearly illustrates the piston-in-cylinder design. The pocket located behind the piezoelectric transducer and the electrical leads connected to the front and back sides of the transducer are visible. Figure 4.5 also shows

the fluid-loaded chamber surrounding the ejector sandwich structure along with the fluid inlet and outlet.

The assembled test fixture is shown in the experimental setup during visualization in Figure F.6. As seen in the figure, the microscope lens of the CCD camera is oriented at an angle of 20° to the surface of the ejector plate during image acquisition. The

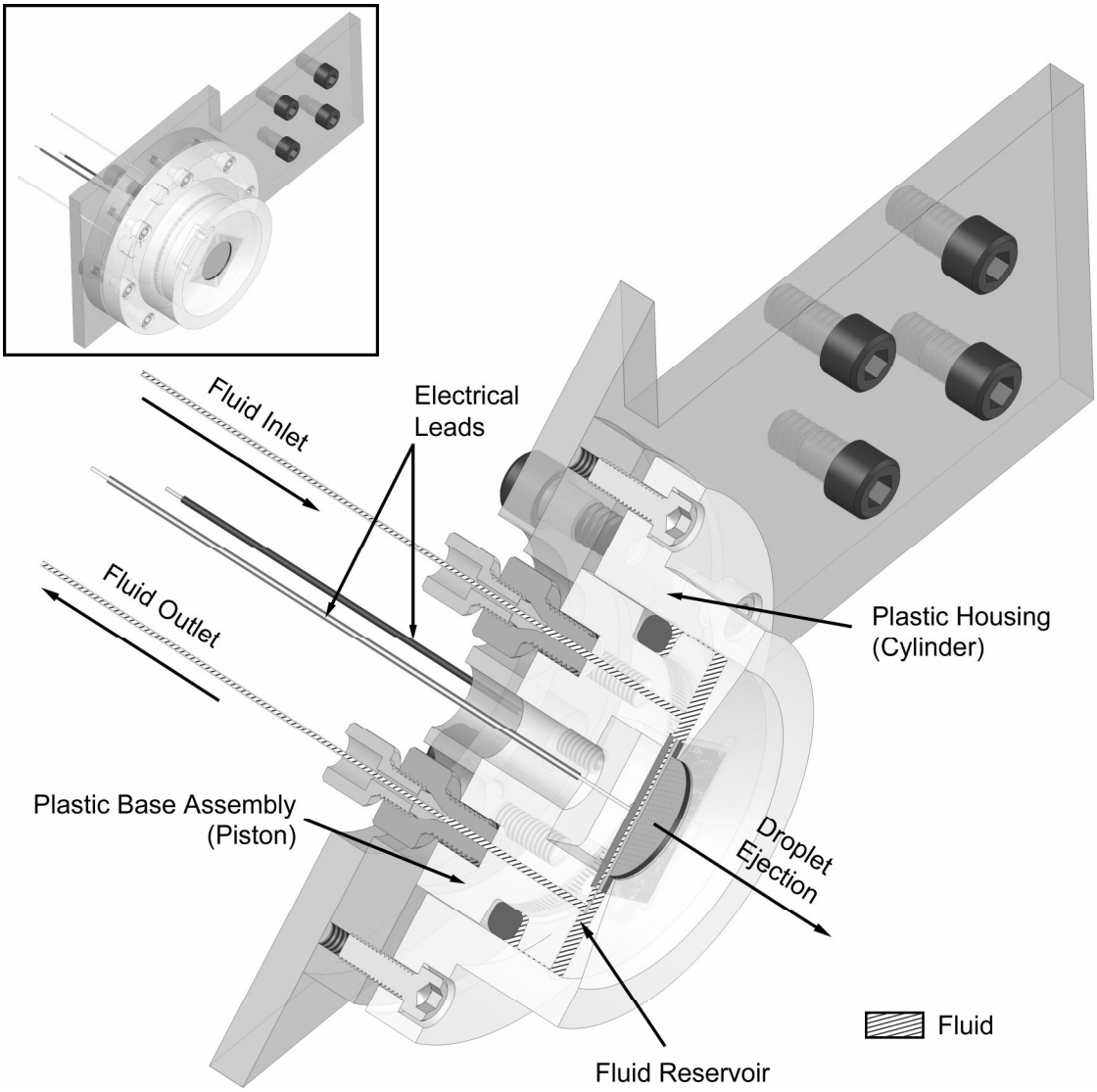

Figure F.5. Cutaway schematic showing the cross-sectional view of the test section assembly during operation.

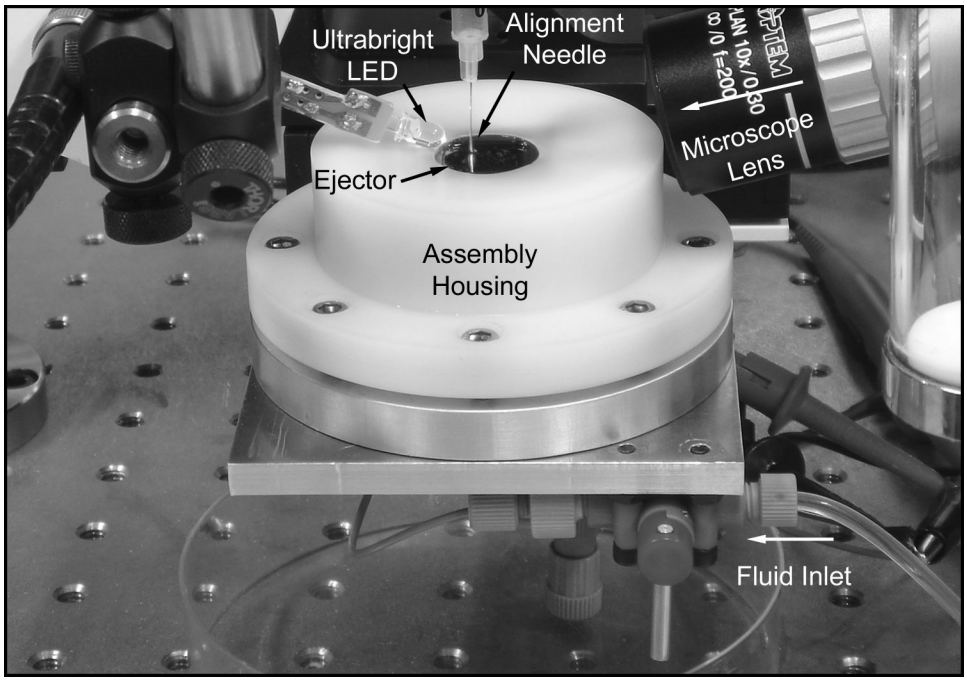

Figure F.6. Assembled test section positioned in the experimental setup.

ultrabright LED is positioned so that ejected droplets/jets are backlit. Even though ejection is easily seen with the naked eye, it is difficult to locate the exact position of an active orifice. The tip of the alignment needle is located at the focal point of the microscope lens so that if the stage is positioned to align an active orifice with this needle, the droplets/jets are easily found within the field of view of the microscope.

APPENDIX G

SPECIFICS OF THE FLUENT IMPLEMENTATION

Implementation of the volume of fluid (VOF) method in Fluent[72] requires careful consideration of how the selection of the primary and secondary phases will affect the problem setup and solution. Since the nozzle is initially filled with liquid, i.e., a liquid volume fraction of 1 is "patched" on the cells in the portion of the domain representing the nozzle, it is convenient to select the liquid as the secondary phase. The advection equation (Equation 19 of Chapter 5) then solves for the volume fraction C of the secondary (liquid) phase, and the primary (gas) phase volume fraction is found by subtracting computed values of C from 1. The momentum equation (Equation 21 of Chapter 5), which is dependent on the volume fraction of both phases through the volume-fraction-averaged density ρ and viscosity μ, is used to solve for the velocity field in both fluids. Specifically, Fluent[72] solves the governing equations (Equations (19)–(22) of Chapter 5) sequentially using a two-dimensional, double-precision segregated solver. The solution technique requires iteration of the following steps:

1. The current solution or the initial conditions are used to update the fluid properties.
2. The current values of the pressure are substituted into the momentum equation to solve for the updated velocity field.
3. The updated velocity field does not necessarily satisfy the continuity equation so a pressure-correction equation, which is derived from the continuity equation, is used to obtain corrections to the pressure and velocity fields and the face mass

fluxes. Fluent[72] recommends that the Pressure-Implicit with Splitting of Operators (PISO) pressure-velocity coupling scheme, which is based on the Semi-Implicit Method for Pressure-Linked Equations (SIMPLE) family of algorithms, be used for transient VOF problems.

4. The volume fraction advection equation is used to update the location of the interface between the liquid and gas. For transient VOF calculations, this equation is solved using an explicit time-marching scheme. Fluent automatically determines the time step used in the explicit scheme to ensure solution stability; however, adjustment of the maximum allowable Courant number near the interface can be used to influence the calculation of this time step. This Courant number is defined as the ratio of the time step to the characteristic time of transit for a fluid element across a control volume, which is equal to the volume of a cell divided by the sum of the outgoing fluxes.

5. The system of equations is checked for convergence, and if not achieved, the iterative process is repeated starting at step 1.

Fluent[72] makes several suggestions for improving the accuracy and convergence of VOF solutions. In addition to recommending that the PISO method be used for pressure-velocity coupling, it is also recommended that the PREssure STaggering Option (PRESTO!) pressure interpolation scheme be used to compute the cell face pressure. In general, the PISO algorithm allows all under-relaxation factors except for that for the pressure to be increased to 1 to increase the rate of convergence; however, for the VOF implementation discussed here, all under-relaxation factors except for that for momentum

are increased to 1, and the under-relaxation factor corresponding to momentum is set to 0.7.

REFERENCES

[1] H. P. Le, "Progress and trends in ink-jet printing technology," Journal of Imaging Science and Technology **42** (1), pp. 49-62 (1998).

[2] B. de Heij, B. van der Schoot, H. Bo, J. Hess, and N. F. de Rooij, "Characterization of a fL droplet generator for inhalation drug therapy," Sensors and Actuators A: Physical **85** (1), pp. 430-434 (2000).

[3] T. M. Crowder, M. D. Louey, V. V. Sethuraman, H. D. C. Smyth, and A. J. Hickey, "2001: An odyssey in inhaler formulation and design," Pharmaceutical Technology **25** (7), pp. 99-113 (2001).

[4] G. Perçin and B. T. Khuri-Yakub, "Piezoelectrically actuated flextensional micromachined ultrasound droplet ejectors," IEEE Transactions on Ultrasonics, Ferroelectrics, and Frequency Control **49** (6), pp. 756-766 (2002).

[5] S. Yuan, Z. Zhou, G. Wang, and C. Liu, "MEMS-based piezoelectric array microjet," Microelectronic Engineering **66** (1-4), pp. 767-772 (2003).

[6] S. Yuan, Z. Zhou, and G. Wang, "Experimental research on piezoelectric array microjet," Sensors and Actuators A: Physical **108** (1-3), pp. 182-186 (2003).

[7] A. Lozano, H. Amaveda, F. Barreras, X. Jordà, and M. Lozano, "High-frequency ultrasonic atomization with pulsed excitation," Journal of Fluids Engineering **125** (6), pp. 941-945 (2003).

[8] J. F. Banks, S. Shen, C. M. Whitehouse, and J. B. Fenn, "Ultrasonically assisted electrospray ionization for LC/MS determination of nucleosides from a transfer RNA digest," Analytical Chemistry **66** (3), pp. 406-414 (1994).

[9] J. F. Banks, J. P. Quinn, and C. M. Whitehouse, "LC/ESI-MS determination of proteins using conventional liquid chromatography and ultrasonically assisted electrospray," Analytical Chemistry **66** (21), pp. 3688-3695 (1994).

[10] D. B. Hager, N. J. Dovichi, J. Klassen, and P. Kebarle, "Droplet electrospray mass spectrometry," Analytical Chemistry **66** (22), pp. 3944-3949 (1994).

[11] L. He and K. K. Murray, "337 nm matrix-assisted laser desorption/ionization of single aerosol particles," Journal of Mass Spectrometry **34** (9), pp. 909-914 (1999).

[12] P. Luginbuhl, P.-F. Indermuhle, M.-A. Grétillat, F. Willemin, N. F. de Rooij, D. Gerber, G. Gervasio, J.-L. Vuilleumier, D. Twerenbold, M. Düggelin, D. Mathys, and R. Guggenheim, "Femtoliter injector for DNA mass spectrometry," Sensors and Actuators B: Chemical **63** (3), pp. 167-177 (2000).

[13] W. T. Berggren, M. S. Westphall, and L. M. Smith, "Single-pulse nanoelectrospray ionization," Analytical Chemistry **74** (14), pp. 3443-3448 (2002).

[14] S. Aderogba, J. M. Meacham, F. M. Fernandez, F. L. Degertekin, and A. G. Fedorov, "Nanoelectrospray ion generation for high-throughput mass spectrometry using a micromachined ultrasonic ejector array," Applied Physics Letters **86** (20), pp. 2031101-2031103 (2005).

[15] I. Ederer, J. Grasegger, and C. Tille, "Droplet generator with extraordinary high flow rate and wide operating range," Transducers '97, Proceedings of the 1997 International Conference on Solid-State Sensors and Actuators. Part 2 (of 2), Jun 16-19 1997, Chicago, IL, USA, pp. 809-812 (1997).

[16] I. Ederer, P. Raetsch, W. Schullerus, C. Tille, and U. Zech, "Piezoelectrically driven micropump for on-demand fuel-drop generation in an automobile heater with continuously adjustable power output," Sensors and Actuators A: Physical **62** (3), pp. 752-755 (1997).

[17] J. M. Meacham, M. J. Varady, D. Esposito, F. L. Degertekin, and A. G. Fedorov, "A micromachined ultrasonic atomizer for liquid fuels," Atomization and Sprays (submitted for review 2006).

[18] M. Orme, Q. Liu, and R. Smith, "Molten aluminum micro-droplet formation and deposition for advanced manufacturing applications," Aluminum Transactions Journal **3** (1), pp. 95-103 (2000).

[19] P. Calvert, "Inkjet printing for materials and devices," Chemistry of Materials **13** (10), pp. 3299-3305 (2001).

[20] W. S. Wong, S. Ready, R. Matusiak, S. D. White, J.-P. Lu, J. Ho, and R. A. Street, "Amorphous silicon thin-film transistors and arrays fabricated by jet printing," Applied Physics Letters **80** (4), pp. 610-612 (2002).

[21] G. Perçin, L. Levin, and B. T. Khuri-Yakub, "Piezoelectrically actuated droplet ejector," Review of Scientific Instruments **68** (12), pp. 4561-4563 (1997).

[22] G. Perçin, T. S. Lundgren, and B. T. Khuri-Yakub, "Controlled ink-jet printing and deposition of organic polymers and solid particles," Applied Physics Letters **73** (16), pp. 2375-2377 (1998).

[23] S.-C. Chang, J. Bharathan, and Y. Yang, "Dual-color polymer light-emitting pixels processed by hybrid inkjet printing," Applied Physics Letters **73** (18), pp. 2561-2563 (1998).

[24] G. Perçin and B. T. Khuri-Yakub, "Micromachined droplet ejector arrays for controlled ink-jet printing and deposition," Review of Scientific Instruments **73** (5), pp. 2193-2196 (2002).

[25] G. Perçin and B. T. Khuri-Yakub, "Piezoelectric droplet ejector for ink-jet printing of fluids and solid particles," Review of Scientific Instruments **74** (2), pp. 1120-1127 (2003).

[26] A. U. Chen and O. A. Basaran, "A new method for significantly reducing drop radius without reducing nozzle radius in drop-on-demand drop production," Physics of Fluids **14** (1), pp. L1-L4 (2002).

[27] C.-Y. Kung, M. D. Barnes, N. Lermer, W. B. Whitten, and J. M. Ramsey, "Single-molecule analysis of ultradilute solutions with guided streams of 1-μm water droplets," Applied Optics **38** (9), pp. 1481-1487 (1999).

[28] G. L. Switzer, "A versatile system for stable generation of uniform droplets," Review of Scientific Instruments **62** (11), pp. 2765-2771 (1991).

[29] S. I. Zoltan, United States Patent No. 3,683,212 (1972).

[30] G. Perçin, G. G. Yaralioglu, and B. T. Khuri-Yakub, "Micromachined droplet ejector arrays," Review of Scientific Instruments **73** (12), pp. 4385-4389 (2002).

[31] S. A. Elrod, B. Hadimioglu, B. T. Khuri-Yakub, E. G. Rawson, E. Richley, C. F. Quate, N. N. Mansour, and T. S. Lundgren, "Nozzleless droplet formation with focused acoustic beams," Journal of Applied Physics **65** (9), pp. 3441-3447 (1989).

[32] J. W. Kwon, Q. Zou, and E. S. Kim, "Directional ejection of liquid droplets through sectoring half-wave-band sources of self-focusing acoustic transducer," Proceedings of the IEEE Micro Electro Mechanical Systems (MEMS), Las Vegas, NV, pp. 121-124 (2002).

[33] M. J. Madou, *Fundamentals of Microfabrication* (CRC Press, LLC, Boca Raton, FL, USA, 2002), pp. 183-216.

[34] J. M. Meacham, C. Ejimofor, S. Kumar, F. L. Degertekin, and A. G. Fedorov, "Micromachined ultrasonic droplet generator based on a liquid horn structure," Review of Scientific Instruments **75** (5), pp. 1347-1352 (2004).

[35] APC International, Ltd., "Material properties of lead zirconate titanate (PZT-8) material 880," www.americanpiezo.com (2006).

[36] ANSYS, ANSYS Release 7.1 (ANSYS, Inc., Canonsburg, PA, USA, 2003).

[37] J. S. Yang, *An Introduction to the Theory of Piezoelectricity* (Springer, New York, NY, 2005).

[38] M. J. Assael and S. K. Polimatidou, "Measurements of the viscosity of alcohols in the temperature range 290-340 K at pressures up to 30 MPa," International Journal of Thermophysics **15** (1), pp. 95-107 (1994).

[39] W. E. Forsythe, *Smithsonian Physical Tables*, 9th rev. ed. (Knovel, Norwich, NY, 1954 (2003)).

[40] R. H. Perry and D. W. Green, *Perry's Chemical Engineers' Handbook*, 7th ed. (McGraw-Hill, New York, NY, 1997).

[41] F. Plantier, J. L. Daridon, and B. Lagourette, "Nonlinear parameter (B/A) measurements in methanol, 1-butanol and 1-octanol for different pressures and temperatures," Journal of Physics D: Applied Physics **35** (10), pp. 1063-1067 (2002).

[42] C. L. Yaws, *Yaws' Handbook of Thermodynamic and Physical Properties of Chemical Compounds: Physical, Thermodynamic, and Transport Properties for 5000 Organic Chemical Compounds* (Knovel, Norwich, NY, 2003).

[43] W. D. Pilkey, *Formulas for Stress, Strain, and Structural Matrices* (Wiley, New York, NY, 1994).

[44] G. Brenn and U. Lackermeier, "Drop formation from a vibrating orifice generator driven by modulated electrical signals," Physics of Fluids **9** (12), pp. 3658-3669 (1997).

[45] K. C. Chaudhary and T. Maxworthy, "Nonlinear capillary instability of a liquid jet, part 2. Experiments on jet behaviour before droplet formation," Journal of Fluid Mechanics **96**, pp. 275-286 (1980).

[46] M. Orme and E. P. Muntz, "New technique for producing highly uniform droplet streams over an extended range of disturbance wavenumbers," Review of Scientific Instruments **58** (2), pp. 279-284 (1987).

[47] J. Eggers, "Nonlinear dynamics and breakup of free-surface flows," Reviews of Modern Physics **69** (3), pp. 865-929 (1997).

[48] E. Mariotte, *Traité du movement des eaux et des autres corps fluides (Treatise on the motion of water and other fluids)* (E. Michallet, Paris, France, 1686).

[49] F. Savart, "Mémoire sur la constitution des veines liquids lancées par des orifices circulaires en mince paroi (Memoir on the constitution of liquid veins discharged through circular orifices in a thin wall)," Annales de Chimie **53**, pp. 337-386 (1833).

[50] J. Plateau, *Statique Expérimentale et Théorique des Liquides soumis aux seules Forces Moléculaires (Experimental and theoretical statics of fluids subject only to molecular forces)* (Gauthier Villars, Paris, France, 1873).

[51] G. Magnus, "Hydraulische undersuchungen (Hydraulic investigations, part I)," Poggend. Annal. **xcv**, pp. 1-59 (1855).

[52] G. Magnus, "Hydraulische undersuchungen (Hydraulic investigations, part II)," Poggend. Annal. **cvi**, pp. 1-32 (1859).

[53] L. J. W. S. Rayleigh, "On the capillary phenomena of jets," Proceedings of the Royal Society of London **29**, pp. 71-97 (1879).

[54] L. J. W. S. Rayleigh, "Further observations upon liquid jets, in continuation of those recorded in the Royal Society's 'Proceedings' for March and May 1879," Proceedings of the Royal Society of London, **34**, pp. 130-145 (1882).

[55] L. J. W. S. Rayleigh, "Some applications of photography," Nature (London) **44**, pp. 249-254 (1891).

[56] E. Tyler and E. G. Richardson, "The characteristic curves of liquid jets," Proceedings of the Physical Society **37**, pp. 297-311 (1925).

[57] A. Haenlein, "Über den zerfall eines flüssigkeitsstrahls (On the distruption of a liquid jet)," Forschung auf dem Gebiete des Ingenieurwesens (Research in the field of engineering) **2**, pp. 139-149 (1931).

[58] W. Ohnesorge, "Die bildung von tropfen an düsen und die auflösung flüssiger strahlen (Formation of drops by nozzles and the breakup of liquid jets)," Zeitschrift für angewandte mathematik und mechanik (Journal of Mathematics and Mechanics) **16** (6), pp. 355-358 (1936).

[59] E. Becker, W. J. Hiller, and T. A. Kowalewski, "Experimental and theoretical investigation of large-amplitude oscillations of liquid droplets," Journal of Fluid Mechanics **231**, pp. 189-210 (1991).

[60] N. Instruments, LabVIEW version 7.0 (National Instruments, Austin, TX, 2006).

[61] N. Instruments, Vision Assistant version 7.0.0 (National Instruments, Austin, TX, 2006).

[62] R. J. Lang, "Ultrasonic Atomization of Liquids," The Journal of the Acoustical Society of America **34** (1), pp. 6-8 (1962).

[63] R. Rajan and A. B. Pandit, "Correlations to predict droplet size in ultrasonic atomization," Ultrasonics **39** (4), pp. 235-255 (2001).

[64] L. J. W. S. Rayleigh, *The Theory of Sound* (Dover Publications, New York, NY, 1945), p. 344.

[65] W. Eisenmenger, "Dynamic properties of the surface tension of water and aqueous solutions of surface active agents with standing capillary waves in the frequency range from 10 kc/s to 1.5 Mc/s," Acustica **9** (4), pp. 227-240 (1959).

[66] L. J. W. S. Rayleigh, "On the instability of jets," Proceedings of the London Mathematical Society **10**, pp. 4-13 (1878).

[67] S. W. J. Smith and H. Moss, "Experiments with mercury jets," Proceedings of the Royal Society of London, Series A **93** (652), pp. 373-393 (1917).

[68] C. Weber, "Zum Zerfall eines Flüssigkeitsstrahles (On the decay of a liquid jet)," Zeitschrift für angewandte mathematik und mechanik (Journal of Mathematics and Mechanics) **11** (2), pp. 136-154 (1931).

[69] A. C. Merrington and E. G. Richardson, "The break-up of liquid jets," Proceedings of the Physical Society **59** (1), pp. 1-13 (1947).

[70] J. M. Meacham, M. J. Varady, F. L. Degertekin, and A. G. Fedorov, "Droplet formation and ejection from a micromachined ultrasonic droplet generator: Visualization and scaling," Physics of Fluids **17** (10), pp. 1006051-1006058 (2005).

[71] I. Systat Software, SigmaPlot version 7.0 (Systat Software, Inc., Point Richmond, CA, 2001).

[72] Fluent, Fluent version 6.2 (Fluent, Lebanon, NH, 2006).

[73] H. C. Lee, "Drop Formation in a liquid jet," IBM Journal of Research and Development **18** (4), pp. 364-369 (1974).

[74] W. T. Pimbley, "Drop formation from a liquid jet: a linear one-dimensional analysis considered as a boundary value problem," IBM Journal of Research and Development **20** (2), pp. 148-156 (1976).

[75] S. E. Bechtel, M. G. Forest, and K. J. Lin, "Closure to all orders in 1-D models for slender viscoelastic jets: An integrated theory for axisymmetric, torsionless flow," Stability and Applied Analysis of Continuous Media **2**, pp. 59-100 (1992).

[76] L. Ting and J. B. Keller, "Slender jets and thin sheets with surface tension," SIAM (Society for Industrial and Applied Mathematics) Journal on Applied Mathematics **50** (6), pp. 1533-1546 (1990).

[77] J. Eggers, "Universal pinching of 3D axisymmetric free-surface flow," Physical Review Letters **71** (21), pp. 3458-3460 (1993).

[78] J. Eggers and T. F. Dupont, "Drop formation in a one-dimensional approximation of the Navier-Stokes equation," Journal of Fluid Mechanics **262**, pp. 205-221 (1994).

[79] F. J. Garcia and A. Castellanos, "One-dimensional models for slender axisymmetric viscous liquid jets," Physics of Fluids **6** (8), pp. 2676-2689 (1994).

[80] D. T. Papageorgiou, "On the breakup of viscous liquid threads," Physics of Fluids **7** (7), pp. 1529-1544 (1995).

[81] S. E. Bechtel, C. D. Carlson, and M. G. Forest, "Recovery of the Rayleigh capillary instability from slender 1-D inviscid and viscous models," Physics of Fluids **7** (12), pp. 2956-2971 (1995).

[82] B. Ambravaneswaran, E. D. Wilkes, and O. A. Basaran, "Drop formation from a capillary tube: Comparison of one-dimensional and two-dimensional analyses and occurrence of satellite drops," Physics of Fluids **14** (8), pp. 2606-2621 (2002).

[83] X. D. Shi, M. P. Brenner, and S. R. Nagel, "Cascade of structure in a drop falling from a faucet," Science **265** (5169), pp. 219-222 (1994).

[84] M. P. Brenner, X. D. Shi, and S. R. Nagel, "Iterated instabilities during droplet fission," Physical Review Letters **73** (25), pp. 3391-3394 (1994).

[85] E. D. Wilkes, S. D. Phillips, and O. A. Basaran, "Computational and experimental analysis of dynamics of drop formation," Physics of Fluids **11** (12), pp. 3577-3598 (1999).

[86] R. M. S. M. Schulkes, "Evolution and bifurcation of a pendant drop," Journal of Fluid Mechanics **278**, pp. 83-100 (1994).

[87] D. F. Zhang and H. A. Stone, "Drop formation in viscous flows at a vertical capillary tube," Physics of Fluids **9** (8), pp. 2234-2242 (1997).

[88] P. K. Notz, A. U. Chen, and O. A. Basaran, "Satellite drops: Unexpected dynamics and change of scaling during pinch-off," Physics of Fluids **13** (3), pp. 549-552 (2001).

[89] S. O. Unverdi and G. Tryggvason, "Computations of multi-fluid flows," Physica D: Nonlinear Phenomena **60** (1-4), pp. 70-83 (1992).

[90] S. O. Unverdi and G. Tryggvason, "A front tracking method for viscous incompressible flows," Journal of Computational Physics **100**, pp. 25-37 (1992).

[91] M. Sussman, E. Fatemi, P. Smereka, and S. Osher, "Improved level set method for incompressible two-phase flows," Computers & Fluids **27** (5-6), pp. 663-680 (1998).

[92] M. Sussman, P. Smereka, and S. Osher, "A level set approach for computing solution to incompressible two-phase flow," Journal of Computational Physics **114**, pp. 146-159 (1994).

[93] F. J. Kelecy and R. H. Pletcher, "The development of a free surface capturing approach for multidimensional free surface flows in closed containers," Journal of Computational Physics **138** (2), pp. 939-980 (1997).

[94] F. H. Harlow and J. E. Welch, "Numerical calculation of time dependent viscous incompressible flow of fluid with free surface," Physics of Fluids **8**, pp. 2182-2189 (1965).

[95] C. W. Hirt and B. D. Nichols, "Volume of fluid (VOF) method for the dynamics of free boundaries," Journal of Computational Physics **39**, pp. 91-119 (1981).

[96] M. Rudman, "Volume-tracking methods for interfacial flow calculations," International Journal for Numerical Methods in Fluids **24** (7), pp. 671-691 (1997).

[97] M. Rudman, "Volume-tracking method for incompressible multifluid flows with large density variations," International Journal for Numerical Methods in Fluids **28** (2), pp. 357-377 (1998).

[98] W. J. Rider and D. B. Kothe, "Reconstructing volume tracking," Journal of Computational Physics **141** (2), pp. 112-152 (1998).

[99] D. J. E. Harvie and D. F. Fletcher, "A new volume of fluid advection algorithm: The defined donating region scheme," International Journal for Numerical Methods in Fluids **35** (2), pp. 151-172 (2001).

[100] J. U. Brackbill, D. B. Kothe, and C. Zemach, "A continuum method for modelling surface tension," Journal of Computational Physics **100**, pp. 335-354 (1992).

[101] J. R. Richards, A. N. Beris, and A. M. Lenhoff, "Drop formation in liquid-liquid systems before and after jetting," Physics of Fluids **7** (11), pp. 2617-2630 (1995).

[102] J. R. Richards, A. M. Lenhoff, and A. N. Beris, "Dynamic breakup of liquid-liquid jets," Physics of Fluids **6** (8), pp. 2640-2655 (1994).

[103] D. L. Youngs, "Time-dependent multi-material flow with large fluid distortion," Numerical Methods for Fluid Dynamics, pp. 273-285 (1982).

[104] J. Hallmark, "End user perspective - industrial consumer electronics power," Proceedings of the DOE Fuel Cells for Portable Power Workshop, Phoenix, AZ (2002).

[105] T. Kikas, I. Bardenshteyn, C. Williamson, C. Ejimofor, P. Puri, and A. G. Fedorov, "Hydrogen production in a reverse-flow autothermal catalytic microreactor: from evidence of performance enhancement to innovative reactor design," Industrial and Engineering Chemistry Research **42**, pp. 6273-6279 (2003).

[106] S. Gottesfeld, "Direct methanol fuel cells for portable power - fuel cell developer perspectives," Proceedings of the DOE Fuel Cells for Portable Power Workshop, Phoenix, AZ (2002).

[107] J. S. Chin and A. H. Lefebvre, "Some comments on the characterization of drop-size distribution in sprays," Proceedings of the Third International Conference on Liquid Atomization and Spray Systems, London, UK, pp. IVA/1/1-12 (1985).

[108] G. D. Myers and A. H. Lefebvre, "Flame propagation in heterogeneous mixtures of fuel drops and air," Combustion and Flame **66**, pp. 193-210 (1986).

[109] G. A. Richards and A. H. Lefebvre, "Turbulent flame speeds of hydrocarbon fuel droplets in air," Combustion and Flame **78**, pp. 299-307 (1989).

[110] F. T. Cutts, C. J. Clements, and J. V. Bennett, "Alternative routes of measles immunisation: a review," Biologicals **25**, pp. 323-338 (1997).

[111] These results have been obtained in collaboration with the CDC, Atlanta, Georgia (Drs. Papania & Rotta).

[112] N. H. Bings, C. Wang, C. D. Skinner, C. L. Colyer, P. Thibault, and D. J. Harrison, "Microfluidic devices connected to fused-silica capillaries with minimal dead volume," Analytical Chemistry **71** (15), pp. 3292-3296 (1999).

[113] J. Li, P. Thibault, N. H. Bings, C. D. Skinner, C. Wang, C. L. Colyer, and D. J. Harrison, "Integration of microfabricated devices to capillary electrophoresis-electrospray mass spectrometry using a low dead volume connection: application to rapid analyses of proteolytic digests," Analytical Chemistry **71** (15), pp. 3036-3045 (1999).

[114] B. Zhang, H. Liu, B. L. Karger, and F. Foret, "Microfabricated devices for capillary electrophoresis-electrospray mass spectrometry," Analytical Chemistry **71** (15), pp. 3258-3264 (1999).

[115] S. Le Gac, S. Arscott, C. Cren-Olive, and C. Rolando, "Two-dimensional microfabricated sources for nanoelectrospray," Journal of Mass Spectrometry **38** (12), pp. 1259-1264 (2003).

[116] Q. Xue, F. Foret, Y. M. Dunayevskiy, P. M. Zavracky, N. E. McGruer, and B. L. Karger, "Multichannel microchip electrospray mass spectrometry," Analytical Chemistry **69** (3), pp. 426-430 (1997).

[117] L. Licklider, X.-Q. Wang, A. Desai, Y.-C. Tai, and T. D. Lee, "A micromachined chip-based electrospray source for mass spectrometry," Analytical Chemistry **72** (2), pp. 367-375 (2000).

[118] S. Zhang, C. K. Van Pelt, and J. D. Henlion, "Automated chip-based nanoelectrospray mass spectrometry for rapid identification of proteins separated by two-dimensional gel electrophoresis," Electrophoresis **24** (21), pp. 3620-3632 (2003).